

# Institut für Festkörperphysik

FRIEDRICH-SCHILLER-UNIVERSITÄT JENA



**Annual Report 2010**



**Institut für Festkörperphysik  
Friedrich-Schiller-Universität Jena  
Max-Wien-Platz 1  
D-07743 JENA**

Tel.: +49 (0) 3641 / 947300  
Fax: +49 (0) 3641 / 947302  
e-mail: carsten.ronning@uni-jena.de  
home page: <http://www.ifk.uni-jena.de/>

Prof. Dr. Carsten Ronning  
director Tel.: +49 (0) 3641 / 947300, 947301  
Fax: +49 (0) 3641 / 947302  
e-mail: carsten.ronning@uni-jena.de  
home page: <http://www.nano.uni-jena.de/>

Prof. Dr. Torsten Fritz Tel.: +49 (0) 3641 / 947400, 947411  
Fax: +49 (0) 3641 / 947412  
e-mail: torsten.fritz@uni-jena.de  
home page: <http://www.organics.uni-jena.de/>

Prof. Dr. Friedrich Huisken Tel.: +49 (0) 3641 / 947354, 947301  
Fax: +49 (0) 3641 / 947308  
e-mail: friedrich.huisken@uni-jena.de  
home page: <http://www.astrolab.uni-jena.de/>

PD Dr. Heinrich Metzner Tel.: +49(0) 3641 / 947353  
Fax: +49(0) 3641 / 947302  
e-mail: heiner.metzner@uni-jena.de  
home page: <http://www.physik.uni-jena.de/inst/exphys/cislab/>

Prof. Dr. Paul Seidel Tel.: +49 (0) 3641 / 947410, 947411  
Fax: +49 (0) 3641 / 947412  
e-mail: paul.seidel@uni-jena.de  
home page: <http://www.physik.uni-jena.de/~tief>

Prof. Dr. Werner Wesch Tel.: +49 (0) 3641 / 947330, 947301  
Fax: +49 (0) 3641 / 947302  
e-mail: werner.wesch@uni-jena.de  
home page: <http://www.physik.uni-jena.de/inst/exphys/ionen/>

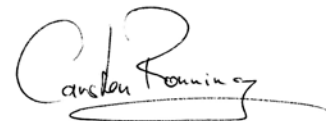
## Preface

We like to take this annual report 2010 as an opportunity to thank a lot of people and organizations for their manifold support for our research at the Institute of Solid-State Physics at the Friedrich-Schiller-University Jena. Furthermore, this report, which is already the 15<sup>th</sup> in this series, is also addressed to the interested scientific community and to our colleagues within the university and from outside.

Special thanks go to the following organizations for their financial support:

- Deutsche Forschungsgemeinschaft – DFG
- Bundesministerium für Bildung und Forschung – BMBF
- Bundesministerium für Umwelt, Naturschutz und Reaktorsicherheit – BMU
- Bundesministerium für Wirtschaft und Technologie – BMWi
- Thüringer Ministerium für Bildung, Wissenschaft und Kultur – TMBWK
- Deutscher Akademischer Austauschdienst – DAAD
- Gesellschaft für Schwerionenforschung, Darmstadt – GSI
- Deutsches Elektron Synchrotron, Hamburg – DESY
- Several Industrial Partners

We like also to thank all our colleagues at other Universities and Institutes, which are collaborating with us, but the collaborative work has not be presented in the research articles of this report. Furthermore, we are very grateful for the work of our very motivated secretaries, technicians and the people in the mechanical and electrical workshops. All have contributed to our research in an outstanding way and, thus, to this report.

A handwritten signature in black ink, appearing to read 'Carsten Ronning', with a stylized flourish underneath.

Prof. Dr. Carsten Ronning

# Contents

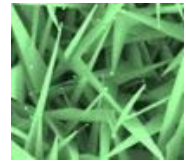
<b>1. Scientific groups of the institute</b>	6
<b>2. Scientific reports</b>	
Characterizing epitaxial Graphene .....	12
PL quantum efficiency of silicon nanocrystals measured by laser-induced deflection .....	14
Multiple peak photoluminescence from Ge-doped silicon oxide nanoparticles .....	16
Determination of the Number of Graphene Layers by Raman Spectroscopy .....	18
Structural modification of SHI irradiated a-Ge layers at low temperatures .....	19
Ion-beam-induced damage formation in CdTe at 15 K .....	20
Development of porous structures in GaSb by ion irradiation .....	22
In-situ RBS channeling studies of ion implanted semiconductors and insulators .....	24
Luminescence properties of terbium doped zinc sulphide nanowires .....	25
Q-factor measurements of Calcium Fluoride at low temperatures .....	26
Cryogenic Current Comparator .....	28
Elastic resonance spectrum of bonded crystalline silicon samples.....	30
Principles and methods for Q-factor measurements of cantilevers .....	32
Investigation of the mechanical loss of a thin silica coated cantilever .....	34
Compensation of thermo-elastic noise in silicon suspension elements .....	36
Temperature dependent magnetorelaxometry: numerical simulation of energy barrier distribution.....	38
Experimental and theoretical investigation on high-Tc superconducting intrinsic Josephson junctions .....	40
Preparation and characterisation of tunnelling junctions based on Ba(Fe <sub>0.9</sub> Co <sub>0.1</sub> ) <sub>2</sub> As <sub>2</sub> -superconductor thin films.....	42
Thin film hybrid Josephson junctions on iron-based superconductors.....	44
Ion Beam Irradiation of Nanostructures: 3D Monte Carlo Simulations .....	46
FIB/SEM Dual Beam System - FEI NanoLab Helios 600i .....	48
Design and characterization of ZnO nanowire field effect transistors .....	50
Lasing in single ZnO nanowires at room temperature .....	52
Optical properties of cuprous oxide .....	54
Exploring the luminescence of nanostructures and solar cells .....	56
Intense intra-3d-emission from Co <sup>2+</sup> doped ZnO nanowires .....	58
Morphology Changes and Alignment of Semiconductor Nanowires using Ion Beams .....	60
Biofunctionalization of ZnO nanowires .....	62
Protein adsorption behavior on Si and TiO <sub>2</sub> nanoripples.....	64
Modelling the Quantum Efficiency of Cadmium Telluride Solar Cells .....	66
Back Contact Formation in Cadmium Telluride Thin Film Solar Cells.....	68

The zinc oxide – molybdenum specific contact resistance for applications in Cu(In,Ga)Se <sub>2</sub> solar cell technology.....	70
Production of CIGS solar cells in a non-vacuum process using high-temperature sintering .....	72
Phosphorus Implanted Cadmium Telluride Solar Cells .....	74
Increased homogeneity and open-circuit voltage of Cu(In,Ga)Se <sub>2</sub> solar cells due to higher deposition temperature .....	76
Investigation of the Excitonic Luminescence Band of CdTe Solar Cells by Photoluminescence Excitation Spectroscopy .....	78
Electrical behaviour of CIS solar cells under spectral illumination .....	80
Thermal admittance spectroscopy on Cu(In,Ga)(Se,S) <sub>2</sub> -based solar cells.....	82
Interface modification by ion implantation in Cu(In,Ga)Se <sub>2</sub> solar cells.....	84
<b>3. Technical reports and equipment</b>	
Operation of the ion-accelerators JULIA and the ion-implanter ROMEO .....	86
Cryogenic service .....	88
Equipment .....	89
<b>4. Current research projects</b>	<b>93</b>
<b>5. Publications</b>	
5.1 Publications in scientific journals .....	96
5.2 Invited talks and colloquia .....	100
5.3 Conference contributions .....	103
5.4 Theses .....	110
<b>6. Cooperations, guests and colloquia at IFK</b>	
6.1 Visiting scientists .....	113
6.2 Colloquia at Institute of Solid State Physics .....	113
<b>7. Teaching activities</b>	
7.1 Lectures .....	115
7.2 Seminars .....	115
7.3 Practica .....	116
<b>8. Personnel</b>	<b>117</b>

## Scientific groups of the institute

### Experimental Physics / Solid State Physics

*Prof. Dr. C. Ronning*



- Synthesis, doping and functionalization of semiconductor nanowires
- Semiconductor physics: doping using ion beams
- Growth and functionalization of diamond-like materials
- Ion beam analysis

Recent work of the research group in the field of semiconductor nanowires focuses both on the growth of desired nanostructures as well as on the modification of semiconductor nanowires for the use as photonic and electronic devices. This includes in realization of light-emitting diodes and the observation of laser oscillations within single ZnO nanowires. The latter results have been realized in collaboration with the group of Prof. Dr. F. Capasso from the Harvard University – an fruitful exchange collaboration, which has been supported by DAAD in 2010.

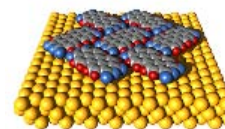
In the area of semiconductor nanowires the group holds further successful collaborations within the SPP-Program “Nanowires and Nanotubes” of the DFG. This includes PL-investigations of H-treated single ZnO nanowires together with Dr. T. Voss (Uni Bremen), life-time measurements of ZnS:Mn nanostructures with Prof. Dr. W. Heimbrodt (Uni Marburg), the electrical doping of III-V-nanowires with Dr. W. Prost (Uni Duisburg), as well as the growth of desired nanostructures together with Prof. Dr. R. Adelung (Uni Kiel).

Besides those supported collaborations by funding agencies, the group works also on the electrical functionalization of Si nanowires for different kind of memory devices or solar cells together with Dr. A. Colli / Prof. Dr. A. Ferrari (University of Cambridge, UK) and PD Dr. S. Christiansen (IPHT Jena)

Another important scientific area of the group is the investigation of hard/soft interfaces in terms of biocompatibility. Here, the accelerator systems Mr. JIM Stringer and LEILA are used for the growth of diamond-like materials as well as for nanostructuring of surfaces (Ripples). The biocompatibility and bioactivity of such thin films and surfaces is currently investigated in collaboration with the IMT.

Finally, it is worth to mention that on-going work of the group is performed in the area of ion beam doping of ZnO (in collaboration with Prof. Dr. M. Grundmann, Uni Leipzig), ion beam doping of Cu<sub>2</sub>O thin films (Prof. Dr. B.K. Meyer, University of Gießen), ion beam analysis of thin high-*k* materials (Dr. C. Wenger, IHP Frankfurt/Oder), and RBS-investigations of BN thin films (Prof. Dr. H.G. Boyen, Uni Hasselt).

## Applied Physics / Solid State Physics



*Prof. Dr. T. Fritz*

- Preparation of highly ordered thin films of organic molecules by UHV-deposition (OMBE)
- Chemical vapor deposition and characterization of carbon nanotubes
- Growth of graphene and carbon nanotubes on silicon carbide
- *In situ* optical spectroscopy (DRS)
- Analyses of surfaces, layers and nanostructures using AES, XPS, LEED, RHEED, XPD, STM, AFM, and SEM

The group *Applied Physics / Solid State Physics* (formerly known as *Physics of thin films*-group) at the Institute of Solid State Physics is engaged in the research on nanostructures, solid surfaces and thin films of both organic and inorganic semiconductor materials.

Our main research interest lies in the discovery of structure-property-relations of structurally well defined ultrathin epitaxial layers, organic quantum wells and carbon nanotubes. The main target of our research is the development of basic principles for the use of nano materials in prospective devices.

For analyses of the chemical composition and bonding at surfaces and in thin films we use surface analysis methods like photoelectron spectroscopy (XPS, UPS) and Auger electron spectroscopy (AES). The crystalline structure can be determined by electron diffraction (LEED, XPD, and electron channeling). Scanning tunneling microscopy (STM), atomic force microscopy (AFM) and scanning electron microscopy (SEM) are used for high-resolution imaging of nanostructures and surfaces.

Our *in situ* optical spectroscopy, namely differential reflectance spectroscopy (DRS) is used to study organic (sub-)monolayers and heterostructures in terms of absorption spectroscopy to analyse the optical interaction between the molecules or between organic adsorbates and inorganic substrates.

We have also developed a computational method to calculate the inter- and intralayer potential energy and to predict epitaxial alignments for realistically large OMBE domains (comprising several thousands of molecules).

Carbon nanotubes have been produced on solid substrates by chemical vapour deposition (CVD) using methane and ethanol as precursor gas. Extensive characterization of the CVD samples by SEM, AFM and Raman spectroscopy revealed high-quality single-wall carbon nanotubes of diameters between 1 and 2 nm. The amount of residual catalyst and amorphous carbon species has been determined to be very low. Our long-time experience in silicon carbide research has been used to grow graphene as well as carbon nanotubes on single-crystalline SiC substrates.



## Low Temperature Physics



*Prof. Dr. P. Seidel*

- Superconductivity within thin layers and layer systems
- Josephson effects, proximity effect, tunnel effects and quantum effects in superconducting devices
- DC-SQUID's and their application in measurement, e.g. biomagnetism, MRX, CCC
- cryogenic measurements on optical components (mechanical quality factor)
- Dynamics of superconducting Josephson arrays and qubits
- cryogenic engineering (cryocoolers, cryogenic storage)

The *low temperature physics* group works on the following fields:

- preparation, characterization, modelling and application of Josephson junctions and SQUIDs (precision and magnetorelaxation measurements with LTS SQUIDs, non-destructive evaluation and biomagnetism with HTS SQUIDs, intrinsic Josephson junctions)
- low temperature physics and cryogenic engineering (development of new kinds of pulse tube cryocoolers, investigations on a new concept for regenerators, cryogenic storage, cryogenic current comparator CCC)
- experimental work within the SFB/TR on cryogenic measurements of the Q-factor of optical components including grating optics
- thin film technologies for insulators and other materials

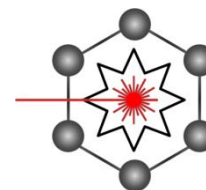
The research is carried out in cooperations with other research groups in Thuringia (TU Ilmenau, IPHT Jena, SUPRACON Jena, Innovent e.V. Jena). Within common activities the group works together with the Gesellschaft für Schwerionenforschung Darmstadt, DESY Hamburg, ILK Dresden, IFW Dresden, TARGET Systemelectronic GmbH Solingen and the Zentrum für Raumfahrt-technologie und Mikrogravitation Bremen.

Several research activities exist with industrial partners e.g. with Air Liquide (France), Northrop Gruman (USA), AEG Infrared Moduls GmbH Heilbronn and the TransMIT center for adaptive cryotechniques Gießen. A long tradition of cooperation with the Institute of Electrical Engineering (IEE) of the Slovak Academy of Sciences Bratislava, the Universities of Moscow (Russia), Kharkov (Ukraine), Glasgow (U.K.), Padua (Italy) and Vienna (Austria), and the University of Osaka (Japan) is also remarkable.

## Laboratory Astrophysics/Cluster Physics

*Prof. Dr. F. Huisken*

- Photoluminescence studies of silicon and germanium nanocrystals produced by CO<sub>2</sub> laser pyrolysis
- Electronic spectroscopy of neutral and ionized polycyclic aromatic hydrocarbons (PAHs) in supersonic jets and cryogenic matrices
- Study of astrochemical reactions in liquid helium nanodroplets



The Joint *Laboratory Astrophysics/Cluster Physics* Group at the Institute of Solid State Physics results from a cooperation between the MaxPlanckInstitute for Astronomy, Heidelberg, and the FriedrichSchillerUniversity, Jena. Inaugurated in February 2003, it is conducted by Prof. Dr. Thomas Henning and Prof. Dr. Friedrich Huisken.

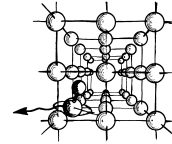
The research of the Joint Laboratory Astrophysics and Cluster Physics Group is devoted to fundamental astrophysical questions that can be answered by laboratory experiments, with particular emphasis on spectroscopy. The electromagnetic radiation reaching us from stellar objects is modified in a characteristic manner by interstellar molecules and dust particles. Many of these “fingerprints” are still far from being understood. In order to determine the species causing the modification of the electromagnetic signals detected by telescopes and satellites, comprehensive laboratory studies are urgently needed.

The laboratory is equipped with modern molecular and cluster beam machines as well as laser systems to contribute to the clarification of such fundamental questions. For this purpose, the molecules, clusters, and nanoparticles of interest are prepared in vacuum chambers under conditions coming close to those encountered in the interstellar space (low temperature and low density).

## **Ion Beam Physics**

*Prof. Dr. W. Wesch*

- Modification of solids by ion implantation and succeeding processes and ion beam analysis (RBS, PIXE, ERD, NRA)
- Ion beam synthesis of buried nanostructures
- Investigation of the effect of high electronic excitation on structural modification of crystalline and amorphous semiconductors
- Simulation of processes of ion-solid interaction



The *Ion Beam Physics* Group deals with modification of solids and synthesis of buried nanostructures using ion beams and combined secondary processes. The studies cover fundamental processes of ion-beam induced structural modification in semiconductors and insulators being relevant for future electronic, optoelectronic and photonic device technologies.

Concerning the II-VI semiconductors, in 2010 the studies were focused to the investigation of damage formation in CdTe at room temperature and 15 K using our two-beam irradiation chamber for in situ irradiation and ion beam analysis. Furthermore damage evolution in SiC by silver and neutron irradiation was investigated in collaboration with the University of Pretoria in South Africa. The investigation of structural modification of LiNbO<sub>3</sub> by ion irradiation as well as ion beam enhanced etching of this material was continued in collaboration with the Institute of Applied Physics. Additionally we started to study ion beam synthesis of metal nanoclusters in LiNbO<sub>3</sub> for photonic applications, and in collaboration with the University Minsk in Belarus we continued our work on ion beam synthesis of III-V compound nanoclusters in silicon.

Beside these activities on materials modification utilizing ion beams with conventional energies (several 10 keV to several MeV), the effect of high electronic excitation due to swift heavy ion irradiation (several 100 MeV) on plastic deformation and on the formation of voids and porous structures in amorphous Ge and GaSb were studied in collaboration with the Australian National University Canberra in Australia. The processes of void formation in amorphous Ge was also investigated by classical molecular dynamics computer simulations.

## Photovoltaics

*PD Dr. H. Metzner*



- Preparation and development of  $\text{Cu(In,Ga)(Se,S)}_2$  - based thin film solar cells
- Preparation and development of CdTe-based thin film solar cells
- Investigation of epitaxially grown heterostructures for photovoltaics

The research of the *photovoltaics* group is directed to three different fields:

- Preparation and development of  $\text{Cu(In,Ga)(Se,S)}_2$  - based thin film solar cells (CIGS). The research aims at a better understanding of the materials science of the CIGS chalcopyrite semiconductor and the improvement of existing and the development of novel cell concepts. To this end, a complete baseline on a form factor of  $10 \times 10 \text{ cm}^2$  is available as well as various characterization tools including AM 1.5 solar simulation and spectral response.
- Preparation and development of CdTe-based thin film solar cells. The research aims at a better understanding of the materials science of the II-VI semiconductor CdTe and the improvement of existing and the development of novel cell concepts. To this end, a complete baseline on a form factor of  $10 \times 10 \text{ cm}^2$  is available as well as various characterization tools including AM 1.5 solar simulation and spectral response.
- Investigation of epitaxially grown heterostructures for photovoltaics. The research aims at a better understanding of the materials science of heterostructures between silicon and CIGS and the development of novel cell concepts. To this end, a complete system for molecular beam epitaxy (MBE) is in operation which includes the *in situ* analysis by means of electron diffraction (RHEED).

The photovoltaics group collaborates with other university groups, research institutions, and the photovoltaic industry in numerous research projects.

The IFK photovoltaics group is member of the following institutions which include:

- **“Solar Input” e.V.**  
a collaboration of photovoltaic industry and research institutions located in Thuringia,
- **“PV-Uni-Netz”**  
a collaboration of photovoltaic research groups at 12 German universities.

# Characterizing epitaxial Graphene

Matthias Meißner, Bernd Schröter, and Torsten Fritz

The 2010 Nobel Prize for physics and the quickly growing number of publications about graphene show that this is a material widely expected to have a great impact in science and technology. Preparing homogeneous large-area graphene sheets remains a key problem, though.

Heating silicon carbide (SiC) crystals to a point where Si evaporates and the C atoms at the surface rearrange themselves to graphene layers is one way to grow graphene. We have used a technique where the heating is done in an argon atmosphere at ambient pressure to increase the homogeneity and area of graphene domains [1]. The resulting samples show epitaxially grown graphene layers, when the Si-face of the crystals is used.

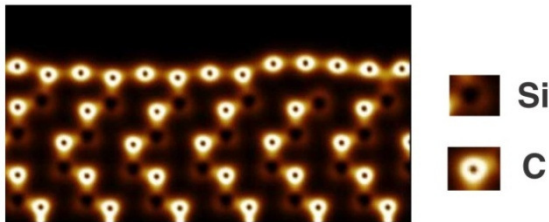


**Fig. 1:** *Ab initio* calculation of graphene-like buffer layer on SiC [5].

The structure of the interface between graphene and the Si-face of SiC has been controversially discussed [2,3]. Recently a model was proposed in which the interface layer, called buffer layer, consists of a single graphene-like layer which is partially bound to the SiC crystal (cf. Fig. 1) and decouples further layers from the substrate [4,5]. We could confirm that X-ray Photoelectron Spectroscopy (XPS) and Low Energy Electron Diffraction (LEED) data can be explained by this model [6]. The complex diffraction patterns of the interface have been attributed to a

$6\sqrt{3}\times 6\sqrt{3}$ -R30 ( $6\sqrt{3}$  for short) supercell that develops due to the lattice constant difference between graphene and SiC. However, not all of the reciprocal  $6\sqrt{3}$  lattice spots are visible. This contradiction can be explained in two ways: 1) The effect of multiscattering between the SiC and the graphene lattice produces the additional spots besides the  $1\times 1$  SiC and graphene spots, and not the above mentioned superstructure. 2) The corrugation due to the partial bonding to the substrate [5] has indeed the  $6\sqrt{3}$  periodicity but enhances only the number of orders seen in LEED.

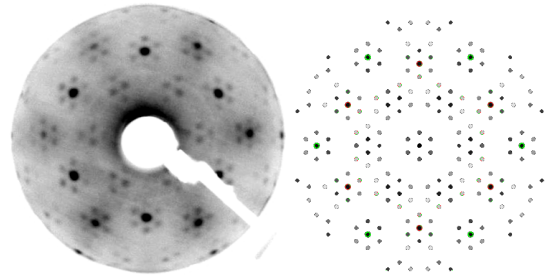


**Fig. 2:** LEED image at  $E = 116$  eV of a monolayer graphene on SiC (left) and geometrical multiscattering simulation (right;  $1\times 1$  SiC-spots red,  $1\times 1$  graphene spots green).

Both arguments can explain the observed LEED pattern, with the multiscattering model not requiring any corrugation of the surface. This can be attributed to the similarity of the Moiré effect and the multiscattering effect, both of which generate a new periodicity by superimposing two different lattices. The corrugation of the buffer layer, for its part, can roughly be explained by the Moiré effect because at positions where the graphene atoms are close to Si atoms from the substrate (i.e. where graphene lattice points are close to SiC lattice points) they

form bonds and thus lie lower. The symmetry of the resulting corrugation can be approximately reproduced by a simple Moiré simulation, and its Fourier transform shows the same features as the experimental LEED patterns [5,6]. Since geometrical multiscattering theory also combines the graphene and SiC periodicities, it does yield the same result.

However, additional experimental data favor the existence of a buffer layer over simple multiscattering. LEED patterns of samples with thicker graphene (4-5 monolayers) still showed signs of the  $6\sqrt{3}$  spots even though the  $1\times 1$  SiC spots were not visible anymore. Also Scanning Tunneling Microscopy (STM) measurements on samples with two and more graphene layers on a buffer layer retained the  $6\sqrt{3}$ -structure [7] rendering simple multiscattering insufficient to explain the data.

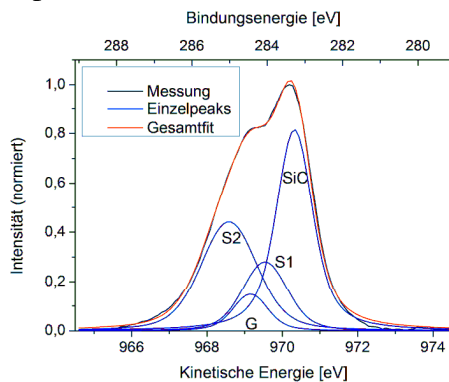


**Fig 3:** Normalized background-subtracted C1s spectrum of buffer layer on SiC – fitted according to the buffer layer model (cf. text).

With this buffer layer model we were able to fit XPS spectra of our samples. The carbon C1s peak thus contains four contributions: carbon from the substrate (SiC) and graphene (G), plus the buffer layer atoms that are bound to the substrate (S1), and the buffer layer atoms not bound to the substrate (S2). The latter contribution is shifted relative to the G

peak due to a charge transfer from the substrate.

To extract the number of graphene layers averaged over a large area from XPS we used a standard attenuation model in which the substrate electron intensity

$$I \sim \exp\left(-\frac{d}{\lambda}\right)$$

is exponentially weakened by an adsorbate layer of thickness  $d$ . However, for the substance-specific attenuation length  $\lambda$  there exist only estimations which leave an uncertainty of about 10%. Because of the exponential character of the equations this only allows for a rough estimate of the graphene thickness. Still, comparison with the relative intensities of the graphene and SiC spots in LEED and further methods such as Auger Electron Spectroscopy (AES) revealed empirical relationships that can be used to calibrate these methods within the uncertainty range of XPS.

Since we can now determine the average graphene thickness, we are able to work more quantitatively with graphene as a substrate and investigate its properties. Especially we will explore the interaction of graphene with organic molecules deposited upon it.

## References

- [1] K. V. Emtsev et al., *Nature Materials* **8**, 203 (2009).
- [2] A. J. v. Bommel, J. E. Crombeen, and A. v. Tooren, *Surf. Sci.* **48**, 463 (1975).
- [3] J. Hass et al., *Phys. Rev. B* **78**, 205424 (2008).
- [4] K. V. Emtsev et al., *Phys. Rev. B* **77**, 155303 (2008).
- [5] F. Varchon et al., *Phys. Rev. B* **77**, 235412 (2008).
- [6] M. Meißner, Diplomarbeit (2010).
- [7] K. Wachter, Bachelorarbeit (2010).

# PL quantum efficiency of silicon nanocrystals measured by laser-induced deflection

K. Potrick, T. Schmidt, S. Bublitz,\* Chr. Mühlig,\* W. Paa,\* and F. Huisken

\*Institut für Photonische Technologien (IPHT), Albert-Einstein-Str. 9, 07745 Jena

Silicon nanocrystals (Si NCs) have attracted much interest because of their ability to efficiently emit visible light. The photoluminescence (PL) of Si NCs with sizes between 3 and 8 nm is governed by the radiative recombination of excitons in a quantum-confined system. In order to show efficient PL, the Si NCs must be perfectly passivated to avoid dangling bonds on their surface. The simplest method leading to a stable passivation is probably natural oxidation in air. However, this process is rather slow as it takes about one month to achieve terminal passivation [1]. An important parameter to describe the quality of passivation is the quantum efficiency (QE)  $\eta_{\text{PL}}$  which is defined as the ratio of the number of emitted photons to the number of absorbed photons. Unfortunately, it is difficult to accurately measure the power absorbed by the Si NCs as well as the power emitted in the form of PL photons.

An alternative approach could be to measure the heat transferred to the sample by the excitation laser. When the sample is fresh the surface of the Si NCs is dominated by dangling bonds and no PL will occur. In this case, all absorbed laser power will be transferred to the phonon bath, *i.e.*, the entire absorbed power is converted into heat

which can be measured directly, *e.g.*, by the photo-thermal deflection technique described below. When time passes by, the passivation of dangling bonds proceeds and both, the PL signal and  $\eta_{\text{PL}}$ , increase. As a result, the heat input is diminished.

## Experiment

We have employed a sensitive photo-thermal deflection technique where small amounts of heat input can be measured by the deflection of a probe laser beam due to thermal lensing. The method, referred to as laser-induced deflection (LID) [2] is shortly explained with the help of Fig. 1. We consider a fused silica cuboid covered with a thin film capable of absorbing laser light at a given wavelength. In Fig. 1(a), we are facing the top surface covered by a thin layer of Si NCs which is illuminated by a violet laser beam. If the laser photons are absorbed by the film the absorption-induced heat is transferred to the fused silica cuboid, generating a temperature and refraction index gradient profile (thermal lens), schematically shown by the system of rings. A pair of probe laser beams from a diode laser source ( $\lambda = 640 \text{ nm}$ ) is directed through the fused silica block close to the heat source. Their deflections correlate with the amount of heat coupled into the cuboid. The device was calibrated with a thermal resistor so that the power converted into heat can be determined in absolute units. Figure 1(b) shows a side view of the setup. With the power sensor placed behind the fused silica block, the transmitted power of the excitation laser beam is measured. The PL emitted by the Si NCs is collected with an optical fiber and analyzed with a minispectro-

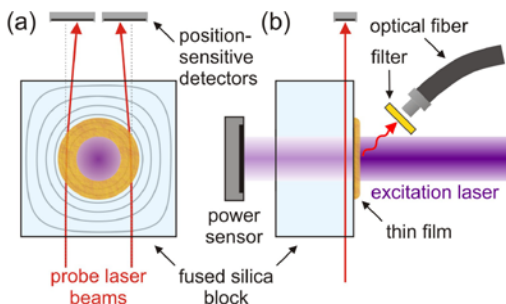


Fig. 1: Schematic view of the LID setup.



meter. A continuous-wave diode laser operating at  $\lambda = 406$  nm serves as the excitation source.

## Results

The LID technique has been used to measure the heat input into a film of freshly prepared Si NCs and to monitor the evolution of this process over a period of one month until saturation is achieved. At the same time, the transmittance of the laser beam used for excitation and the PL arising from the Si NCs with increasing efficiency are measured as well. The recorded data allows us to gain insight into the oxidation of Si NCs and the passivation of their dangling bonds during the first days and to derive the PL QE as a function of time. Note that the present method of QE determination is independent of the nature of the PL origin. With the knowledge of the porosity and thickness of the Si NC layer, it is possible to determine the absorption cross section of the Si NCs.

The Si NCs were prepared by laser-induced pyrolysis of silane in a cluster beam apparatus and deposited under vacuum as a thin layer on a fused silica block. The deposition time was 105 min resulting in a layer thickness of 205 nm as determined by atomic force microscopy. The average diameter of the crystalline core,  $d = 4.17$  nm, of the Si NCs at the end of the experiment, *i.e.*, after complete oxidation, was determined from the PL spectrum.

Figure 2(a) shows the behavior of the power converted into heat ( $P_{LID}$ ) as a function of time starting immediately after having taken the sample out of the vacuum and following the signal for 31 d. The LID signal reveals a sharp decrease during the first day which then slows down. The data could be fitted with a sum of two exponential decays yielding the time constants  $\tau_1 = 2.9$  h and  $\tau_2 = 5.3$  d. Interestingly, the early sharp de-

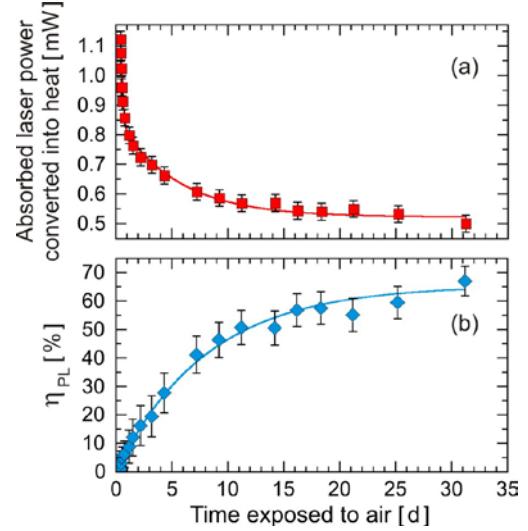


Fig. 2: Absorbed laser power converted into heat (a) and PL quantum efficiency  $\eta_{PL}$  (b) as a function of time after synthesis.

crease correlates with a sharp increase of the transmitted laser power, which can be explained by the fast formation of an oxide layer during the first few hours and the associated shrinking of the crystalline core. Having measured  $P_{LID}$  as a function of time and, in addition, the transmitted laser power,  $P_{trans}$ , as well as the PL peak position or band gap,  $E_{gap}$ , we are in the position to determine the quantum efficiency  $\eta_{PL}$ . However, as it was not possible to accurately measure the power reflected and scattered by the Si NCs, we could only determine a lower limit for the quantum efficiency. The result of the corresponding analysis is plotted in Fig. 2(b). It is found that the QE increases continually with a time constant of  $\tau_{\eta} = 8.1$  d and reaches saturation after  $\sim 30$  d. The extraordinarily high terminal QE of  $\sim 65\%$ , which must be still considered as a lower limit, points to a high quality of the Si NCs produced by laser pyrolysis and to an efficient passivation [3].

## References

- [1] G. Ledoux, J. Gong, and F. Huisken, Appl. Phys. Lett. 79 (2001) 4028.
- [2] C. Mühlig, S. Bublitz, and S. Kufert, Appl. Opt. 48 (2009) 6781
- [3] K. Potrick et al. Appl. Phys. Lett., submitted.



# Multiple peak photoluminescence from Ge-doped silicon oxide nanoparticles

T. Schmidt, L. Ma, K. Potrick, C. Jäger, and F. Huisken

In an earlier study, we have explored the optical properties of amorphous  $\text{SiO}_2$  nanoparticles ( $\text{SiO}_2$  NPs) that were obtained by the full oxidation of previously prepared silicon nanocrystals (Si NCs) [1]. The characteristics of the strong photoluminescence (PL) of the  $\text{SiO}_2$  NPs were very similar to those observed for the Si NCs from which the  $\text{SiO}_2$  NPs were prepared. As the PL of the Si NCs was governed by the recombination of quantum-confined excitons, whereas the PL of the  $\text{SiO}_2$  NPs was assigned to defect luminescence, the close correlation between the PL of Si NCs and  $\text{SiO}_2$  NPs was difficult to understand.

Encouraged by our new achievements in the production of  $\text{Si}_{1-x}\text{Ge}_x$  NCs with Ge contents of up to 20% [2], we have produced Si/Ge alloy oxide NPs and studied their optical properties. The motivation was threefold, (1) to find nanomaterials with new optical properties for applications in photonics and biology, (2) to obtain information on new light-emitting defect centers, and (3) to learn more about the defect centers in the previously studied pure  $\text{SiO}_2$  NPs by comparing the respective spectra.

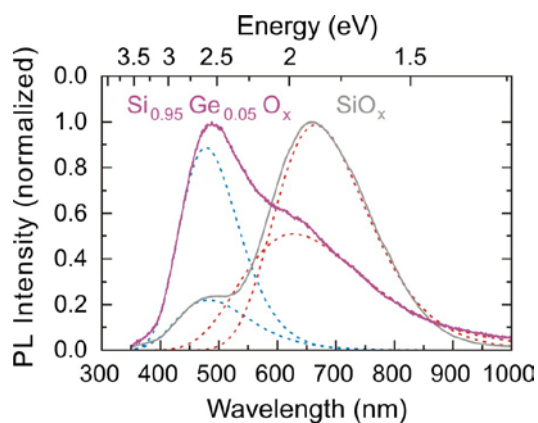


Fig. 1: The PL curve of oxidized Si/Ge NPs (violet curve in comparison with the one measured for pure  $\text{SiO}_x$  nanoparticles.

As starting material for the present study, we used silicon nanocrystals containing about 5% germanium, as produced by  $\text{CO}_2$  laser-induced pyrolysis of gaseous precursors [2]. The as-prepared nanopowder was oxidized in water [1], and after evaporation of the water, light-emitting Ge-containing silica nanoparticles were obtained. PL studies revealed the co-existence of at least two different defect centers, one associated with a blue emission (463 nm) and short emission lifetime (70 ns), the other showing red emission (617 nm) and a long lifetime (40  $\mu\text{s}$ ). The corresponding PL spectrum is displayed in Fig. 1 by the violet curve with the two components being represented by the blue and red dashed curves, respectively. Comparing the peak positions with literature data, we can assign the blue band to arise from oxygen-deficient centers (ODCs) while the red band is attributed to nonbridging oxygen hole centers (NBOHCs). It is interesting to note that the same defect centers have also been observed in pure  $\text{SiO}_x$  NPs as shown by the grey spectrum also presented in Fig. 1. However, the intensities associated with the two defect centers are reversed. The fact that the ODCs are more pronounced in the Ge-containing silica NPs indicates that these NPs are more difficult to oxidize if they are subjected to the same conditions.

As a means to obtain information on the average stoichiometry of the  $\text{Si}_{0.95}\text{Ge}_{0.05}\text{O}_x$  sample and to quench known or create new defect centers, we have performed annealing experiments at temperatures between 400 and 1000  $^\circ\text{C}$  in steps of 100  $^\circ\text{C}$  in an oxygen-free atmosphere with argon as protective gas. The PL spectra measured after

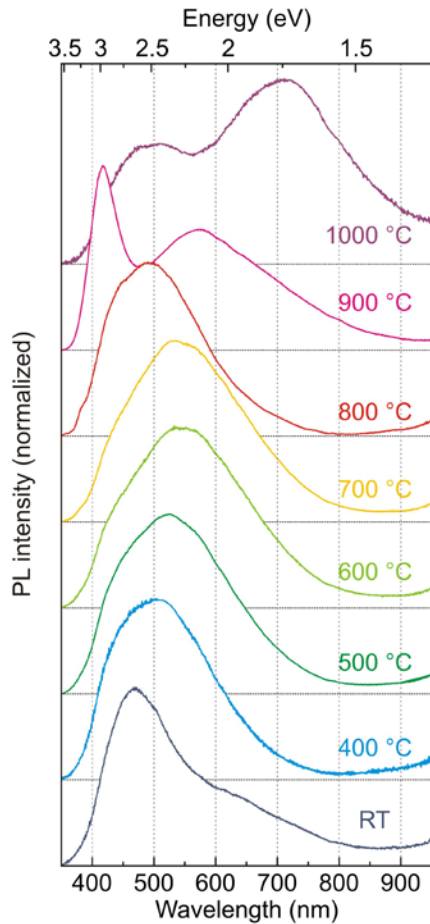


Fig. 2: Evolution of the PL of the Ge-doped silicon oxide nanopowder upon thermal annealing.

each annealing step are displayed together with the initial PL spectrum (RT) in Fig. 2. They reveal a continuous red shift with each isochronal annealing step from 400 to 600 °C, which is followed by a blue shift from 600 to 800 °C. This behavior indicates a variation of the distribution of surface versus volume ODC defect centers.

Most interestingly, after annealing at 900 °C, the PL spectrum splits into two components, a central peak at 2.2 eV and a new feature at 3.0 eV, indicating that new defect states were generated. In accordance with cathodoluminescence (CL) studies on Ge-implanted silica layers, the 3.0 eV defect center can be associated with Ge-related oxygen-deficient centers. Salh *et al.* [3] have investigated the formation of clusters in Ge ion-implanted amorphous silicon dioxide layers. They found a pronounced violet

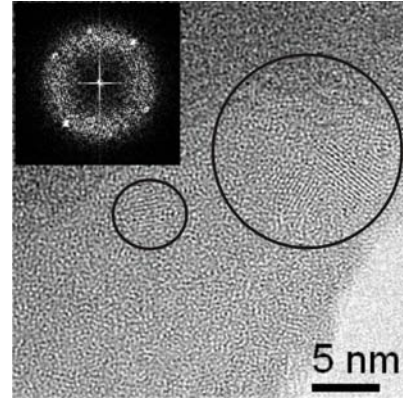


Fig. 3: HRTEM image of the  $\text{Si}_{0.95}\text{Ge}_{0.05}\text{O}_x$  NPs obtained after the last annealing step at 1000 °C.

CL peak at 410 nm (3.0 eV) when their sample was annealed at 800 – 900 °C. Supported by scanning transmission electron microscopy studies, which revealed small Ge nanocrystals, they concluded that the 3.0 eV CL band originates from ODCs at the surface of small Ge clusters. We adopt this interpretation and conclude that the Ge atoms in our substoichiometric sample have nucleated to form Ge nanoclusters.

After our last annealing step at 1000 °C, we observe strong white luminescence with a dominant PL band at 1.75 eV, which we assign to radiative exciton recombination in small Si NCs. Indeed, the formation of small Si NCs is proved by the HRTEM image shown in Fig. 3.

To conclude, we would like to note that we started from a crystalline Si/Ge alloy nanopowder which was transformed during the processing to a more bulk-like oxide material. With the final annealing steps, we achieved a phase separation leading to the independent formation of Ge and Si nanocrystals in an amorphous  $\text{SiO}_2$  matrix, thus returning to nanoscale physics.

## References

- [1] A. Colder, F. Huisken, E. Trave, *et al.*, *Nanotechnology* 15 (2004) L1.
- [2] L. B. Ma, T. Schmidt, O. Guillois, and F. Huisken, *Appl. Phys. Lett.* 95 (2009) 013115.
- [3] R. Salh, L. *et al.*, *Superlattice Microstruct.* 45 (2009) 362.

# Determination of the Number of Graphene Layers by Raman Spectroscopy

Martin Bohrisch, Bernd Schröter, and Torsten Fritz

Graphene is a two dimensional material which consists of carbon arranged in a honeycomb lattice. It is a zero gap semiconductor with a linear dispersion relationship near the Fermi energy  $E_F$ . Close to  $E_F$ , electrons behave like massless relativistic Dirac fermions. This unusual effect causes several outstanding phenomena [1]. Raman spectroscopy is a fast and non-destructive method to characterize carbon modifications [2]. Here it is used to identify the number of stacked layers of graphene grown on silicon carbide (SiC).

To synthesize the graphene, 6H-SiC(0001) was annealed at a temperature above 1200°C in argon atmosphere. Raman measurements were obtained at room temperature from a confocal Raman microscope *LabramDilor I* with a spatial resolution of 2  $\mu\text{m}$ . A HeNe-Laser with a wavelength of 633 nm was used for excitation. The Raman spectrum of graphene has two prominent features. These are the G-peak ( $\sim 1580 \text{ cm}^{-1}$ ) and the 2D-peak ( $2700 \text{ cm}^{-1}$ ). The G-peak from epitaxial graphene on SiC is interfered by modes of the substrate. The 2D-Band can be detected without any significant background from the substrate. It corresponds to a double resonant scattering process of electrons close to the K-point in the Brillouin-zone. It is possible to determine the number of stacked graphene sheets from this band. For two graphene layers, the dispersion close to the Fermi energy splits in two subbands [3]. In this band structure more than one double resonant scattering process is possible. As shown in fig. 1a the 2D-peak from a bilayer graphene is a superposition of four Lorentzians. The full width at half maximum (FWHM) of each peak is larger than the spectral distance between them, so they occur as one asymmetric band. The 2D-band of a monolayer graphene has a single Lorentzian, with a FWHM of about  $35 \text{ cm}^{-1}$ . For more than two layers the number of superposing peaks raises, the 2D-band becomes broader and assumes for ten stacked graphene sheets the same shape like the 2D-peak of graphite [4].

In the histogram plot in fig. 1b the quantity of measured FWHM of the 2D-band is categorized. Three distinct features accentuated through Gaussians can be identified. We have analyzed the shapes of the 2D-peak-spec-

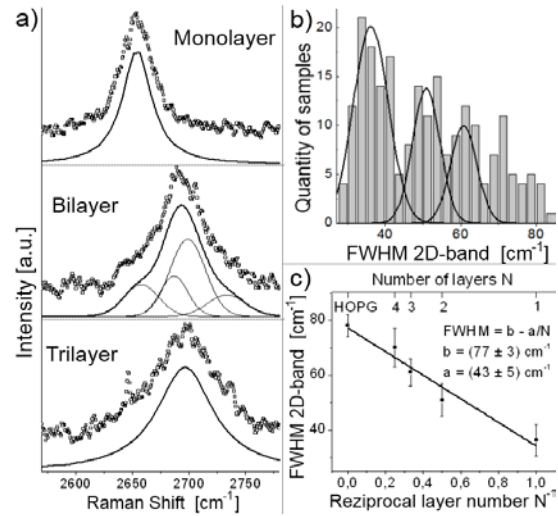


**Fig.1:** a) 2D-peaks of mono-, bi- and trilayer graphene with fitted Lorentzians. In b) the Number of samples is plotted sorted by the FWHM of the 2D-band. There are also Gaussians drawn to highlight the features in this statistic. In c) the centers of these curves are plotted versus the dedicated number of graphene sheets. [5]

tra from each histogram region by fitting Lorentzians to them. In the FWHM range of 25 to  $45 \text{ cm}^{-1}$  only one Lorentzian is required to match the spectrum. These 2D-peaks are caused by a monolayer graphene. To fit the spectra from the second region ( $45\text{-}56 \text{ cm}^{-1}$ ) four Lorentzians are needed. The 2D-bands from the third feature ( $56\text{-}65 \text{ cm}^{-1}$ ) have a broad asymmetric shape but could be well described by one peak. The whole issue is illustrated in fig. 1a. We assign the layer numbers one to three to the features in fig. 1b. Fig. 1c shows a linear relationship between the reciprocal number of graphene sheets and the FWHM of the 2D-peak of graphene, which justifies the determination of the number of stacked graphene layers by Raman spectroscopy. The FWHM of the 2D-peak for an infinite number of layers has been taken from the 2D-band of highly oriented pyrolytic graphite (HOPG).

We thank Harald Mutschke at the Astrophysics Institute for the possibility to accomplish Raman measurements.

- [1] C. Rao et al., J. Phys. Chem. Lett. **1**, 572 (2010).
- [2] E. Kurimoto et al., J. Appl. Phys. **85**, 5214 (2000).
- [3] C. Neto et al., Reviews of Modern Physics **81**, 109 (2009).
- [4] A. Ferrari et al., Physical Review Letters **97**, 187401 (2006).
- [5] M. Bohrisch, Diploma Thesis, FSU Jena, 2010.

# Structural modification of SHI irradiated a-Ge layers at low temperatures

T. Steinbach, C.C. Jacobi, W. Wesch, D. Severin\*, M. Bender\* and C. Trautmann\*

\*GSI Helmholtz Centre for Heavy Ion Research GmbH, Planckstr. 1, 64291 Darmstadt

Swift heavy ion (SHI) irradiation of amorphous Ge performed at the ANU accelerator facility reveals an extreme volume expansion [1]. A detailed study of the influence of SHI irradiation parameters on this effect [2] demonstrates that for all irradiation parameters used a strong swelling of the irradiated material was observed which is caused by the formation and growth of randomly distributed voids leading to a gradual transformation of the amorphous layer into a sponge-like porous structure. Moreover, the swelling linearly depends on the ion fluence  $N_I$  and on the value of electronic energy deposition  $\epsilon_e$ . Based on these results, we can conclude that voids are formed in a-Ge if a specific threshold value of the energy deposited by electronic processes is exceeded [2].

In this project we investigated the effect of the irradiation temperature as well as the influence of higher electronic energy deposition on the void formation in a-Ge layers (thickness  $d = 3.1 \mu\text{m}$ ). The experiments were performed at the M3-branch at the UNILAC. The sample was irradiated at  $T \approx 290$  and  $55 \text{ K}$  with  $940 \text{ MeV Au}$ -ions.

In Fig. 1 the step height  $\Delta z$  is depicted as a function of  $N_I$ . For both irradiation temperatures,  $\Delta z$  indicates a linear dependence on  $N_I$  similar to previous results (see black

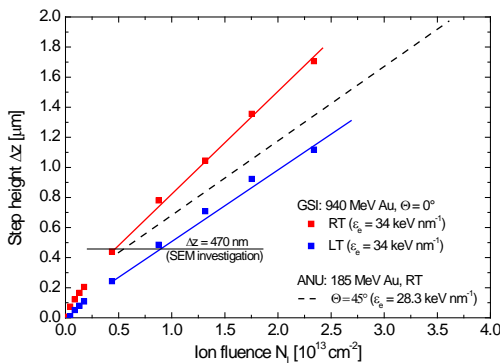


Fig. 1 Mean step height  $\Delta z$  for a-Ge irradiated with  $940 \text{ MeV Au}$ -ions at RT and LT (GSI) vs  $N_I$ . The black dashed line illustrates the swelling caused by  $185 \text{ MeV Au}$ -ion irradiation (ANU) [2].

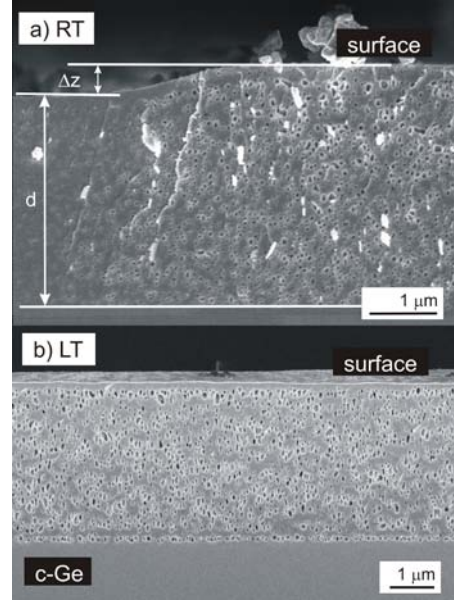


Fig. 2 Cs-SEM images showing the formation of voids after the irradiation at RT (a) and LT (b).

dashed line in Fig. 1 or Ref [2]). However, for the same ion fluence the volume expansion is much smaller for LT than for RT irradiation. Cs-SEM investigations (Fig. 2) revealed for both, RT and LT, the transformation of the initially homogeneous a-Ge layer into a porous structure with irregularly shaped voids. The samples in Fig. 2 are chosen for  $\Delta z \approx 470 \text{ nm}$  (see Fig. 1). The formation of voids, which accumulate with increasing ion fluence to form a porous layer, takes place solely in the  $3.1 \mu\text{m}$  thick amorphous surface layer while the underlying substrate is still crystalline and free of voids.

The mechanisms of void formation and the transformation into a sponge like structure are not yet understood and will be subject of further investigations.

Work supported by BMBF, contract no. 05KK7SJ1

## References

- [1] W. Wesch et al., J. Phys. D: Appl. Phys. 42 (2009) 115402.
- [2] T. Steinbach et al., Phys. Rev. B, accepted



# Ion-beam-induced damage formation in CdTe at 15 K

C. W. Rischau, C. S. Schnohr, E. Wendler and W. Wesch

Ion implantation studies on CdTe are of interest regarding a possible application of this technique in the fabrication of CdTe devices such as solar cells, infrared windows and radiation detectors, but also with respect to the fundamental understanding of ion-beam-induced damage formation in II-VI compounds. Investigations at room temperature exhibited some intriguing features like defects extending much deeper into the crystal than the calculated range of the ions and a high resistance to amorphization [1-3]. In order to reveal whether these effects are driven thermally, we studied the ion-beam-induced damage formation in CdTe at 15 K.

Commercial CdTe single crystals with  $\langle 111 \rangle$  or  $\langle 112 \rangle$  orientation were irradiated at 15 K with 270 keV Ar or 730 keV Sb ions to fluences ranging from  $1.0 \times 10^{11}$  to  $6.0 \times 10^{16} \text{ cm}^{-2}$ . Damage formation was studied with Rutherford backscattering spectrometry (RBS) in channeling configuration. The experiments were carried out in a two-beam chamber [4] which allows irradiation and subsequent analysis without changing the sample temperature. The relative defect concentration  $n_{\text{def}}$  was then obtained from the RBS spectra using the computer code DICADA [5]. For comparison, the depth distributions of primarily displaced target atoms  $N_{\text{disp}}$  and implanted ions  $N_{\text{ion}}$  were calculated with SRIM2008 [6] assuming displacement energies of  $E_d^{\text{Cd}} = 5.0 \text{ eV}$  and  $E_d^{\text{Te}} = 6.6 \text{ eV}$ .

Furthermore, the maximum value  $N_{\text{disp}}^{\text{max}}$  of the calculated distribution of primary displacements was used to transform the ion fluence  $N_I$  into the number of displacements per lattice atom  $n_{\text{dpa}}$ .

Figure 1 shows typical RBS spectra of  $\langle 111 \rangle$ -oriented CdTe irradiated with 270 keV Ar at 15 K. Up to the highest fluence of  $5.0 \times 10^{16} \text{ cm}^{-2}$  the channeling yield does not reach random level indicating CdTe is not rendered amorphous even after prolonged irradiation at 15 K. However, the spectra exhibit a distinctive surface peak and a knee at channel numbers significantly beyond the projected range  $R_p$  of the implanted ions. The latter feature was also observed in room temperature studies and is attributed there to the formation of correlated defects, i.e. to the formation of small dislocation loops [2,3].

In order to study the type of defects created at very low temperature, energy-dependent RBS measurements were performed for selected ion fluences. The energy dependence of the backscattering yield at a fixed depth  $z$  revealed that predominantly uncorrelated defects, i.e. point defects and defect clusters, are formed at 15 K. The fact that the same knee shape of the RBS spectra is observed for both correlated and

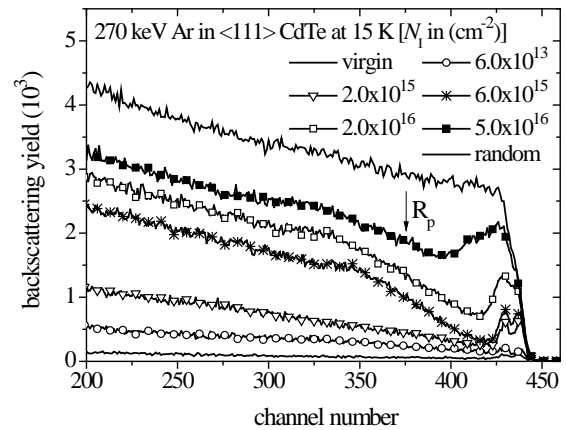


Fig. 1 RBS channeling spectra of 1.4 MeV He ions backscattered on  $\langle 111 \rangle$  CdTe irradiated with 270 keV Ar ions at 15 K. The arrow indicates the projected range of the implanted ions  $R_p = 0.22 \mu\text{m}$  calculated with SRIM2008.

uncorrelated defects can be explained by the broad distribution of defects together with the high mass of the Cd and Te atoms as was shown by DICADA simulations.

The defect distributions calculated with DICADA from the RBS spectra shown in Fig. 1 are plotted in Fig. 2. Similar to what was observed in room temperature studies, the defects extend to a depth of up to 4-5 times the projected range of the ions even after irradiation at 15 K.

The fluence dependence of the defect concentration was evaluated at two different depths, namely  $z = 0.1$  and  $0.35 \mu\text{m}$ , and is shown in Fig. 3. The increase of the defect concentration in *stage I* can be attributed to the production of primary point defects by single ion impacts. However, a comparison of  $n_{\text{def}}$  with  $n_{\text{dpa}}$  shows that only 20% of the primarily displaced lattice atoms survive the relaxation process of the collision cascades. In *stage II* the collision cascades of individual ions start to overlap leading to the recombination of vacancies and interstitials and thus to a saturation of the defect concentration. The strong increase of  $n_{\text{def}}$  in *stage III* can be attributed to the formation of a polycrystalline or amorphous surface layer ( $z = 0.10 \mu\text{m}$ ) or to the

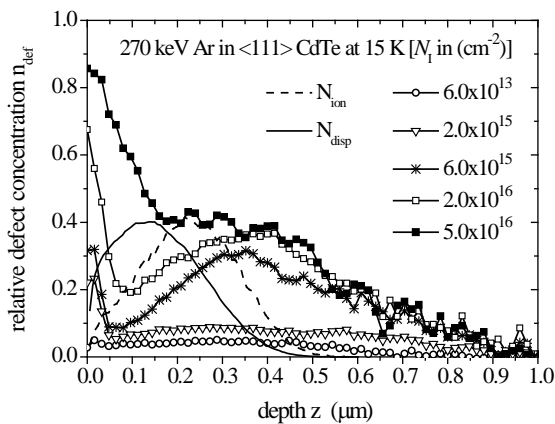


Fig. 2 Relative defect concentration  $n_{\text{def}}$  versus depth  $z$  calculated with DICADA for  $\langle 111 \rangle$  CdTe irradiated with 270 keV Ar ions at 15 K. The distributions of primary displacements  $N_{\text{disp}}$  and implanted ions  $N_{\text{ion}}$  were calculated with SRIM2008.

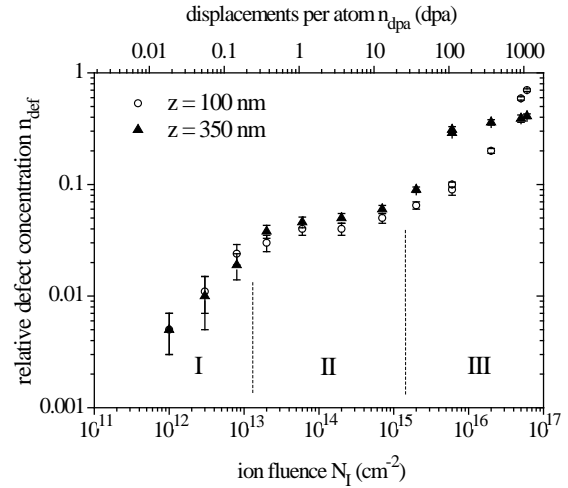


Fig. 3 Defect concentration  $n_{\text{def}}$  at  $z = 0.10$  and  $0.35 \mu\text{m}$  as a function of ion fluence  $N_1$  (lower scale) and number of displacements per lattice atoms  $n_{\text{dpa}}$  (upper scale) for  $\langle 111 \rangle$  CdTe irradiated with 270 keV Ar at 15 K.

formation, growth and saturation of non-recombinable defect clusters ( $z = 0.35 \mu\text{m}$ ). The same observations are made for  $\langle 112 \rangle$ -oriented CdTe and for Sb instead of Ar. In particular, a strong resistance to amorphization and a range of the ion-beam-induced defects much larger than the projected range of the ions were seen for all irradiations at 15 K thus eliminating a thermal origin for both effects. The high ionicity of the CdTe crystal and recombination-enhanced diffusion are instead believed to be responsible for the intriguing damage formation behaviour of this important II-VI compound [7,8].

## References

- [1] M. Gettings, K.G. Stephens, Rad. Effects 22 (1974) 53.
- [2] G. Leo et al., Nucl. Instr. Meth. B 63 (1992) 41.
- [3] G. Leo, M. Ruault, J. Appl. Phys. 73 (1993) 2234.
- [4] B. Breeger et al., Nucl. Instr. Meth. B 174 (2001) 199.
- [5] K. Gärtner, Nucl. Instr. Meth. B 227 (2005) 522.
- [6] J.F. Ziegler, J.P. Biersack, U. Littmark, The Stopping and Range of Ions in Solids, Pergamon, New York, 2003.
- [7] H.M. Naguib, R. Kelly, Rad. Effects 25 (1975) 1.
- [8] J.C. Bourgoin, J.W. Corbett, Rad. Effects 36 (1978) 157.

# Development of porous structures in GaSb by ion irradiation

T. Steinbach, C.C. Jacobi, W. Wesch

Ion irradiation of GaSb does not only cause defect formation but also leads to the formation of a porous structure [1-8]. To study the behaviour of this structural modification, GaSb was irradiated with 6 MeV Iodine ions. The ion fluence ranged between  $5 \times 10^{12}$  and  $6 \times 10^{15} \text{ cm}^{-2}$ . Experiments were performed with two different procedures: (CI) Continuous Irradiation of samples followed by measurements of the step height in air and (SI) Stepwise Irradiation of samples with measurements of the step height in air between subsequent irradiations. Samples were analyzed by means of surface profilometry and cross section (cleaved samples) scanning electron microscopy (cs-SEM).

In Fig. 1, the measured step height  $\Delta z$  is shown as a function of the ion fluence  $N_I$  for samples irradiated continuously and stepwise. According to the different irradiation procedures, CI and SI, and different magnitudes of swelling the graph can be divided into three parts. In part I, both irradiation procedures result in the same step height and  $\Delta z$  increases linearly up to an ion fluence of  $1.5 \times 10^{14} \text{ cm}^{-2}$  resulting in a step height of  $3 \mu\text{m}$ . For higher ion fluences, the two procedures CI and SI seem to have a different influence on the magnitude of swelling. In part II, the step height increases linearly, but steeper as in part I, and seems to end at a limit of  $32 \mu\text{m}$  for continuously irradiated samples. This step height is nearly eighteen times larger than the projected ion range. In contrast to this development, the step height decreases from  $3$  to  $1 \mu\text{m}$  with increasing ion fluence for samples irradiated stepwise, as can be seen in the curve in part III. This decrease results in a minimum at  $6 \times 10^{14} \text{ cm}^{-2}$ . The-

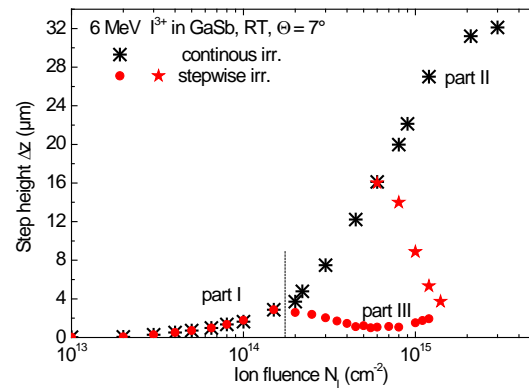


Fig. 1 Step height  $\Delta z$  as a function of the ion fluence  $N_I$  for GaSb samples irradiated with 6 MeV  $\text{I}^{3+}$  ions at room temperature according to procedure CI and SI.

reafter,  $\Delta z$  increases again with increasing ion fluence. A sample, which was continuously irradiated to an ion fluence of  $N_I = 6 \times 10^{14} \text{ cm}^{-2}$  resulting in a step height of  $16 \mu\text{m}$ , serves as a starting point for further irradiation according to procedure SI (red stars in Fig. 1). The sample was passed through a cycle containing a 30 minutes break in air and a subsequent irradiation step of an ion fluence of  $2 \times 10^{14} \text{ cm}^{-2}$ . The

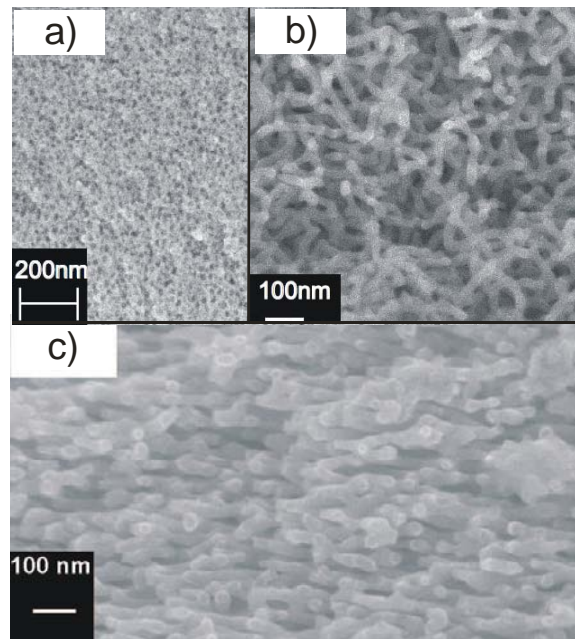


Fig. 2 Cs-SEM images of GaSb samples irradiated with 6 MeV I ions. (a) CI,  $N_I = 5 \times 10^{13} \text{ cm}^{-2}$ ; (b) CI,  $N_I = 6 \times 10^{14} \text{ cm}^{-2}$ ; (c) SI,  $N_I = 1.4 \times 10^{15} \text{ cm}^{-2}$

step height decreases from 16  $\mu\text{m}$  to 3.8  $\mu\text{m}$  in the ion fluence range of 0.6 to  $1.4 \times 10^{15} \text{ cm}^{-2}$ .

The structural evolution is shown in the SEM images in Fig. 2a - 2c. In part I, isolated, spherical voids are formed (Fig. 2a,  $N_I = 5 \times 10^{13} \text{ cm}^{-2}$ ). With increasing ion fluence, the diameter of the voids does not change, but the density of the voids rises. For ongoing continuously irradiated samples (part II) voids begin to interconnect with each other and the irradiated layer transforms into a sponge like porous structure, which consists of huge hollows and long and thin rods (Fig. 2b). At an ion fluence of  $6 \times 10^{14} \text{ cm}^{-2}$ , the rods are approximately 21 nm in diameter and  $\sim 70 - 250 \text{ nm}$  in length. This structural transformation from isolated voids into huge hollows and long rods is the reason for the extreme increase of  $\Delta z$  in the curve in part II of Fig. 1. In comparison to the rod like structures formed for continuous irradiation it is obvious that for stepwise irradiation the rods orientate parallel to the surface and the hollows between the rods shrink (Fig. 2c). Consequently, the material becomes compact again, which probably is the reason for the huge decrease of  $\Delta z$ .

Generally, the porous structures are stable with respect to measurements of the step height after a few months. Furthermore, several times of evacuation and venting of the vacuum chamber with a continuously irradiated sample do not influence the porous structure as well. Stepwise irradiations of one sample with ion fluence steps of  $1 \times 10^{14}$ ,  $2 \times 10^{14}$  and  $3 \times 10^{14} \text{ cm}^{-2}$  (final ion fluence of  $6 \times 10^{14} \text{ cm}^{-2}$ ) between subsequent breaks of 30 minutes within the evacuated irradiation chamber lead to the same step height of 16  $\mu\text{m}$  as a sample which was irradiated continuously to an ion fluence of  $6 \times 10^{14} \text{ cm}^{-2}$ .

In order to investigate the dependence on the gas atmosphere, a sample was exposed to an Ar-atmosphere with subsequent irradiation. The resulting step height shows the same decrease like that of samples, which were exposed to air/oxygen (Fig. 1).

A sample has to be in contact with gas and has to be irradiated a second time to see a decrease in  $\Delta z$  instead of an increase. We can exclude chemical reactions with oxygen, other elements of the air or Iodine as the reason for this effect. Exposure to air leads to a perpendicular orientation of the rods to the ion beam direction after an additional irradiation. Nevertheless, the reason for this change of the behaviour of GaSb after exposure to air is still unknown.

presented at IBMM2010, Montreal

Work supported by BMBF, contract no. 05KK7SJ1.

## References

- [1] R. Callec, P. N. Favennec, M. Salvi, H. L'Haridon, M. Gaunea, *Appl. Phys. Lett.* 59 (1991) 1872.
- [2] R. Callec, A. Poudoulec, *J. Appl. Phys.* 73 (1993) 4831.
- [3] R. Callec, A. Poudoulec, M. Salvi, H. L'Haridon, P. N. Favennec, M. Gaunea, *NIMB* 80/81 (1993) 532.
- [4] S. M. Kluth, J. D. Fitz Gerald, M. C. Ridgway, *Appl. Phys. Lett.* 86 (2005) 131920.
- [5] S. M. Kluth, B. Johannessen, P. Kluth, C. J. Glover, G. J. Foran, M. C. Ridgway, *NIMB* 238 (2005) 264.
- [6] N. Nitta, M. Taniwaki, T. Suzuki, Y. Hayashi, Y. Satoh, T. Yoshiie, *Materials Transactions* 43 (2002) 674.
- [7] N. Nitta, M. Taniwaki, Y. Hayashi, T. Yoshiie, *Physika B* 376-377 (2006) 881.
- [8] T. Yoshiie, N. Nitta, M. Taniwaki, *NIMB* 255 (2007) 120.



# In-situ RBS channelling studies of ion implanted semiconductors and insulators

E. Wendler

There is a continuous interest to study the defect production in various ion implanted materials and to understand their different susceptibility to ion beam induced damage formation. Very low irradiation temperatures and in situ techniques are the matter of choice in order to minimize the influence of thermal effects. Here Rutherford backscattering spectrometry (RBS) is used, which can be performed immediately after implantation without changing temperature and environment of the samples [1, 2].

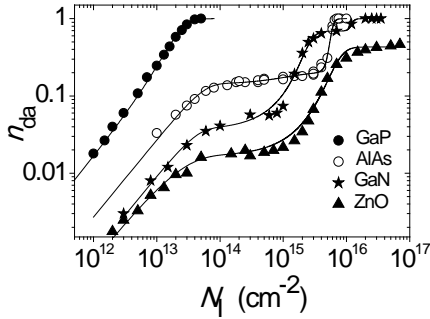


Fig. 1: Relative defect concentration in the maximum of the measured distribution,  $n_{da}$ , versus the ion fluence  $N_I$  for Ar ion implantation in various materials at 15 K [3]).

Figure 1 shows the relative defect concentration obtained by RBS versus the ion fluence for Ar ions implanted into various materials at 15 K. These damage production curves can be represented by simple models thus providing information about the mechanisms of damage formation and amorphisation (see e.g. [4, 5]). In GaP amorphisation of the implanted layer (characterised by  $n_{da} = 1$ ) is obtained by accumulation and growth of damage produced by direct ion impacts. In the case of the other examples in Fig. 1 the occurrence of a plateau at  $n_{da} \approx 0.03 \dots 0.2$  indicates a balance between defect formation and recombination. In AlAs and GaN amorphisation is reached at relatively high ion fluences, being strongly supported by the implanted ions themselves. Contrary, ZnO is very resistant to ion induced damage formation and does not amorphise for Ar ion fluences as high as  $5 \times 10^{16} \text{ cm}^{-2}$ . In GaN and ZnO a second intermediate plateau at  $n_{da} \approx 0.4 \dots 0.6$  is observed which can be attributed to the formation of non-recombining defect clusters which are extended defects [3]. At very

low ion fluences a linear increase of the defect concentration  $n_{da}$  with ion fluence  $N_I$  occurs provided the defects remaining after relaxation of the primary collision cascades do not anneal during further implantation. In Fig. 1 one can recognize such an increase for all examples and the cross section of damage formation per incident ion,  $P$ , is obtained by fitting the model curves to the experimental data [3, 4]. In a first approximation  $P$  is given by  $P \approx n_{da}^{\text{ion}} A_I$  with  $n_{da}^{\text{ion}}$  being the defect concentration produced by a single ion in crystalline material and  $A_I$  the area damaged by one ion projected to the surface. Assuming each ion to produce an amorphous cluster,  $n_{da}^{\text{ion}} = 1$  is valid and  $A_I$  as well as the diameter  $d$  of the clusters produced by one ion can be estimated.

substrate	$P$ (cm <sup>2</sup> )	$d$ (nm)	$a_0$ (nm)
GaP	$1.6 \times 10^{-14}$	1.43	0.545
AlAs	$3.5 \times 10^{-15}$	0.67	0.566
GaN	$9.5 \times 10^{-16}$	0.35	0.319
ZnO	$2.3 \times 10^{-16}$	0.17	0.325

Table 1: Cross section of damage formation,  $P$ , diameter of the clusters produced by single Ar ions,  $d$ , and lattice constant  $a_0$ .

Comparing  $d$  with the lattice constant  $a_0$  (see Table 1) it is obvious that only in the case of GaP the clusters are large enough to define an amorphous state. In the other three examples the assumption of  $n_{da}^{\text{ion}} = 1$  cannot be valid, which means that in these cases a single ion impact produces only point defects or clusters of them. This is consistent with the conclusion given above, because already existing point defects can recombine with those produced by subsequent ion impacts.

References:

- [1] High Energy Ion Beam Analysis, Eds G. Götze and K. Gärtner, Akademie-Verlag Berlin 1988.
- [2] B. Breger, E. Wendler, W. Trippensee, Ch. Schubert, W. Wesch, Nucl. Instr. and Meth. B 174, 199-204 (2001).
- [3] E. Wendler, CAARI 2010 Proceedings, AIP Conference Proceedings, April 2011, Volume 1336 (in press).
- [4] E. Wendler, Nucl. Instr. and Methods B 267 (2009) 2680.
- [5] W. J. Weber, Nucl. Instr. and Methods B 166-167 (2000) 98.

# Luminescence properties of terbium doped zinc sulphide nanowires

F. Riedel, S. Geburt, C. Ronning

Semiconductor nanowires have the potential for fundamental future application in optoelectronic devices to act e.g. as nanoscaled light emitters (LED) or waveguides [1-2]. Doping them with rare earth elements could offer new optical properties. Terbium doped ZnS is already used as a green phosphor and has been studied in electroluminescent thin films [3]. But there are no investigations on Tb doped ZnS nanowires yet.

## Experimental

ZnS nanowires were grown via VLS mechanism in a tube furnace at 1050 °C, using a 5 nm gold layer as catalyst. Characterization with SEM showed that the nanowires have a length of about 60-100 µm and a diameter of 100-400 nm. The doping with Tb was realized using ion implantation at ROMEIO. The implantation profile was simulated with SRIM [4], such as a homogeneous doping profile up to a depth of 120 nm was established. The Tb fluence implanted corresponds to a concentration of 0.2 at%. Investigations of the optical properties were done with cathodoluminescence at 5 K and a new-established photoluminescence system at different temperatures.

## Results and discussion

Directly after implantation, a strong luminescence could be measured from the samples. The spectra show several peaks, which could be identified as intra-4f-transitions of Tb<sup>3+</sup> in ZnS (see Fig. 1). An annealing at 600°C in vacuum increases the luminescence intensity for the transitions by a factor of 100. Higher temperatures result in destruction of the nanowires.

Codoping with F improves luminescence intensity for thin films, due to the formation

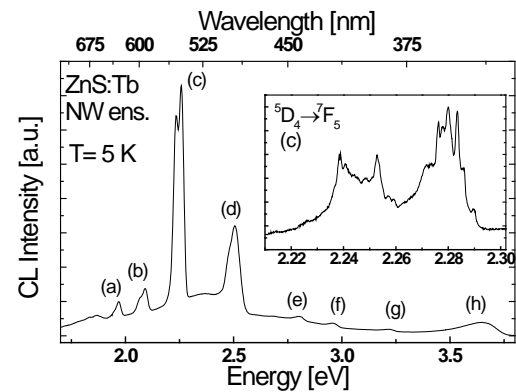


**Fig. 1:** CL spectra of Tb-implanted ZnS-nanowire-ensemble. The peaks (a) – (d) belong to intra-4f-transitions  $^5D_4 \rightarrow ^7F_j$ , for  $j = 3, \dots, 6$ , and (e) – (g) to  $^5D_3 \rightarrow ^7F_j$ , for  $j = 4, \dots, 6$ , whereas (h) is the near-band-edge-emission of ZnS. The inset shows several Stark-level-transitions of (c) in high resolution.

of lumogen centers [5]. This was also studied for the nanowires, implanting two samples additionally with 0.2 and 0.6 at% F. Unfortunately, the intensity in these samples reached only the same value as the samples without F after annealing at 500 °C, so no improvement in luminescence intensity could be achieved.

First luminescence measurements at the PL-setup could be performed. High resolution spectra show more Stark-Level-transitions within the  $^5D_4 \rightarrow ^7F_5$  transition than with CL (see inset of Fig. 1). The luminescence intensity is decreasing at higher temperatures, but still strong at room temperature, making nanostructures of this material system very interesting for applications.

## References

- [1] Zimmler et al., Appl. Phys. Lett. 94, 241120 (2009)
- [2] Voss et al., Nanolett. 7, No. 12, 3675–3680 (2007)
- [3] Adachi et al., Jpn. J. Appl. Phys. 47-1, 83-86 (2008)
- [4] Ziegler et al., *The Stopping and Range of Ions in Solids*, Pergamon Press (1985)
- [5] Okamoto et al., Appl. Phys. Lett. 49, No. 10 (1986)

# Q-factor measurements of Calcium Fluoride at low temperatures

C. Schwarz, D. Heinert, G. Hammond\*, P. Seidel and R. Nawrodt

\* SUPA, School of Physics and Astronomy, University of Glasgow, G12 8QQ Glasgow, UK

Calcium fluoride ( $\text{CaF}_2$ ) is a very attractive material for optical and opto-mechanical applications due to its excellent thermal, mechanical and optical properties. Its high mechanical Q-factor throughout a wide range of temperatures makes it interesting for high precision experiments such as gravitational wave detectors [1], laser stabilisation cavities [2] and Quantum Non-Demolition measurements utilising whispering gallery mode resonators. For these applications the Brownian thermal noise of the optical components is directly related to the mechanical loss of the materials if the mechanical loss is spatially homogeneously distributed [3]. Although the optical, dielectric and thermal properties of  $\text{CaF}_2$  are well known the mechanical loss (by means of Q-factor measurements) has not been studied in detail. Such measurements are essential in order to fully realise the suitability of this material for future applications where low thermal noise is an essential requirement.

We present the measurement of the mechanical Q-factor over a temperature range from 5 to 300 K in a frequency range from 31 to 43 kHz.

The sample used in our investigations was a  $\text{CaF}_2$  single crystal grown by Schott Lithotec. The sample had a cylindrical geometry with a diameter of 75 mm and a length of 75 mm. The symmetry axis of the cylinder was parallel to the [100] axis of the single crystal. All surfaces, including the front and back as well as the barrel, were polished to optical quality by Hellma Optics [4].

The Q-factor of the sample was investigated by exciting mechanical resonant vibrations with the corresponding frequency  $f$  and recording their subsequent free ring down. A

comb-like electrostatic drive plate was used to drive the sample close to or at the resonant frequency. The vibration of the sample was detected interferometrically with a commercial laser vibrometer. The read-out direction was in parallel to the symmetry axis of the cylinder. The crystal was suspended by means of a 50  $\mu\text{m}$  diameter tungsten wire around its central plane to decouple the sample from seismic disturbances. This provides a suspension system which has the least possible interaction with the resonant modes under investigation. The mechanical Q-factor of a resonant mode with the frequency  $f$  can be calculated by:

$$Q = \varphi^{-1} = \tau \pi f ,$$

where  $\tau$  is the time for an amplitude decay to  $1/e$  of its initial value after the excitation. The Q-factor of a resonant system is the inverse of the mechanical loss  $\varphi$ .

The whole setup was inserted into a cryostat in order to measure the Q-factor at temperatures between 5 and 300 K. The probe chamber was evacuated to better than  $10^{-3}$  Pa to minimize any additional damping due to the presence of residual gas. The temperature was sensed with a second sample of the same geometry and material. Due to a symmetric arrangement of both samples inside the probe chamber an accuracy of about 0.3 K was reached. Each mode was measured several times and the highest mechanical Q-factor obtained for all runs at a given temperature was considered to be the most reliable value. A typical measuring time of about 20 minutes per mode is needed for each temperature step. The temperature is then varied and a new measurement started. Further details of the

setup and the measuring procedure can be found in [5].

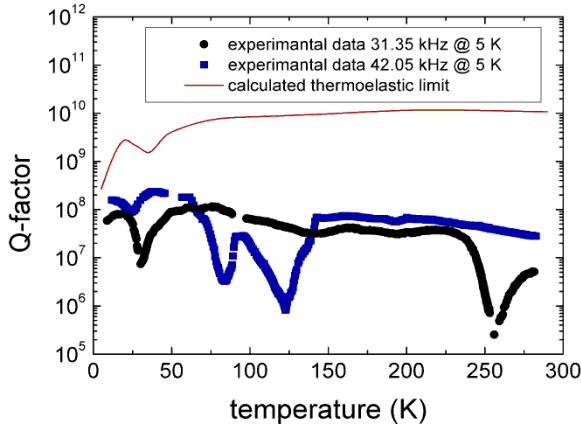


**Figure 1** Temperature dependent comparison of the experimental Q-factor data obtained for two modes and their lowest expectable thermo-elastic limit for the CaF<sub>2</sub> sample.

Figure 1 shows the measured mechanical loss of the CaF<sub>2</sub> sample between 5 and 300 K for two resonant modes (31.35 kHz and 42.05 kHz). The straight brown line represents the calculated thermo-elastic limit for the 31 kHz-mode. This mode showed the lowest thermo-elastic limit for all modes under investigation and can thus be seen as a lower limit. As the temperature is reduced from 300 to 50 K the Q-factor of the observed modes increases by roughly one order of magnitude. Both modes show dips in the mechanical loss at around 87 K, 120 K and 255 K which are caused by a resonant coupling between the samples and the violin modes resonances in the suspension wire. This was verified by changing the length of the suspension wire and observing the dips shifting to different temperatures. At approximately 25 K a dip in the Q-factor appeared. In contrast to the dips at higher temperatures this one was present in every measured mode at slightly different temperatures. An important contribution to the overall Q-factor in crystalline materials is thermo-elastic damping. Here, the local vol-

ume change caused by deformation over an oscillation cycle results in local temperature fluctuations. These fluctuations lead to a dissipative heat flux which extracts vibrational energy. To calculate the influence of the thermo-elastic damping the heat equation needs to be solved using the COMSOL finite element package. The Q-factor can then be related to the energy loss  $\Delta E$ , dissipated during one cycle of oscillation using:

$$Q^{-1} = \frac{1}{2\pi} \frac{\Delta E}{E_{tot}} = \frac{1}{4\pi f T_0 E_{tot}} \int \lambda (\nabla T)^2 dV,$$

where  $E_{tot}$  represents the total elastic energy of the mode,  $T$  is the internal temperature distribution with average value  $T_0$ ,  $f$  is the oscillation frequency and  $\lambda$  is the thermal conductivity. The integration in this equation was numerically evaluated over the whole volume of the sample to provide the results plotted in fig. 1. It is clear from this figure that thermo-elastic damping will only be significant at very low temperatures.

We have observed various dips in the temperature dependent Q-factor of a CaF<sub>2</sub> single crystal in a temperature range from 5 to 300 K. All dips above 50 K could be identified by resonant coupling between the samples and the suspensions vibrational modes. The dip around 25 K can be explained by a thermally activated dissipation process which is currently under investigation [6].

This work was supported by the DFG under contract SFB Transregio 7.

## References

- [1] P. Amico et al., Rev. Sci. Instrum. 73 (2002) 179.
- [2] A. A. Savchenkov et al., J. Opt. Soc. Am. B 24 (2007) 2988.
- [3] Y. Levin, Phys. Rev D 57 (1998) 659.
- [4] <http://www.hellma-optics.de>
- [5] R. Nawrodt et al., Eur. Phys. J. Appl. Phys. 38 (2007) 53.
- [6] C. Schwarz et al., physica status solidi (RRL) (submitted).

# Cryogenic Current Comparator

R. Geithner, R. Neubert, W. Vodel, and P. Seidel

For the recently launched FAIR (Facility for Antiproton and Ion Research) project [1] at GSI Darmstadt an improved low temperature dc Superconducting Quantum Interference Device (LTS SQUID) based Cryogenic Current Comparator (CCC) for non-destructive beam monitoring should be developed. Furthermore the CCC in a project with DESY Hamburg was completed and tested. It was used as a monitor for dark currents for Tera Electron Volt Superconducting Linear Accelerator (TESLA) cavities and therewith as a quality check of these cavities [2].

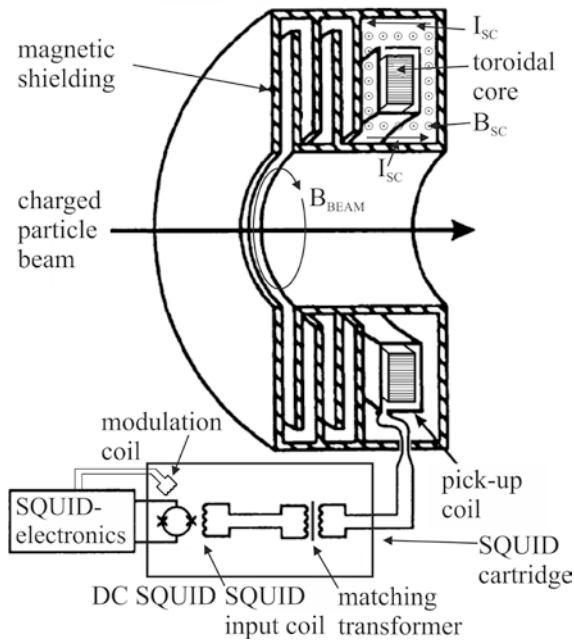


Fig. 1 Schematic diagram of the CCC. The superconducting hollow cylinder with magnetic shielding, the superconducting toroidal pick-up coil with ferromagnetic core, the superconducting matching transformer and the SQUID read-out components are all shown.

In the CCC, an ion beam current  $I_{Beam}$ , which flows through a superconducting hollow cylinder is transformed via a superconducting toroidal pickup coil with a ferromagnetic core and a matching transformer into a current which is fed through the

input coil of the readout DC SQUID *UJ 111* [2], [3].

The sensitivity ultimately depends on the pickup coil. It was demonstrated [4] that the use of a ferromagnetic core leads to a possible optimization for better noise performance using materials with a high relative permeability  $\mu_r$ .

The temperature and frequency dependent measurements of the relative permeability  $\mu_r$  and the noise contribution of several samples of ferromagnetic materials have shown that the nanocrystalline Nanoperm [5] has some advantages over amorphous Vitrovac and nanocrystalline Vitroperm [6] regarding the usage as core material for the pickup coil of a CCC. Referring to our measurements [4] Nanoperm shows a higher relative permeability  $\mu_r$  which is less frequency dependent and has a lower noise contribution than Vitrovac or Vitroperm. Although the measurements were done on small samples, we needed cores with much larger dimensions for the CCC in the FAIR project. In this CCC the core for the pickup coil will have an outer diameter of 260 mm, an inner diameter of 205 mm and a height of 97 mm. Three cores with these dimensions were delivered by Magnetec and the magnetic properties were measured in a wide neck cryostat at GSI Darmstadt. The frequency dependent serial inductance and the serial resistance were measured with an Agilent E4980A LCR-Meter as described in [4]. The measurements were done at room temperature, in liquid nitrogen at 77 K and in liquid helium at 4.2 K. All measured cores have shown the expected properties. The change of the inductance factor  $A_L$ , which means inductance of a coil on the tested core divided by the square of the number of turns, is very low in the frequen-

cy range between 20 Hz and 10 kHz. The inductance factor  $A_L$  decreased to 65 % with decreasing temperature from 300 K to 4.2 K (see Fig. 2).

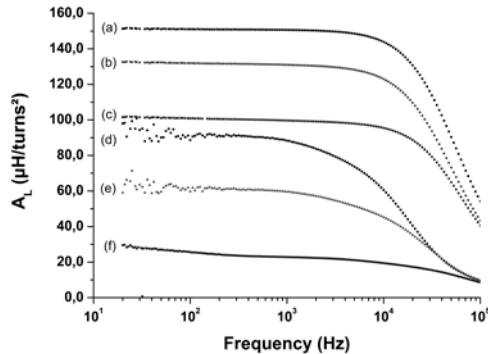


Fig. 2 Inductance factor  $A_L$  at different temperatures of Nanoperm M-764-01 core 2 [(a) 300 K; (b) 77 K; (c) 4.2 K] and DESY-CCC pickup coil (Vitrovac 6025) [(d) 300 K; (e) 77 K; (f) 4.2 K].

The Nanoperm core had a four times higher inductance factor  $A_L$  at 4.2 K than the currently used Vitrovac core within the DESY-CCC.

The above mentioned pickup coil was used in a CCC for measurements of dark currents of TESLA cavities. It was completed at the end of 2009 and was successfully tested at the beginning of 2010 in the Horizontal Bi-Cavity Test Facility (HoBiCaT) at Helmholtz-Zentrum Berlin (HZB).

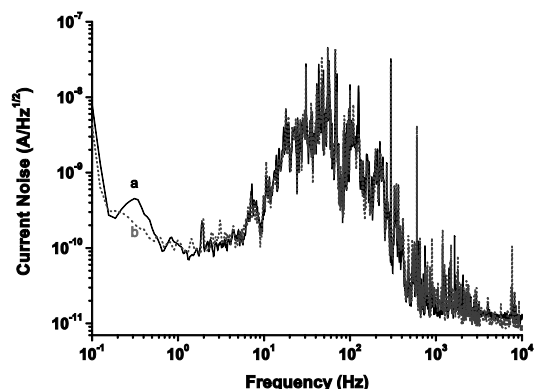


Fig. 3 Spectral current noise distributions of the CCC at HZB without acceleration field [curve (a); black], and with acceleration field [curve (b); light gray, dotted; no additional noise contribution].

The measurements were carried out in an extremely noisy accelerator environment. The noise-limited current resolution under

these extremely rough conditions was measured to be  $0.2 \text{ nA/Hz}^{1/2}$  for frequencies below 5 Hz [7]. In the frequency range between 5 Hz and 500 Hz the noise increased to  $50 \text{ nA/Hz}^{1/2}$  due to external disturbances.

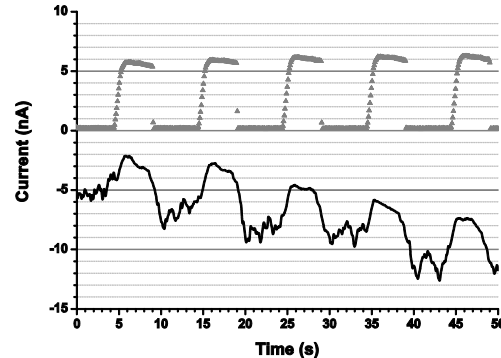


Fig. 4 Dark current of approximately 5 nA measured with the CCC (black curve, filtered and smoothed) and an additional Faraday Cup (gray, triangles) for comparison.

These could be attributed in part to microphonic effects. An attenuation of this kind of disturbance might be achieved by fixing the disks of the meander-shaped shielding against each other.

Nevertheless the non-destructive detection of dark currents down to 5 nA with an accuracy of a few nA in an accelerator environment was successful. The ferromagnetic core material Nanoperm M-764-01 and the experiences from the DESY project will provide further improvements for the new version of the CCC.

## References

- [1] Facility for Antiproton and Ion Research (FAIR), homepage available: <http://www.gsi.de/fair/>.
- [2] W. Vodel et al., *Supercond. Sci. Technol.*, 20, (2007), 393.
- [3] W. Vodel, K. Mäkinen, *Meas. Sci. Technol.*, 3, (1992), 1155-1160.
- [4] R. Geithner et al., *Applied Supercond. Conf.*, (2010), Washington, USA, to appear in *IEEE Trans. Appl. Supercond.* (2011).
- [5] MAGNETEC GmbH, Industriestrasse 7, D-63505 Langenselbold, Germany.
- [6] VACUUMSCHMELZE GmbH & Co. KG, Gruener Weg 37, D-63450 Hanau, Germany.
- [7] R. Geithner et al., *Rev. Sci. Instrum.*, 82, (2011), 013302.

# Elastic resonance spectrum of bonded crystalline silicon samples

D. Heinert, C. Heilmann, C. Schwarz, G. Hofmann, J. Komma,  
A. Grib\*, P. Seidel and R. Nawrodt

\*Physics Department, Kharkov National University, 61077 Kharkov Ukraine

The direct detection of gravitational waves represents one of today's major international efforts in fundamental physics. Their tiny effect on spacetime is to be measured in large-scale interferometers distributed around the world (e.g. [1]). Present detectors use fused silica substrates with dielectric mirrors to realise the optical components. Unfortunately, these coatings possess high mechanical losses. The Fluctuation-Dissipation theorem [2] reveals a direct link between Brownian noise and the dissipation of energy. In the end the coatings emerge to significantly increase the noise spectrum of the whole detector in its detection band ranging from 50 Hz to 2 kHz.

One possibility to circumvent coating Brownian noise can be found in the use of monolithic waveguide mirrors [3] for future generations of detectors. These future detectors should run at cryogenic temperatures with crystalline silicon substrates to reduce thermal noise [4]. Due to the fabrication process the waveguide mirrors cannot be produced directly on top of a thick substrate. Therefore they have to be bonded onto a silicon substrate after fabrication. Additionally, suspension elements have to be bonded to the substrates.

The bonding layer is known to introduce additional noise into the system. For thermal noise estimates a measurement of the mechanical loss of the bond layer  $\phi_B$  is essential.

One experimental approach suggests to measure the mechanical loss of two bonded silicon substrates  $\phi_M$  and compare it to a monocrystalline sample of the same geometry  $\phi_S$ . With the energy in the substrate  $E_S$

and in the bond  $E_B$  one can calculate the bond loss as

$$\phi_B E_B = \phi_M (E_B + E_S) - \phi_S E_S. \quad (1)$$

The mechanical loss coefficient also includes surface losses [5] which strongly depend on the measured mechanical mode. Thus to use eq. (1) it is necessary to ensure that both samples show the same mode shape. The same argument is valid for the mechanical energy stored in the bonding layer as it also enters eq. (1). A misalignment of the sample during the bonding process could provide a deviation in the energy distribution and the mode shape as well. Consequently we investigate the effect of the misalignment in this work.

For our analysis we use the FEA package ANSYS [6]. We further assume two silicon cylinders with a diameter of 65 mm and heights of 50 mm and 70 mm, respectively. The cylindrical axis of both samples is oriented along the crystalline (111) direction and they are bonded at their planar face. To account for a rotation  $R_{ij}$  in the analysis we have to calculate the tensor of elastic constants  $C_{ijkl}$  in a rotated coordinate system. Tensor laws predict

$$C_{ijkl}^R = R_{\bar{i}\bar{i}}^{-1} R_{\bar{j}\bar{j}}^{-1} R_{\bar{k}\bar{k}}^{-1} R_{\bar{l}\bar{l}}^{-1} C_{\bar{i}\bar{j}\bar{k}\bar{l}}. \quad (2)$$

ANSYS expects elastic constants in a Voigt scheme, which slightly deviates from the common definition (see Tab. 1).

Tensor index	11	22	33	23	13	12
Voigt index	1	2	3	4	5	6
Anslys' index	1	2	3	6	4	5

Tab. 1 This table shows the index definition of the Voigt notation with respect to the tensor of elastic constants. Note that the FEA package ANSYS uses a different definition.

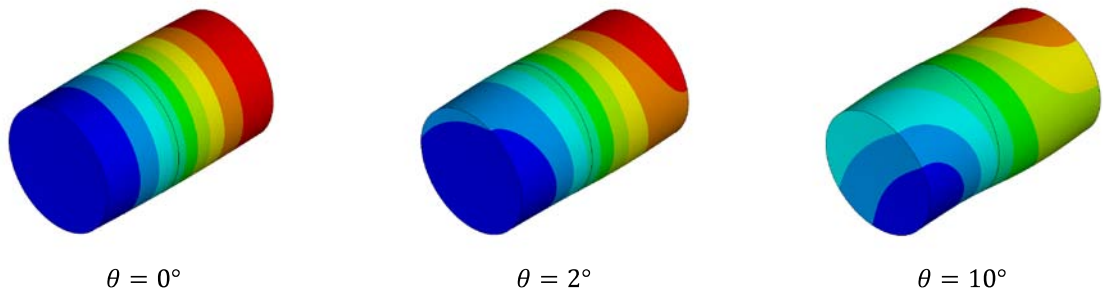


Fig. 2: Mode shape dependence on the misalignment angle  $\theta$  for the mode at  $f = 37.1$  kHz („breathing mode”). The figures show the substrate displacement along the cylindrical axis. Red and blue regions move most while green regions are at rest. The black circle in the middle of the substrate indicates the bond position.

In a first calculation we investigated changes in the eigenfrequency and mode shape with respect to misalignment. For this calculation we were able to neglect the bond layer with its characteristic length of 100 nm as it is small compared to the sample’s length. Our analysis addressed all eigenmodes with a frequency up to 80 kHz. The results for two resonant frequencies are shown in Fig. 1.

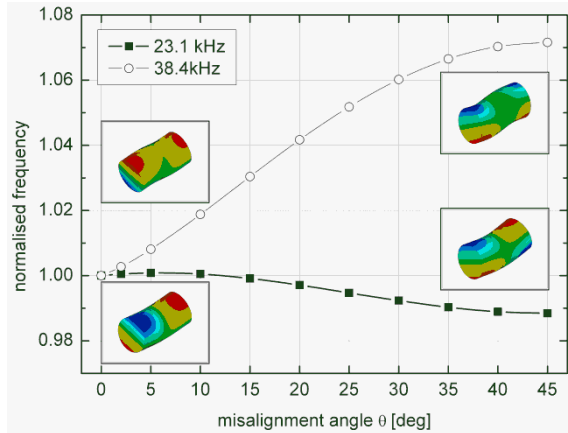


Fig. 1: Resonant frequency change due to a rotational misalignment between the bonded cylinders. The frequency in the legend is valid for no misalignment, i.e.  $\theta = 0^\circ$ . The insets show the mode shapes at  $0^\circ$  and  $45^\circ$  for both modes.

The circles indicate the mode with the highest relative frequency change due to misalignment while squares show an insensitive mode. Interestingly both modes are bending modes, i.e. the main tensions occur along the cylindrical axis. Please note the rotation of the mode shape given in the inset due to the rotation of the major cylinder.

Next to a rotation of the elastic mode a deformation should also be considered. Fig. 2 illustrates this fact on a mode at frequency  $f=37.1$  kHz.

Secondly, we ran a FEA with a bond layer connecting the bulk silicon samples. Analysing the ratio of elastic energy of the bond and total elastic energy with respect to a rotation revealed only minor changes. For the first eight eigenmodes and rotations below  $10^\circ$  the change proved to be less than 10%. This work determined the frequency shift due to misalignment to be below 8% for modes below 80 kHz. We also obtained variations of the energy stored in the bond to be smaller than 10% for the first eight eigenmodes. Consequently, the proposed scheme of bonded silicon masses appears to be valid for bonding loss measurements.

This work was supported by the DFG under contract SFB Transregio 7. The ongoing experimental part is done in close collaboration with the Institute for Gravitational Research in Glasgow.

## References

- [1] D. Sigg et al., *Class. Quantum Grav.* **25** (2008) 114041.
- [2] H. B. Callen and T. A. Welton, *Phys. Rev.* **83** (1951) 34.
- [3] F. Brückner et al., *Phys. Rev. Lett.* **104** (2010) 163903.
- [4] M. Punturo et al., *Class. Quantum Grav.* **27** (2010) 194002.
- [5] R. Nawrodt et al., arXiv:1003.2893 (2010).
- [6] <http://www.ansys.com>.



## Principles and methods for Q-factor measurements of cantilevers

G. Hofmann, J. Komma, C. Schwarz, D. Heinert, G. Hammond\*, R. Nawrodt and P. Seidel

\*Institute for Gravitational Research, University of Glasgow, G12 8QQ Glasgow/UK

The detection of gravitational waves is one of the biggest aims in science today. To detect such waves large Michelson interferometers with arm lengths up to several kilometers were built and are operating on several locations around the globe [1-4].

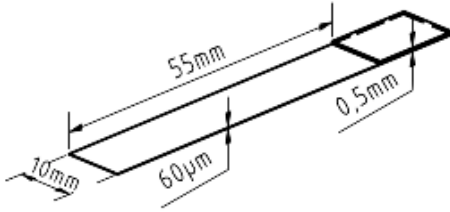


Fig. 1 Schematic drawing of a thin silicon cantilever used in the experiments. The thicker end is for clamping. The thin flexure is coated with the material under investigation.

One crucial sensitivity limit of these detectors is the thermal noise of the optical components [5]. In order to reduce this thermal noise it is necessary to use high-Q materials for the bulk and the coating material. The investigation of the coating dissipation mechanisms utilizes silicon cantilevers [6] as shown in Fig. 1.

The mechanical loss is measured in a ring-down experiment. Thus, the cantilever has

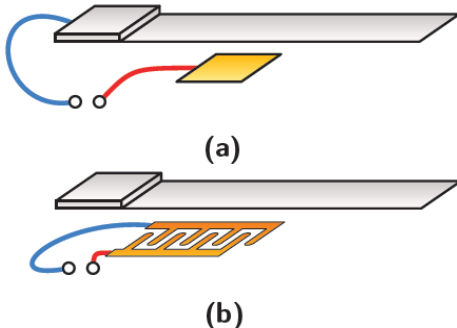


Fig. 2 Electrostatic excitation in combination with a conductive (a) and a dielectric (b) cantilever.

to be excited with one end clamped. The excitation can be done either by using a mechanical coupled piezo element or by

an electrostatic actuator as shown in Fig. 2 with the driving force:

$$F \sim \frac{dC}{dx} U^2. \quad (1)$$

The mechanical loss is obtained from the mechanical Q-factor of the oscillator. Mechanical loss  $\varphi$  and Q-factor are related to each other:

$$\varphi = Q^{-1}. \quad (2)$$

In order to determine the Q-factor one has to measure the frequency  $f_R$  and the bandwidth  $\Delta f$  of the resonance. The Q-factor is then given by:

$$Q \approx \frac{f_R}{\Delta f}. \quad (3)$$

Especially for high-Q measurements it is a better choice to take the ring-down time  $\tau$  followed by:

$$Q \approx \pi f_R \tau. \quad (4)$$

Measurements of the resonant frequency and ring-down times rely on sensing the vibrational amplitude of the cantilever. There are two principles which provide a non-contact measurement of the amplitude – optical or capacitive – which have been investigated in detail [7].

As an established system for optical measurements a commercial laser vibrometer was used. It offers the detection of mechanical vibrations in a frequency range between 0 and 500 kHz with a resolution of better than 0.3 nm.

Another optical method uses two close photodiodes which sense the movement of the reflected laser beam from the sample surface. The signal of the two photodiode is subtracted to remove common mode signals. This setup allows measurements down to vibration amplitudes of about 5 nm.

Both easy-to-use setups are dependent on an optical access to the sample volume of the cryostat.

Especially for very low temperature investigations (mK range) this window is not appropriate due to the heat radiation. To avoid the use of this window an optical fibre could be used as shown in Fig. 3. The distance modulation between the fibre coupler and the cantilever (here simulated as a mirror) affects the retro-reflection and thus the signal detected by a photodiode.

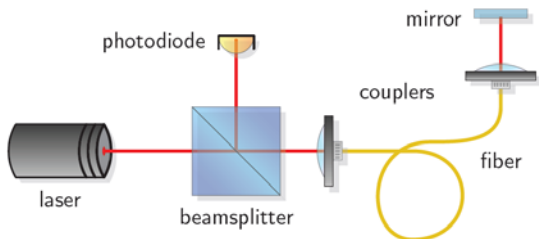


Fig. 3 Schematic drawing of the fiber read-out system. The cantilever works like a mirror whose movement modulates the signal on the photodiode due to the coupling efficiency.

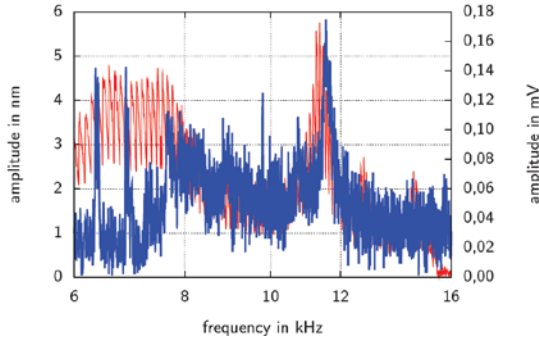


Fig. 4 Frequency spectrum of a piezo actuated mirror at 11.5 kHz. The spectrum received with the SIOS interferometer — shows the peak as well as with the fiber system —.

A second possible setup to avoid an optical viewport is a capacitive read-out. This scheme is based on the modulation of a capacitance  $C$  formed either between two plates – one of them the cantilever itself – or by a periodic array of thin wires facing the cantilever as a dielectric layer in distance  $x$ . Connected to a voltage source  $U_B$  via a resistor  $R$  we get two regimes: frequencies below  $f = (RC)^{-1}$ , constant vol-

tage (CV) and above  $f = (RC)^{-1}$ , constant charge (CC). In CV mode the resistor affects the signal and also lower frequencies reduce the signal due to:

$$\Delta U = RU_B \frac{\delta C}{\delta x} x_0 \Omega \cos(\Omega t). \quad (5)$$

In contrast the CC mode provides a signal that is independent of the biasing resistor:

$$\Delta U = \frac{U_B \delta C}{C_0 \delta x} x_0 \sin(\Omega t). \quad (6)$$

Fig. 5 shows a measured resonance peak acquired with the two photodiode system in comparison to the capacitive read out, the obtained Q-factors are in good agreement.

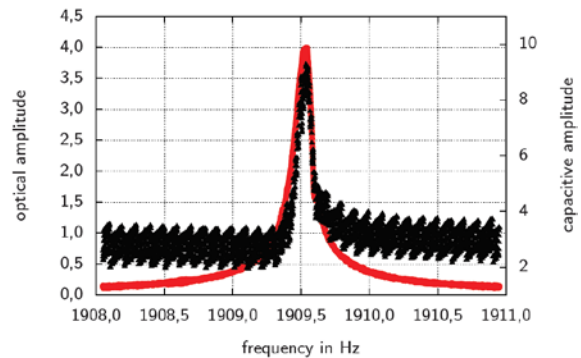


Fig. 5 Resonance peak of a cantilever mode acquired with the two photodiode system ● and with the capacitive read out ▲.

This work was supported by the German science foundation under contract SFB TR7.

## References

- [1] S. Hild, *Status of GEO 600*. 2006
- [2] D. Sigg, *Status of the LIGO detectors*, Classical and Quantum Gravity 25. 2008
- [3] G. Losurdo, *The status of VIRGO*. 2005
- [4] R. Takahashi, *Status of TAMA300*, Classical and Quantum Gravity 21. 2004
- [5] R. Saulson, *Fundamentals of gravitational wave detectors*, World Scientific, Singapore. 1994
- [6] J. Komma, *Investigation of the mechanical loss of a thin silica coated cantilever*, Jahresbericht. 2011
- [7] G. Hofmann, *Methoden und Verfahren zur Gütemessung an Cantilevern*, Studienarbeit. 2010

# Investigation of the mechanical loss of a thin silica coated cantilever

J. Komma, G. Hofmann, C. Schwarz, D. Heinert,  
G. Hammond\*, P. Seidel and R. Nawrodt  
\*Glasgow University, G12 8QQ Glasgow, UK

Modern gravitational wave detectors working like a Michelson interferometer. A laser beam senses the surface of the optical components and thus reads out its thermal noise which limits the sensitivity of the detectors. There is a great interest in materials with low mechanical loss, because the loss is directly related with the thermal noise by the fluctuation-dissipation-theorem [1].

The optical coatings consist of high and low index materials. One common material as a low index material in thin optical layers is silica (SiO<sub>2</sub>). In this work the mechanical loss of a silicon cantilever was measured which was coated with thermally grown silica. The measurements have been performed by means of a ring-down technique. The silicon cantilever is excited to resonant vibrations and the subsequent free ring-down is recorded by means of a highly sensitive vibration sensing method [2]. The loss  $\phi$  can be calculated with the resonance frequency  $f$  and the characteristic ring-down time  $\tau$  via [3]:

$$\phi^{-1} = \pi f \tau. \quad (1)$$

The ring-down time is determined as shown in figure 1 as the time to reach 1/e of the initial amplitude.

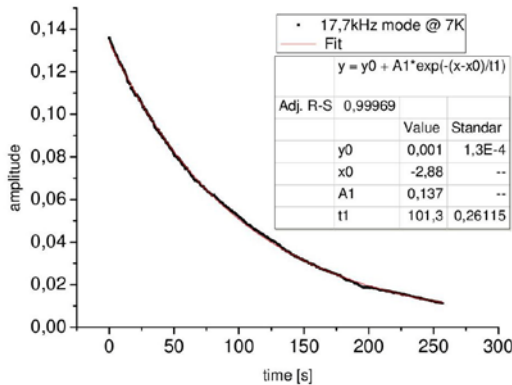


Fig 1: Typical ring-down of a silicon cantilever at 17.7 kHz and 7 K.

The direct measurement of the thin film mechanical loss is very complicated. Therefore, a differential measurement between the coated and the uncoated silicon cantilever was chosen.

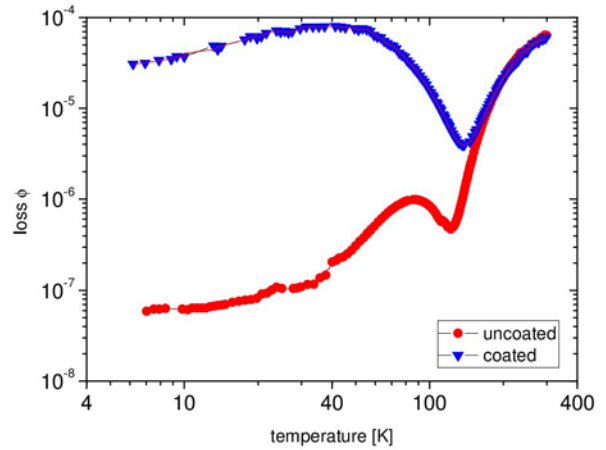


Fig 2: Measured values for the coated and uncoated silicon cantilever [4]. Coating thickness: 1.7  $\mu$ m.

Fig. 2 shows the plots for the coated and uncoated cantilever. Above 100 K both curves are dominated by thermo-elastic damping [5]. At lower temperatures the curves are different – the coated cantilever shows a higher mechanical loss. The difference between both curves corresponds to the coating loss, which is shown in Fig 3.

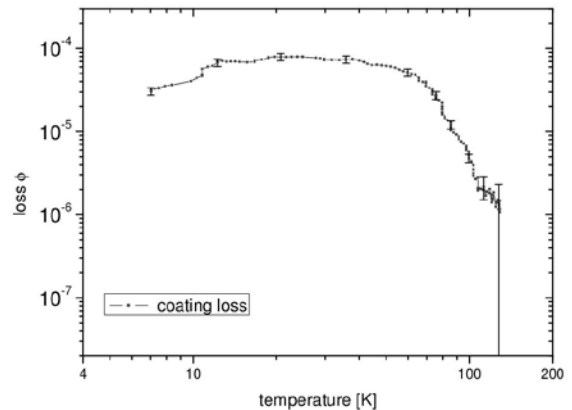


Fig 3: Coating loss of a 1.7  $\mu$ m silica layer [4].

This method gives good results below 130 K. Above this temperature the difference between the two measurements is too small to get a sufficient accurate coating loss. Below 100 K it is possible to estimate the coating mechanical loss with an uncertainty of about 10%.

In this work six different modes were evaluated. A loss peak at around 40 K is visible in the silica coating loss. The peak temperature shifts with the mode frequency. This behavior is an indication for a thermally induced relaxation process. These processes are described by a Debye-like structure:

$$\phi = \Delta \times \frac{\omega\tau}{1 + \omega^2\tau^2}. \quad (2)$$

$\Delta$  is the relaxation strength,  $\omega$  the angular frequency of the vibration and  $\tau$  the relaxation time of the process. The relaxation time is given by [6]:

$$\tau = \tau_0 \times \exp\left(\frac{E_A}{k_B T}\right), \quad (3)$$

with the relaxation constant  $\tau_0$  and the activation energy  $E_A$  of the process. These two process parameters characterize the microscopic process that is the origin of the mechanical loss causing the peak. The parameters can be obtained from an Arrhenius plot (see Fig. 4): Eq. (2) leads to the position of the loss peak at  $\omega\tau = 1$ . Using eq. (3) for  $\tau$

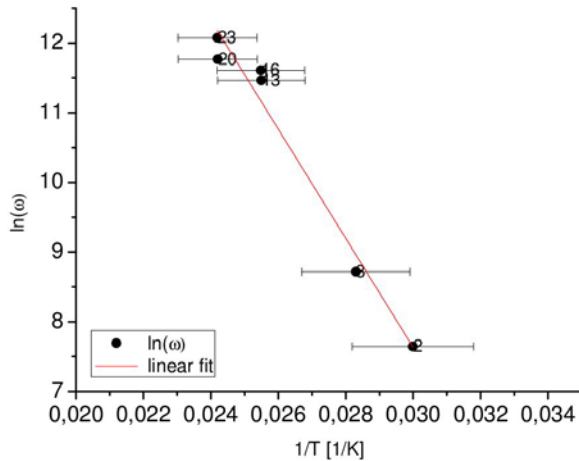


Fig 4: Arrhenius plot of the mechanical loss peak at around 40 K [4].

relates the slope of the linear fit in Fig. 3 to the activation energy  $E_A$ .

The activation energy was determined to be  $(68 \pm 6)$  meV. This energy corresponds to activation energies typically observed in structural changes in amorphous media [7]. Compared to ion-beam sputtered silica coatings the activation energy observed here is approximately twice as high.

The presented analysis of thermally grown silica coatings regarding their mechanical loss reveals a low temperature relaxation peak near 40 K that might be related to structural changes in the material. Further investigations are currently made to clarify the origin of the loss peak.

This work was supported by the DFG under contract SFB Transregio 7.

## References

- [1] H. B. Callen, T. A. Welton: Irreversibility and Generalized Noise, Phys. Rev. 83 (1951) 34-40.
- [2] G. Hofmann: Principles and methods for Q-factor measurements of cantilevers, 2010.
- [3] R. Saulson, Fundamentals of gravitational wave detectors, World Scientific, Singapore 1994.
- [4] J. Komma: Studienarbeit, 2010.
- [5] C. Zener: Internal Friction in Solids. I. Theory of Internal Friction in Reeds, Phys. Rev. 52 (1937) 230-235.
- [6] V. B. Braginsky, V. P. Mitrofanov, V. I. Panov: Systems with Small Dissipation. The University of Chicago Press, 1985.
- [7] K. A. Topp and D. G. Cahill: Elastic properties of several amorphous solids and disordered crystals below 100 K, 1996 Z. Phys. B 101 235.
- [8] I. W. Martin: Studies of materials for use in future interferometric gravitational wave detectors. PhD Thesis, Department of Physics and Astronomy, University of Glasgow, 2009.

# Compensation of thermo-elastic noise in silicon suspension elements

R. Nawrodt, C. Schwarz, J. Komma, G. Hofmann, D. Heinert, G. Hammond\*

\*SUPA, School of Physics and Astronomy, University of Glasgow, G12 8QQ Glasgow, UK

Ultra-high precision length sensing experiments like gravitational wave detectors or quantum non-demolition experiments involve highly insulated optical elements. These elements are well shielded against seismic coupling by sophisticated suspension techniques. The current optimum solution regarding seismic insulation and low thermal noise level is a monolithic suspension. This technique has been very successfully demonstrated for the GEO600 gravitational wave experiment [1].

The suspension is formed by a suspension fibre (circular diameter) or a ribbon (rectangular cross-section) and a test mass. Thermal fluctuations arising within the suspension will cause a fluctuation of the test mass and will couple into the experiment. One of the most important sources of thermal noise is thermo-elastic noise which is based on thermo-elastic dissipation.

Including second-order terms into the thermo-elastic dissipation leads to the following expression for bending beams [2]:

$$\varphi_{TE} = \frac{TY}{\rho C_V} \left( \alpha - \frac{1}{Y} \frac{\partial Y}{\partial T} \frac{\sigma}{Y} \right)^2 \frac{\omega \tau}{1 + \omega^2 \tau^2} \quad (1)$$

with the temperature  $T$  the Young's modulus  $Y$ , the mass density  $\rho$ , the heat capacity  $C_V$ , the coefficient of thermal expansion  $\alpha$ , the static stress  $\sigma$  of the beam, the angular frequency  $\omega$  and the characteristic thermal relaxation time  $\tau$ . It is obvious that the level of thermo-elastic damping is strongly dependent on the mechanical stress  $\sigma$  applied to the suspension element. If the coefficient of thermal expansion  $\alpha$  and the parameter  $\beta=1/T \partial Y/\partial T$  have the same sign it is possible to compensate the thermo-elastic contribution by setting an appropriate stress in the suspension element. This cancellation technique has been successfully applied to the 2<sup>nd</sup> generation of gravitational wave detectors like Advanced LIGO or Advanced Virgo [3, 4] by means

of using fused silica as a suspension material.

Experiments utilising cryogenic temperatures as the proposed 3<sup>rd</sup> generation GW detector "Einstein Telescope" [5] will have to use crystalline suspension elements [6] – preferably silicon suspension elements.

Silicon suspension elements can also be used for low thermal noise suspensions if thermo-elastic noise can be cancelled. Silicon provides an interesting possibility by means of its thermal properties: At two selected temperatures – around 18 and 125 K – the coefficient of thermal expansion is zero (see figure 1, [7]) and thus the linear thermo-elastic damping vanishes.

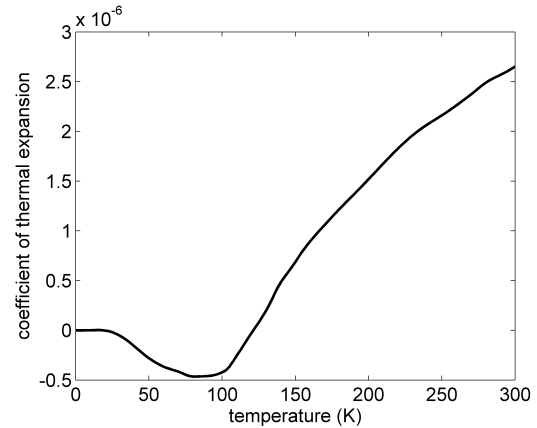


Fig. 1: Thermal expansion for silicon [7].

Operating suspension elements at these temperatures will thus cancel thermo-elastic noise as well. However, it is often not possible to operate suspension elements at a constant temperature– e.g. by means of the demand for extracting heat through the element. Here it might be possible to cancel the thermo-elastic contribution by setting an appropriate tension in the suspension (see eq. (1)). We determined the coefficient  $\beta$  from our experiments. A silicon flexure was excited to resonant vibrations at different temperatures between 5 and 300 K. The resonant frequency  $f$  of a bending mode of a bending beam with thickness  $t$  and length  $l$  is given by:

$$f(T) = \frac{1}{2\pi} \frac{\alpha_n^2 t}{\sqrt{12} l^2} \sqrt{\frac{Y}{\rho}}. \quad (2)$$

$\alpha_n$  is a numerical factor that determines the order of the mode. It can be determined from solving the transcendent equation

$$\cosh \alpha_n \cos \alpha_n = -1. \quad (3)$$

Figure 2 shows the temperature dependence of the resonant frequency of a bending mode at 16.7 kHz.

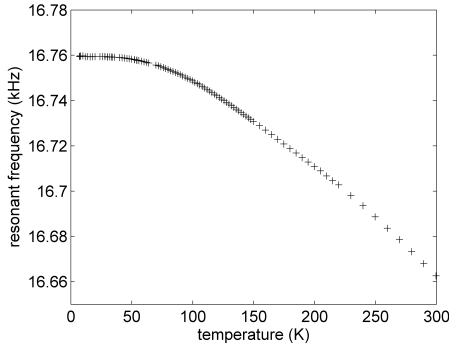


**Fig. 2:** Temperature dependence of the resonant frequency of a Si(100) flexure (length 35 mm, width 6 mm, thickness 50  $\mu\text{m}$ ).

Using eq. (2) it is possible to determine the factor  $\beta = 1/T dY/dT$  from the measured temperature dependence of the resonant frequency  $f$ :

$$\beta(T) = 2 \frac{1}{f(T)} \frac{\partial f(T)}{\partial T} \quad (3)$$

The corresponding values for  $\beta$  obtained from fig. 2 are given in fig. 3. Within the temperature range of interest between 5 and 300 K the coefficient is always negative. In order to be able to compensate the thermo-elastic loss according to eq. (1) it is necessary to have a negative coefficient of thermal expansion.

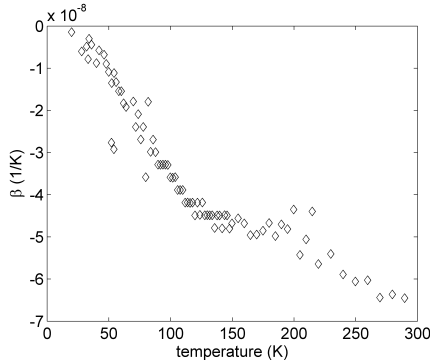


**Fig. 3:** Temperature dependence of the coefficient  $\beta = 1/T dY/dT$  for Si(100).

This demand is fulfilled in a temperature range from 18 to 125 K (see fig. 1). Here, it is possible to set a certain level of tension in a suspension element to cancel thermo-elastic noise. The tension needed for cancellation is plotted in figure 4 together with the breaking strength of silicon.

The stress needed to compensate the linear thermo-elastic effects exceeds the breaking strength in a wide range of temperatures.

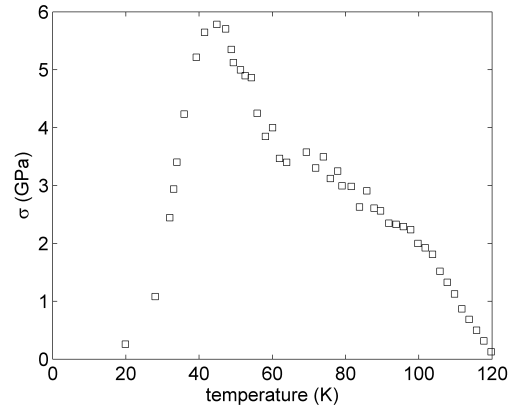


**Fig. 4:** Mechanical stress needed in the silicon based suspension element to compensate the thermo-elastic noise. The breaking strength of silicon under tension is about 2 GPa for samples with a high surface quality (no micro-cracks).

However, in a close vicinity of the two zero crossings of the thermal expansion coefficient of silicon at 18 and 125 K it is possible to compensate the thermo-elastic contribution by setting an appropriate stress.

This work was supported by the DFG under contract SFB Transregio 7.

## References

- [1] M. V. Plissi et al., Rev. Sci. Instrum. **69** (1998) 3055.
- [2] G. Cagnoli, P. A. Willems, Phys. Rev. B **65** (2002) 174111.
- [3] N. A. Robertson et al., Class. Quantum Grav. **19** (2002) 4043.
- [4] P. Amico et al., Rev. Sci. Instrum. **73** (2002) 3318.
- [5] M. Punturo et al., Class. Quantum Grav. **27** (2010) 084007.
- [6] R. Nawrodt, S. Rowan, J. Hough, M. Punturo, F. Ricci, J.-Y. Vinet, Gen. Relativ. Gravit. **43** (2011) 593.
- [7] K. G. Lyon, G. L. Salinger, C. A. Swenson, G. K. White, J. Appl. Phys. **48** (1977) 865.

# Temperature dependent magnetorelaxometry: numerical simulation of energy barrier distribution

M. Schiffler, M. Büttner and P. Seidel

Due to the thermal activation of the relaxation process in temperature dependent magnetorelaxometry (TMRX) measurements the energy barrier distribution (EBD) provides important information. The dominating contributions to the interaction between the magnetic nanoparticles as well as their size distribution can be obtained from it. On the one hand, a theory and numerical simulations for the EBD are presented in [1] calculated for arbitrarily chosen simulation parameters. On the other hand there exist an amount of TMRX measurements representing the EBD [2, 3]. These are four interesting fractions of each the sample “V190” and “DDM 128N” which are provided with information about the anisotropy constant obtained from magnetometric measurements. The simulation parameters used in the presented simulation are the reduced anisotropy constant

$$\beta = \frac{2K(T)}{\mu_0 M_S^2(0K)} \quad (1)$$

derived from the temperature dependent anisotropy constant  $K = H_C M_S$  and the 0K value of the saturation magnetization  $M_S$  (with  $H_C$  denoting the coercivity) and the particle volume concentration

$$\eta = \frac{n_{MNP} M_{MNP}}{\rho_{MNP} V_{sample}} \quad (2)$$

where we denote the iron concentration with  $n_{MNP}$ , the molar mass  $M_{MNP}$  and the density  $\rho_{MNP}$  of the material the magnetic nanoparticles consist in and the sample volume with  $V_{sample}$ . For the sample DDM

128N we obtain a particle volume concentration of  $\eta = 0.000724$  using equation (2). Due to the mixture ratio between magnetite and magnetite in the ferrofluids system V190 this value is  $\eta = 0.000814$ . For each fraction 256 simulation runs are performed for finding a pair of energy barriers. As shown in a concentration dependent simulation for two fixed fractions the energy barrier consists in the anisotropy energy narrowly distributed around a center and a broader distribution of the concentration dependent stray field energy. The simulations with a fit of the lognormal distribution to the histogram data are shown in Figure 1. The parameters used in simulation and for the fit are shown in Table 1 and Table 2.

We firstly observe that the simulations reflect the lognormal distribution of the MNP assumable in real experiments. The differences between the peaks determined by simulation and fit on the one hand and the temperature detection deviation of the TMRX measurements on the other are caused by model-like character of the simulations and the error tolerance of the lognormal fit.

In the tables the lognormal distribution is described by the median  $T_m$  and the logarithmized standard deviation  $\sigma$ . From these values the maximum value  $T_{\max,Sim} = T_m e^{-\sigma^2}$  can be calculated and compared with the experimental maximum value  $T_{\max,Exp}$ . The maximum volume  $V_{\max}$  obtained from TMRX measurements is necessary for conversion of the obtained energy barriers to a temperature value.

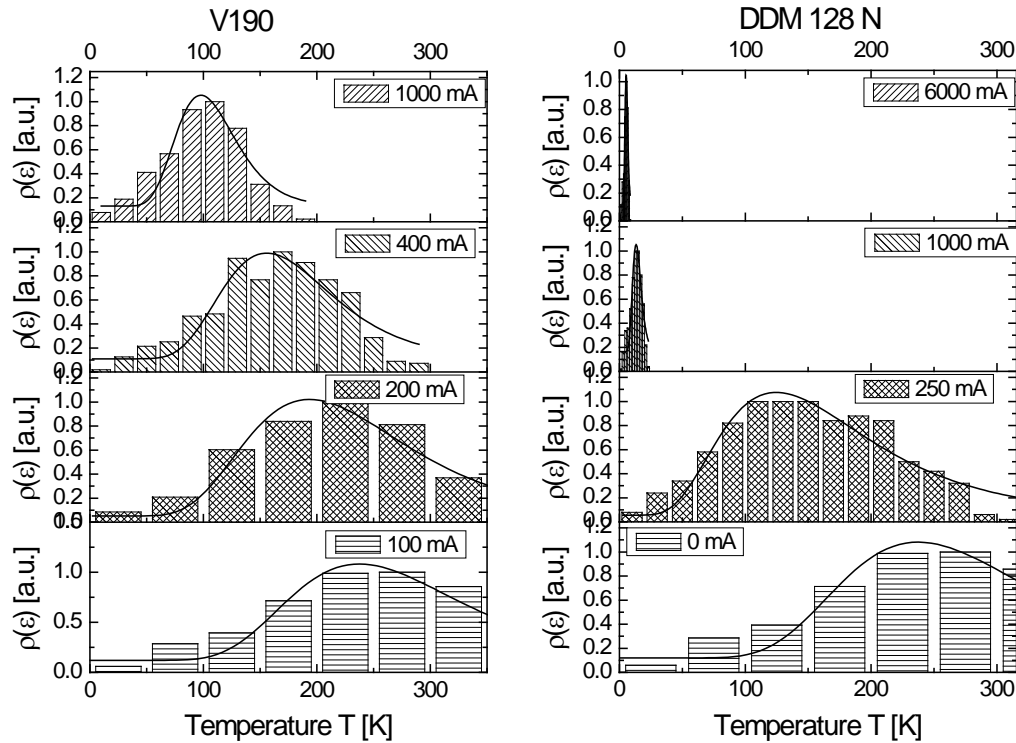


Figure 1: Simulated energy barrier distribution for the investigated ferrofluids samples. The solid lines represent lognormal curve fits.

Table 1: anisotropy data and fit parameters for the sample V190

fraction [mA]	K [kJ/m <sup>3</sup> ]	$\beta$	$V_{\max}$ [10 <sup>-25</sup> m <sup>3</sup> ]	$T_m$ [K]	$\sigma$	$T_{\max}$ Sim [K]	$T_{\max}$ Exp [K]	difference
1000	13.7	0.18551	16.9	104.24	0.397	89.10	92	-3.2%
400	12	0.16303	28.2	167.95	0.437	138.72	150	-7.5%
200	13	0.17632	39.2	222.23	0.443	182.71	190	-3.8%
100	12.3	0.16713	46.0	272.28	0.410	230.06	225	2.2%

Table 2: anisotropy data and fit parameters for the sample DDM 128N

fraction [mA]	K [kJ/m <sup>3</sup> ]	$\beta$	$V_{\max}$ [10 <sup>-25</sup> m <sup>3</sup> ]	$T_m$ [K]	$\sigma$	$T_{\max}$ Sim [K]	$T_{\max}$ Exp [K]	difference
6000	22.6	0.31120	0.61	7.58	0.242	7.15	5	43.0%
1000	19.1	0.23101	1.99	16.83	0.287	15.51	13	19.3%
250	11.4	0.15482	35.4	181.39	0.463	146.44	137	6.9%
0	11.8	0.16225	56.4	322.71	0.414	271.93	210	29.5%

In a second step the shape of the histograms were compared with the whole course of the corresponding TMRX measurement curves. It could be shown that for a certain spatial scaling of the nanoparticles the experimental data can be reconstructed by simulation. The low temperature peak discussed in [3] remains unexplained. A possible reason for this peak can be found similar to [4].

This work was supported by the BMBF project “NanoMed” 03X0104D.

## References

- [1] D. V. Berkov, Journal of Magnetism and Magnetic Materials 186 (1998) 199.
- [2] E. Romanus et al., Nanotechnology 18 (2007) 115709.
- [3] F. Schmidl et al., Journal of Magnetism and Magnetic Materials 311 (2007) 171.
- [4] M. Sasaki et al., Physical Review B 71 (2005)



# Experimental and theoretical investigation on high- $T_c$ superconducting intrinsic Josephson junctions

Alexander Grib<sup>1</sup>, Yury Shukrinov<sup>2</sup>, Frank Schmidl, and Paul Seidel

<sup>1</sup>Physics Department, V. N. Karazin Kharkiv National University, 61077 Kharkiv, Ukraine

<sup>2</sup>Joint Institute for Nuclear Research, BLTP, Dubna, 141980, Russia

The intrinsic Josephson effects [1] in the cuprates where the superconducting  $\text{CuO}_2$  - planes are coupled via non-superconducting barrier layers within the unit cell of the materials can be used to produce series junction arrays. The number of junctions depends on the thickness of the high- $T_c$  material between the electrodes. Optimization of technology and a complex control of the preparation process allows to reduce the number of junctions to a few or even a single one. There are different technologies using mesa geometry of vertical stacks, stacks grown at steps in the substrate, focussed ion beam cutted single crystal or film structures and planar "horizontal stacks" grown on vicinal cutted substrates. Additional doping or external shunting of the intrinsic arrays can be used to adjust the junction parameters or to enhance the synchronization of the junctions within the array. In this way the weak coupling is realized in a periodic stack of Josephson junctions with atomic dimensions along the crystallographic  $c$ -axis.

While the first investigations on the intrinsic junctions used single crystals or etched parts out of them, different thin film technologies have been developed meanwhile, too. Thin film structures used a mesa-type geometry where the high- $T_c$  film is patterned with lateral dimensions in the  $\mu\text{m}$ -range, e.g. [2, 3] and references therein. The problem of metal electrodes to the mesas was solved even for a four-point-measurement which requires two separated contacts on top of each mesa like in Fig. 1a, see Seidel et al. [4].

An alternative way to realize a thin film intrinsic stacked junction array uses substrates with a surface not parallel to the  $\text{CuO}_2$ -planes [5]. On such vicinal cutted

substrates the film grows with  $\text{CuO}_2$ -planes tilted with respect to the surface. Patterning of a microbridge results in a nearly horizontal stack of junctions and the length of the microbridge corresponds to the number of junctions in series, see Fig. 1b. Intrinsic Josephson behavior of the microbridges was observed for misorientation angles equal or larger than 15 degrees [6].

This kind of arrays offers new possibilities for synchronization [7].

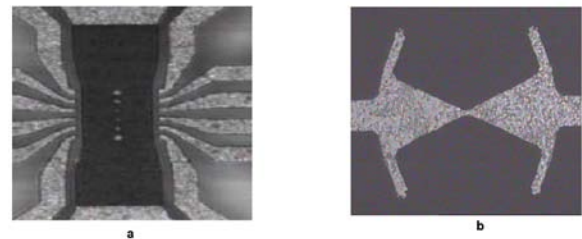


Fig.1 Two types of thin film intrinsic Josephson junctions. (a) 6 TI-2212 mesas with areas from  $2 \times 2 \mu\text{m}^2$  to  $5 \times 5 \mu\text{m}^2$  in the center of the substrate before they were covered by a gold contact which is cut by ion etching to get separate contacts for 4-point measurement; (b) the microbridge on vicinal cut substrate with a  $2 \times 2 \mu\text{m}^2$  planar stack imbedded in an antenna structure (TI-2212 on 20 degrees vicinal cut  $\text{LaAlO}_3$ )

One of the most important applications of the intrinsic Josephson effect is the construction of sub-microwave sources of coherent radiation. The common synchronizing ac current in all junctions is the condition of strong synchronization. Radiation of synchronizing junctions itself can produce this ac current if there is a feedback in the system. The existence of the current resonant mode in the system provides both the strong ac current produced by radiation of junctions and a strong feedback. Thus, an application of a

superconducting resonator is a solution to obtain synchronization of Josephson junctions. It was shown in [8] that the synchronizing ac current is largest in serial arrays of junctions. Intrinsic Josephson junctions satisfy the requested conditions and small spread of critical currents and normal resistances can be in principle achieved. We calculated the optimal parameters of the system for the shunting microbridges. The maximal tolerant spread of critical currents in this case is equal to about 26 % [8].

In our calculations, we found that the effect of the multibranch behaviour impedes synchronization and one should avoid to apply the resonant frequency in the region of the multibranch behaviour. The narrow-band synchronization of two junctions was calculated for the region of the IV-characteristic above the hysteretic region. There is a way to use the successive set of capacitances of junctions as a capacitance of the resonator. In this case junctions with the spread of critical currents of about 10% are strongly synchronized in the hysteretic region [9]. We would like to note that the frequency spectrum of radiation in the hysteretic region contains many harmonics, and the same principle as used in Ref. [9] gives the best results in the non-hysteretic region, i.e. above the characteristic frequencies of the junctions. For further details see [10].

The temperature dependence of the return current of single junction is determined by the temperature dependence of the critical current and the McCumber parameter  $\beta_C$ . For the coupled system of Josephson junctions it is additionally determined by the number of junctions in the stack, by the coupling between junctions and boundary conditions. The temperature dependence of  $\beta_C$  its turn depends on the temperature dependence of the critical current  $I_C(T)$ , junction resistance  $R_J(T)$  and capacitance  $C_J(T)$ . In [10] we assume that the capacitance of the junctions is the temperature independent geometrical capacitance  $C_J$ .

Within the capacitively coupled Josephson junctions model with diffusion current (CCJJ+DC model) [11, 12] we calculated successfully the return current and its temperature dependence [10].

## Acknowledgments

This research was partially supported by Heisenberg-Landau Program and the German Research Foundation (DFG).

## References

- [1] Kleiner R, Steinmeyer F, Kunkel G, Müller P 1992 Phys. Rev. Lett. 68 2394
- [2] Schmidl F, Pfuch A, Schneidewind H, Heinz E, Dörrer L, Matthes A, Seidel P, Hübner U, Veith M, Steinbeiss E 1995 Supercond. Sci. Technol. 8 740
- [3] Haruta M, Kume E and Sakai S 2009 Supercond. Sci. Technol. 22 125004
- [4] Seidel P, Schmidl F, Pfuch A, Schneidewind H, Heinz E 1996 Supercond. Sci. Technol. 9 A9
- [5] Chana O S, Kuzhakhmetov A R, Warburton P A, Hyland D M C, Dew-Hughes D, Grovenor C R M 2000 Appl. Phys. Lett. 76, 3603
- [6] Mans M, Schneidewind H, Buenfeld M, Schmidl F, Seidel P 2006 Phys. Rev. B 74 214514
- [7] Grib A M, Mans M, Scherbel J, Buenfeld M, Schmidl F, Seidel P 2006 Supercond. Sci. Technol. 19 S 200
- [8] Grib A N, Seidel P, Scherbel J 2002 Phys. Rev. B. 65 94508
- [9] Grib A, Seidel P 2009 Physica Status Solidi RRL 3 302
- [10] Grib, A, Shukrinov, Yu, Schmidl, F, Seidel P 2010 J.Phys. Conf. Ser. 248 012038
- [11] Machida M, Koyama T, Tanaka A and Tachiki M 2000 Physica C 85 330
- [12] Shukrinov Yu M, Mahfouzi F, Seidel P 2006 Physica C 62 449

# Preparation and characterisation of tunnelling junctions based on $\text{Ba}(\text{Fe}_{0.9}\text{Co}_{0.1})_2\text{As}_2$ -superconductor thin films

S. Döring, S. Schmidt, F. Schmidl, V. Tympel, V. Große, P. Seidel,  
S. Haindl\*, F. Kurth\*, K. Iida\*, B. Holzapfel\* and I. Mönch\*

\*IFW Dresden, Institute for Metallic Materials, Helmholtzstraße 20, 01069 Dresden, Germany

The experimental investigation of the electronic properties of iron based superconductors [1] is a helpful tool to investigate the nature of superconductivity in these materials. Tunnelling junctions offer ways to measure the energy gap(s) and the symmetry of the order parameter as fundamental properties. Previous studies on the material  $\text{Ba}(\text{Fe}_{0.9}\text{Co}_{0.1})_2\text{As}_2$  (Ba-122) show contradictory results, regarding the number of gaps as well as their  $k_B T_C$  ratio. Optical investigations shows just one gap with  $2\Delta/k_B T_C=2.1$  [2], while calorimetric measurements indicated two gaps with ratios of 1.9 and 4.4, respectively [3]. This was in good agreement with results obtained by spin resonance, where values of 1.6 and 3.8 were found [4]. The only investigation done by point contact tunnelling spectroscopy showed only one gap with  $2\Delta/k_B T_C=5.8$  [5]. In contrast to the commonly used point contact Andreev reflection studies, we used epitaxial thin films of Ba-122 to produce superconductor - normal metal - superconductor (SNS) tunnel junctions with tunable barrier properties.

The Ba-122 thin films were prepared at the IFW Dresden [6]. Using pulsed laser deposition they were grown on a 10mm x 5mm  $(\text{La,Sr})(\text{Al,Ta})\text{O}_3$ -substrate. The film thickness was about 80nm.

At the IFK the entire surface of the samples was covered with gold. Therefore we used two steps of sputtering, each with a thickness of about 5nm. While in the first one, half of the surface was covered, in the second one gold was deposited over the whole sample. This forms two regions, with

different gold layer thicknesses. This gold layer prevents oxidation of the Ba-122 and forms the future normal metal barrier of the junctions. The next step was etching the base electrode with dry Argon. The tunnelling window was formed by sputtered  $\text{SiO}_2$ . Our design of photolithographic mask allows ten different areas of the window, ranging from  $3\mu\text{m} \times 3\mu\text{m}$  to  $100\mu\text{m} \times 100\mu\text{m}$ , all on one sample. The last step was to form the counter electrode. Therefore we thermally evaporated an alloy of indium and lead, which is a well known conventional superconductor. The final junction is shown in Fig.1.

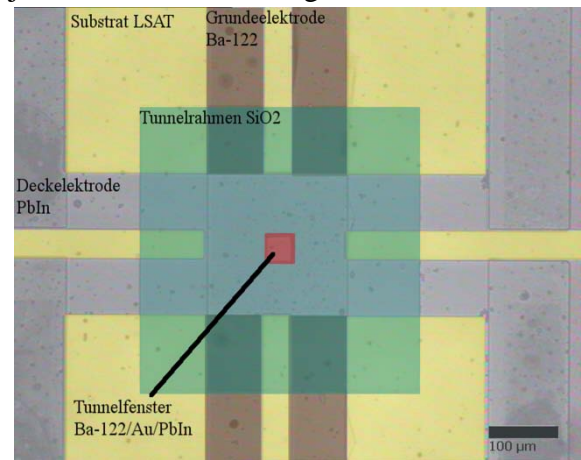


Fig.1 Layout of a tunnel junction.

Prior to the measurements of the tunnel itself, the electrodes have to be characterised. Therefore the contact pads of Ba-122 electrode were bonded with gold wires and V-I-curves were measured at various temperatures between 4.2K and 18K. By deriving them numerically, the differential resistance can be investigated. As shown in Fig.2 its behaviour changes noticeable with the temperature. At temperatures below 6.5K it's nearly zero (except for a small ohmic back-

ground) until the critical current, at which a jump occurs and then falling back to a constant value of  $70\Omega$ . The curves measured at temperatures between 7K and 10K show a smoother rising at  $I_C$ , but ending in the same high current value as the curves mentioned above. At higher temperatures the curves have a v-shaped current dependence and don't show a critical current anymore. At 18K the normal resistance of about  $150\Omega$  is reached.

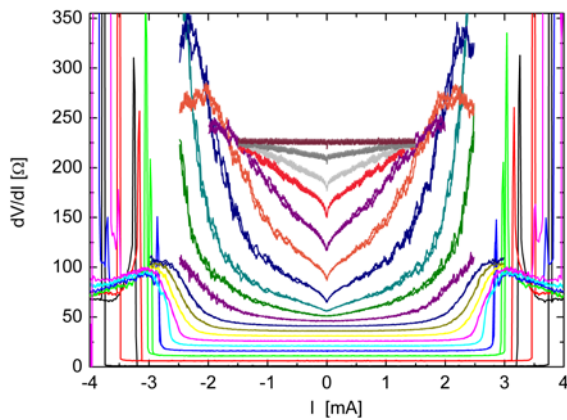


Fig.2 Differential resistance versus current of the Ba-122 base electrode at temperatures between 4.2K and 18K. Each curve is shifted upwards to the previous one by  $5\Omega$ .

The critical current of the Ba-122 can be taken from Fig.2 by taking the current at which the differential resistance arises over the value of the ohmic background.

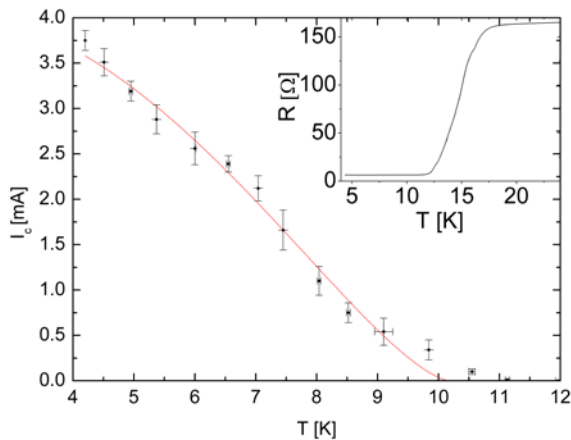


Fig.3 Critical current versus temperature of the Ba-122 base electrode. The solid line corresponds to a fit of the Ginzburg-Landau theory. Inset: Resistance versus temperature of the Ba-122 base electrode.

Within the Ginzburg-Landau theory, the dependence of the critical current is given by [7]

$$I_C(t) = I_C(0)(1 - t^2)^{1.5}(1 + t^2)^{0.5} \quad (1)$$

with  $t=T/T_C$ . As can be seen, our data follows the theoretical prediction for temperatures beneath 9K if a  $T_C$  of 10K is assumed. This causes deviations near  $T_C$ , because the sample's  $T_C$  is about 11K.

When measuring the tunnel using the same procedure as used for the electrodes, we obtain the tunnelling spectra as shown in Fig.4. It can be seen, that the v-shaped dependence of the Ba-122 electrode has a crucial influence on the tunnel spectra, especially at higher temperatures. For the analysis of the tunnel, one has to take account of that fact.

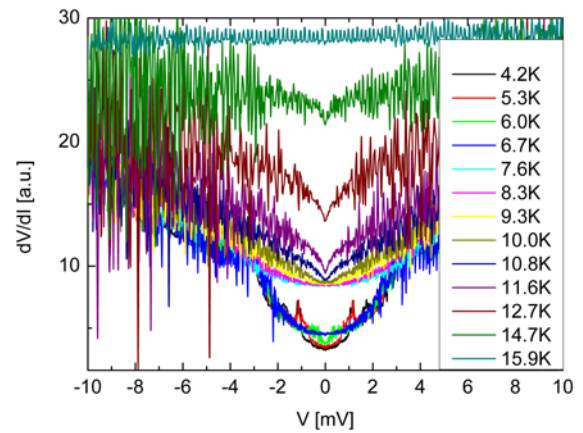


Fig.4 Differential resistance versus voltage of the tunnel junction at various temperatures .

## References

- [1] Y. Kamihara et al.: J. Am. Chem. Soc. 130 (2008) 3296.
- [2] B. Gorshunov et al.: Phys. Rev. B 81 (2010), 060509
- [3] F. Hardy et al.: Phys. Rev. B 81 (2010), 060501
- [4] S. Williams et al.: Phys. Rev. B 80 (2009), 094501
- [5] P. Samuely et al.: Physica C 469 (2009), 507 – 511.
- [6] K. Iida et al.: Applied Physics Letters 95 (2009), 192501.
- [7] W. J. Skocpol et al.: J. Appl. Phys. 45 (1974) 4054

# Thin film hybrid Josephson junctions on iron-based superconductors

S. Schmidt, S. Döring, F. Schmidl, V. Grosse, V. Tympel, K. Iida\*, F. Kurth\*,  
S. Haindl\*, I. Mönch\*, B. Holzapfel\* and P. Seidel

\* IFW Dresden, Institute for Metallic Materials Dresden, Helmholtzstr. 20, 01069 Dresden, Germany

Examining the superconducting properties of the iron-based pnictides (discovered in 2008 [1]) experimentally allows to investigate their superconducting nature. The utilization of Josephson junctions is an effective tool to measure critical currents, their microwave- and magnetic field dependencies and their energy gap(s). Additionally, the quasi-particle density of states and the symmetry of the order parameter are accessible quantitatively.

An estimation of their suitability for applications and devices can be derived from those results. Comparing the values and dependencies with theoretical models can help to understand the superconducting band structure in the pnictides.

In contrast to many groups working on tunnelling junctions utilizing point contact Andreev reflection techniques, we concentrated on the preparation of hybrid Josephson junctions (JJ) consisting of epitaxially grown  $\text{BaFe}_{1.8}\text{Co}_{0.2}\text{As}_2$  thin films (Ba-122) as base electrode, normal conducting gold as barrier material and an alloy of lead and indium as counter electrode. This was the first attempt of manufacturing hybrid JJ in thin film technology worldwide.

A new design of a photolithographic mask system was developed, allowing the electrical measurement (i.e.  $I_C$  and  $T_C$ ) of both the electrodes and the junction structure in 4-point-geometry. The mask design intends to use ten different planar JJ areas (ranging from  $3 \times 3 \mu\text{m}^2$  to  $100 \times 100 \mu\text{m}^2$ ) and five edge contact JJ (with a width of  $3 \mu\text{m}$  to  $20 \mu\text{m}$  and a height according to the base electrode's layer thickness). Cross-sections of both junctions are depicted in Fig.1.

The Co-doped Ba-122 thin films were prepared by a standard pulsed laser deposition technique at IFW Dresden. The deposition temperature of the investigated sample was  $750^\circ\text{C}$ . Details on the film preparation can be found in Ref. [2].

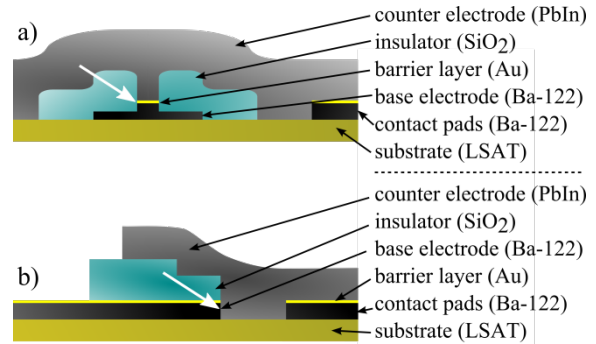


**Fig. 1:** Schematic cross-sections of the (a) planar JJ and the (b) edge junction. The actual junction area is marked with a white arrow.

Exhibiting a roughness of less than 1 nm (rms value), the pnictide layer surface is suitable for a complete coverage with a gold layer of different thicknesses between 5 and 10 nm. This future barrier material deposition process did not change the rms roughness significantly. Additionally, the gold cover prevents contamination during future photoresist processes. The base electrode geometry is patterned via ion beam etching (IBE, 500 eV beam voltage,  $10^{-3} \text{ A/cm}^2$  ion beam density). After removing the Au shortcut via IBE, the junction area is confined by sputtered  $\text{SiO}_2$  (50 W rf-power) of 100 nm thickness (marked with a white arrow in Fig.1a). The counter electrode is formed by a thermally evaporated alloy of lead and indium ( $T_C=7 \text{ K}$ ) with a thickness of 150 nm.

The results we present here were measured in 4-contact-geometry with a gold barrier thickness of 5 nm and a junction area of  $30 \times 30 \mu\text{m}^2$ .

The structuring process caused a slight shift of the transition temperature behaviour of the Ba-122 layer from  $T_{C,50}=15.7 \text{ K}$  prior to  $T_{C,50}=14.4 \text{ K}$  after the structuring (see Fig.2). This may be caused by proximity effects due to the gold layer on its surface. Additionally, both measurements differ methodically, i.e. the first one examined the



whole pnictide layer, whereas in the second one the current is confined in the electrodes.

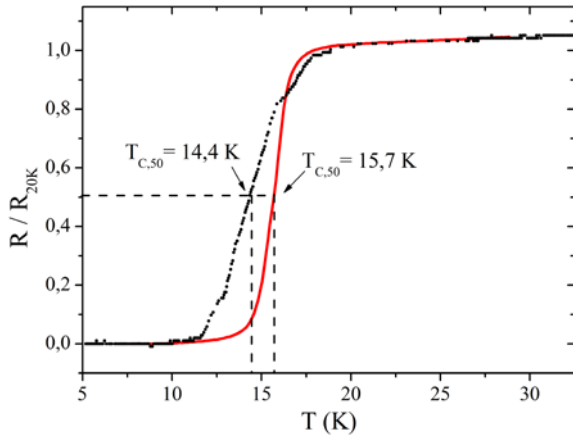


**Fig. 2:** R-T characteristics of the pnictide electrode prior (solid line) and after (black dots) the patterning processes.

Examining the hysteretic I-V characteristics, which can be described using the resistively and capacitively shunted junction (RCSJ) model, we found a critical current,  $I_C$ , of 90  $\mu\text{A}$  with an underlying excess current,  $I_{\text{ex}}$ , of 273  $\mu\text{A}$  (see Fig.3). The characteristic voltage,  $I_C R_N$ , calculates to  $(4.2 \pm 0.3) \mu\text{V}$ . Considering the junction area of 900  $\mu\text{m}^2$  one can derive a critical current density,  $J_C$ , of 23.4  $\text{A}/\text{cm}^2$  and a sheet resistance,  $\rho_N$ , of 5100  $\Omega/\text{cm}^2$ .

Under microwave irradiation Shapiro steps were observed (see Fig.4). Using a frequency of 12 GHz, the microwave power dependence of the Shapiro step heights was examined (see Fig.5) [3].

To model the power dependence of the zeroth step, a RCSJ approach is applied like in Ref. [4].

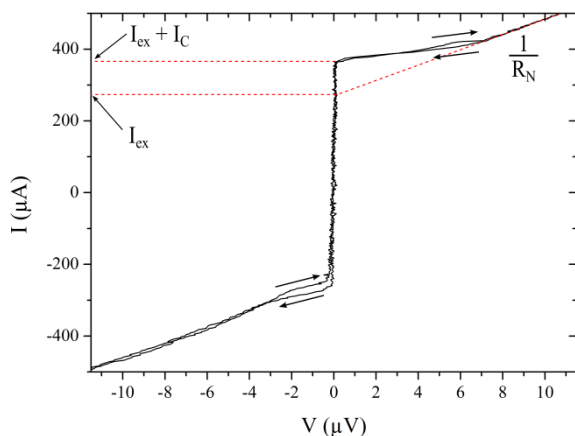


**Fig. 3:** I-V characteristics of the Josephson junction, measured bidirectional at 4.2 K in current bias mode.

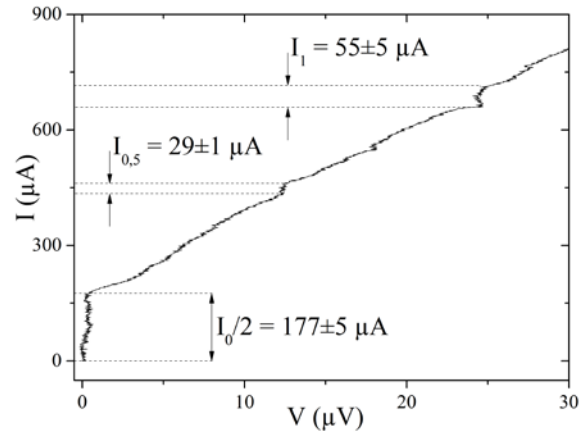


**Fig. 4:** I-V characteristics under microwave irradiation with a frequency of 12 GHz. The heights for half the zeroth, the first and the subharmonic Shapiro steps are denoted.

The critical current is not completely suppressed even at high microwave amplitudes, which justifies the introduction of an excess current. The best agreement with the experimental data delivers the simulation with an exponentially decaying  $I_{\text{ex}}$  and a McCumber parameter  $\beta_C$  of 2.5.

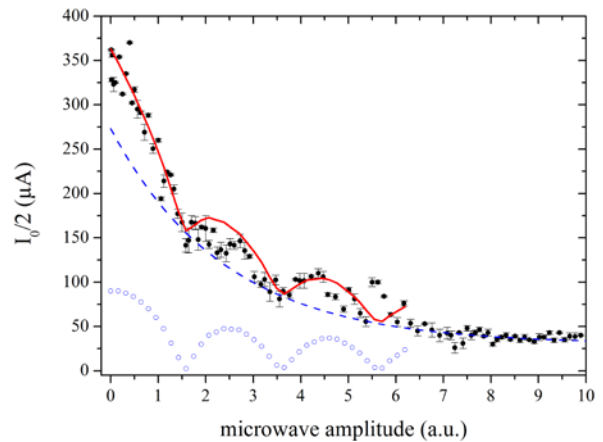


**Fig. 5:** Critical current versus microwave voltage at 12 GHz. The solid line denotes a Bessel simulation consisting of an exponential decay (dashed line) and the Bessel behaviour for the zeroth step (circles).

- [1] Y. Kamihara, T. Watanabe, M. Hirano, H. Hosono, *J. Am. Chem. Soc.* **130** (2008) 3296
- [2] K. Iida, J. Hänisch, T. Thersleff, F. Kurth, M. Kidszun, S. Haindl, R. Huehne, L. Schultz, B. Holzapfel, *Phys. Rev. B.* **81** (2010) 100507
- [3] S. Schmidt, S. Döring, F. Schmidl, V. Grosse, P. Seidel, K. Iida, F. Kurth, S. haindl, I. Mönch, B. Holzapfel, *Appl. Phys. Lett.* **97** (2010) 172504
- [4] P. Seidel, M. Siegel, E. Heinz, *Physica C* **180** (1991) 284



# Ion Beam Irradiation of Nanostructures: 3D Monte Carlo Simulations

C. Borschel and C. Ronning

When doing ion beam irradiation experiments, it is useful and often necessary to accompany the experiments by computer simulations: from these simulations of the ion beam irradiation, the spatial distribution of the implanted ions as well as the distribution of ion beam induced defects can be obtained. Frequently, Monte Carlo codes are used to perform these simulations, with the well-known SRIM code [1] being one of the most popular. However, most of these codes can only simulate ion beam irradiation of flat targets (bulk or homogeneous layers), but they cannot accurately represent nanostructures. When the size of the irradiated structures is comparable to the ion range (or the dimension of the damage cascade) new effects occur compared to bulk. Thus, the correct nanostructure geometry must be taken into account for accurate simulations. We have developed a new Monte Carlo code called *iradina* (ion range and damage in nanostructures), which works similar to SRIM but allows arbitrary 3D target definitions.

## Program description

The target in the program consists of a rectangular box, which is subdivided into many equal-sized rectangular cells. Each cell contains a material or vacuum, which allows a representation of arbitrarily shaped 3D objects. Each material consists of any number of different elements with specified stoichiometry. Furthermore, each cell has a number of counters to record the implanted ions and the produced ion beam damage (vacancies, interstitials ...).

The ion beam irradiation is simulated by letting a large number of ions ( $10^4$  to  $10^6$ ) impinge on the target and calculating the

path of each ion through the target by means of a Monte Carlo code: each ion is assumed to travel through the material in small steps. In each step, the ion suffers one collision with one target atom (“binary collision approximation”) with a randomly selected impact parameter. The scattering angle and energy transfer to the target atom are calculated using the ZBL universal potential [1]. The flight length between subsequent collisions is randomly selected according to a Poisson distribution. Along the flight length, the ion energy is reduced by the electronic energy loss, which is assumed to be continuous. The ions path is followed through the target until it has lost all energy or leaves the simulation volume. The target is assumed to be amorphous (“random phase approximation”), which is a useful approach, as long as the ion beam is not aligned with a low-index crystal orientation.

If the energy transfer to a target atom exceeds its’ displacement energy, the target atoms becomes a moving projectile itself and is followed through the target like the ion. Detailed descriptions and discussion of such transport algorithms are found in [1,2]. In comparison to SRIM [1], *iradina* is about two orders of magnitude faster, because instead of calculating the scattering integral, it uses a fast database method adapted from corteo [2]. Nevertheless, since *iradina* works similar to SRIM, the simulation results for bulk targets should be comparable. This can serve as an initial test of *iradina*. A comparison of the distribution of implanted ions is shown in Fig. 1. The results from *iradina* and SRIM are in good agreement, proving basic functionality of *iradina*.

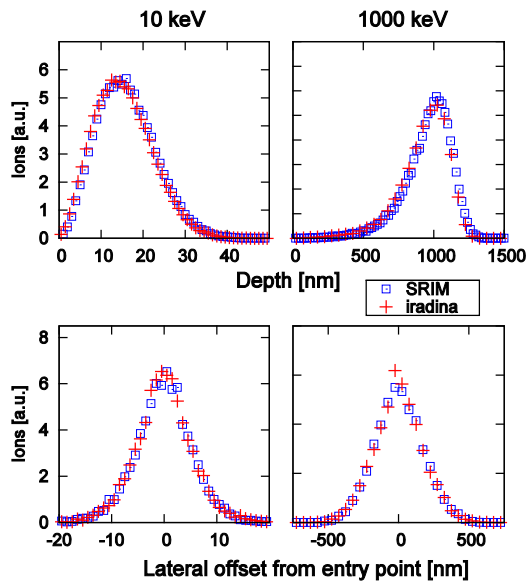


Figure 1: Depth and lateral distribution of implanted Ar ions simulated with SRIM and iradina for ion energies of 10 and 1000 keV.

### Application: nanowire doping

Semiconductor nanowires (NW) of different materials are studied at the IFK. Ion beam implantation is necessary for doping such NW, because the growth mechanism typically inhibits doping during growth. When using the conventional bulk simulation codes to obtain the doping profiles, the results will overestimate the real concentration of implanted ions: since the NW size is comparable to the ion range, a significant fraction of ions hitting the wire leave it at the side and is not incorporated. This effect is illustrated in Figure 2: A box-like concentration profile simulated for bulk targets is shown in (a). The same energies and fluencies were used to simulate the implantation into a NW with *iradina*. Only a thin disk of the NW needs to be simulated as periodic boundary conditions (PBC) can be applied along the NW axis (c). The resulting concentration profile is shown in Figure 2(b) and (d). Comparing (a) and (b) shows that using bulk simulations to calculate implantation into nanowires will lead to lower and inhomogeneous concentration profiles.

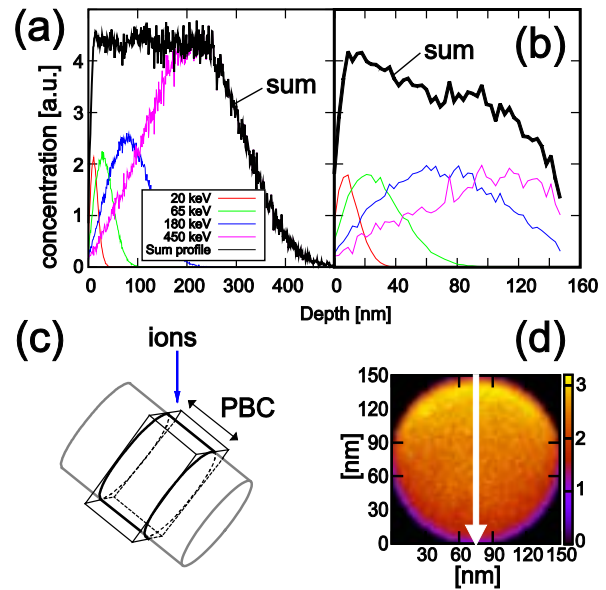


Figure 2: (a) Box-like implantation profile simulated for a bulk target. (b) Iradina simulation for the same energies and fluencies for implantation into a NW. (c) schematic illustration of the simulation. (d) simulated 2d-concentration of implanted ions in the NW. Arrow shows line of profile from (b).

This effect was confirmed experimentally: GaAs NW were implanted with Mn ions. SRIM simulations predicted Mn concentration of 5% for the used parameters, while *iradina* simulations predicted 2.5%. Using X-ray spectroscopy, 2-3% Mn were observed in the implanted nanowires.

### Conclusion

When simulating ion beam irradiation of objects with sizes comparable to the ion range, it is necessary to take into account the correct geometry of the object. Conventional bulk simulators can lead to inaccurate results, as shown for doping of nanowires. In contrast, the new Monte Carlo code *iradina* correctly predicts doping concentrations.

### References

1. J.F. Ziegler, J.P. Biersack and U. Littmark, *The Stopping and Range of Ions in Solids*, Pergamon, New York, 1985
2. F. Schiettekatte, Nucl. Instr. Meth. B 266 (2008), 1880; see also: [www.lps.umontreal.ca/~schiette/index.php?n=Rcherche.Corteo](http://www.lps.umontreal.ca/~schiette/index.php?n=Rcherche.Corteo)

## FIB/SEM Dual Beam System - FEI NanoLab Helios 600i

S. Milz, C. Borschel, C. Ronning

At the end of 2010, a new focused ion beam system (FIB) from FEI was installed in the first floor of the red house (Fig. 1). This dual beam device is equipped with a field effect cathode for the electron beam and a gallium source for the ion beam. Both beams can be accelerated to 0.5-30kV. The electron beam is mainly used for imaging (Fig. 2) - with a maximal resolution of less than one nanometer. The ion beam allows high spatial resolution sputtering of sample surface atoms. Therefore, surface modifications like cutting, milling or polishing on the nanometer scale (down to about 5nm) are possible (Fig. 3).



Fig. 1: Photograph of the focused ion beam system (FIB) FEI NanoLab Helios 600i.

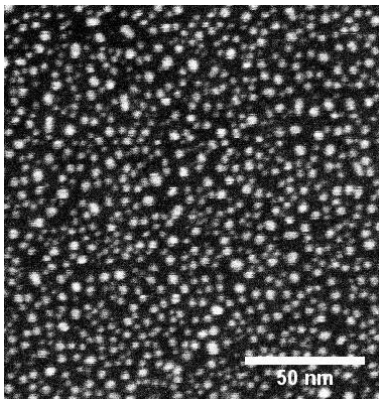


Fig. 2: High resolution transmission image of a test sample. The resolution was calculated to be 0.8nm.

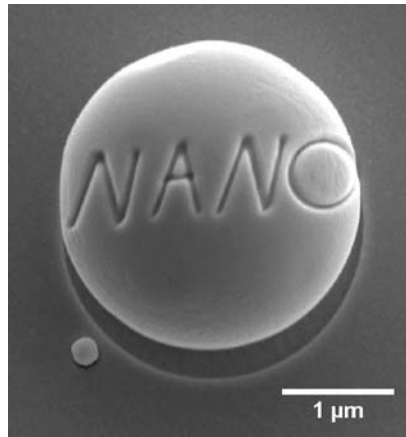


Fig. 3 SEM image of a “nano”-structured gold droplet.

There are several detectors available for imaging: An Everhart Thornley Detector (ETD), a Through Lens Detector (TLD) and an In-Chamber Electron Detector (ICE). They can be used to detect secondary/backscattered electrons with both beams. The ICE detector is additionally capable of detecting secondary ions generated by the ion beam hitting the sample. In addition, another detector for Scanning Transmission Electron Microscopy (STEM, Fig. 5) is installed at the device allowing high resolution images of thin samples (especially TEM lamellas) in transmission mode. The STEM detector is divided in various sectors (see Fig. 4): A spot in the middle for bright field images (BF), a ring for dark field images (DF) and an array of 12 segments used for high angle annular dark field images (HAADF). The three modes can be used to

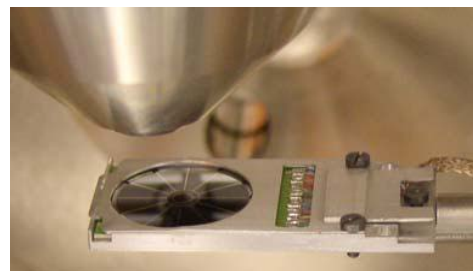


Fig. 4: Photograph of the STEM detector beneath the electron column (without a sample in between).

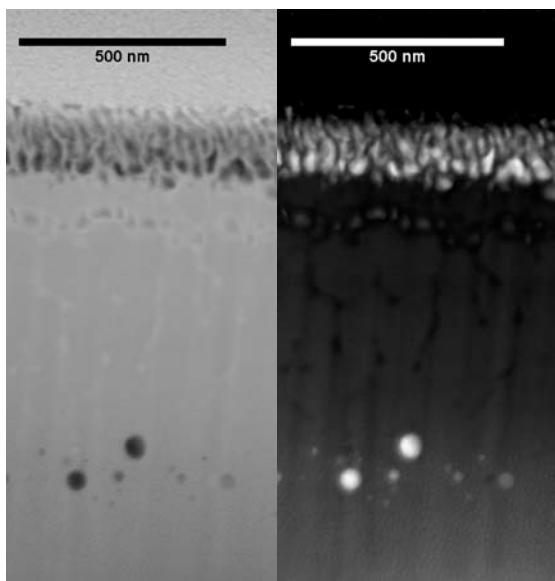


Fig. 5: STEM images of a porous Ge layer (top) and a buried layer of clusters (bottom). Left: bright field image (BF). Right: high angle annular dark field image (HAADF).

optimize material or lattice contrast (Fig. 5). A CCD-camera with IR light is used to follow the movement of the sample and check that it doesn't collide with any equipment.

Four gas injection systems (GIS) are available at the FIB. They evaporate a special source material, typically some organic compound including the desired material. The vapour is guided through a small needle to the sample surface. The ion beam cracks the compound; the heavier parts are deposited on the surface, the lighter (organic) parts are pumped away. The GISs allow the deposition of platinum, gold and SiO<sub>2</sub> with structure sizes in the order of the

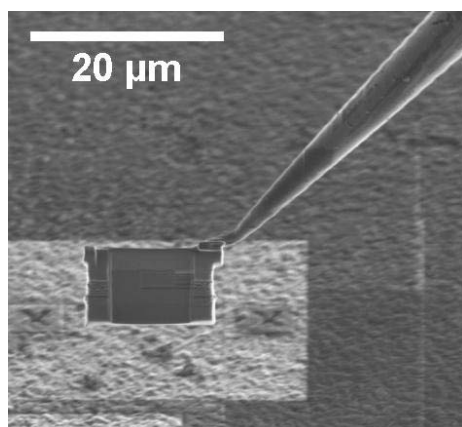


Fig. 6: Ion beam image of the micromanipulator needle lifting out a TEM lamella.

ion beam diameter (some 10nm). Apart from that, XeF<sub>2</sub> can be used to increase the sputtering yield through reactive ion etching.

For easy and quick sample changing, a load-lock chamber was installed to the system (Fig. 1, on the right). It allows sample changing in less than one minute.

Imaging and structuring of highly insulating samples usually suffer from charging effects. To avoid this, a charge neutralizer (an electron gun) can be used in combination with the positive ion beam. When the charge neutralizer is configured correctly, the ion beam can image and modify the surface without any charging effects.

A micromanipulator (Omniprobe) with a small tungsten needle (Fig. 6) can be used for moving nanometer sized objects along the sample. Therefore, the Pt deposition is used to "glue" the object to the micromanipulator needle and the ion beam is used to cut them apart. This is particularly useful for TEM lamella preparation. Therefore, a small lamella (typically 15x5x2µm<sup>3</sup>) is cut out of the sample using the ion beam. Then the micromanipulator needle is glued to the lamella by platinum deposition. After that, the last juncture between the lamella and the sample is sputtered away. The lamella will then be moved to a TEM grid, attached to it and separated from the micromanipulator needle. After a final thinning step (down to less than 100nm) the TEM lamella is ready for TEM studies.

In summary, it can be stated that the new focused ion beam system from FEI is the perfect tool for fast TEM lamella preparation, high resolution SEM studies in backscatter and transmission geometry, in-situ observation of ion beam / nanostructure interactions, nanostructuring of surfaces and electrical contacting on the nanometer scale.

# Design and characterization of ZnO nanowire field effect transistors

I. Slowik, R. Niepelt, M. Gnauck, A. Johannes and C. Ronning

## Introduction

Zinc oxide has been recently one of the most promising functional oxide semiconductors, because of its unique properties and potential applications in various fields, e.g. transparent electronics, ultraviolet light emitters, surface acoustic wave devices or piezoelectric actuators [1]. Furthermore ZnO exhibits a high surface sensitivity and the ability to form self-organized nanostructures like nanowires (NW) with a large surface-to-volume-ratio. Thus, NW field effect transistors (FET) provide a favourable basis to build and study sensing devices like UV and gas sensors.

## Experimental

Zinc oxide nanowires have been synthesized from ZnO powder (99.99% purity) on silicon substrates in a vapor-liquid-solid (VLS) growth process [2].

Subsequently, NW were transferred to another silicon substrate (p-type, 1-20  $\Omega\text{cm}$ ) via imprint for preferably parallel alignment with respect to the substrates' surface. Photolithography and metal film deposition by electron beam evaporation (10 nm Ti + 50-220 nm Au) were then performed to define a pattern of source (S) and drain (D) contacts (Fig. 1). Ultrasonic wedge bonding of gold wires was utilized to connect these

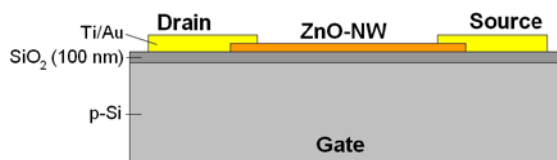


Fig.1: Cross section view of FET sensory device. On top of the oxide layer the nanowire forms a conducting channel between S and D contact of which conductivity can be controlled by the back gate. The oxide layer is about 100 nm thick.

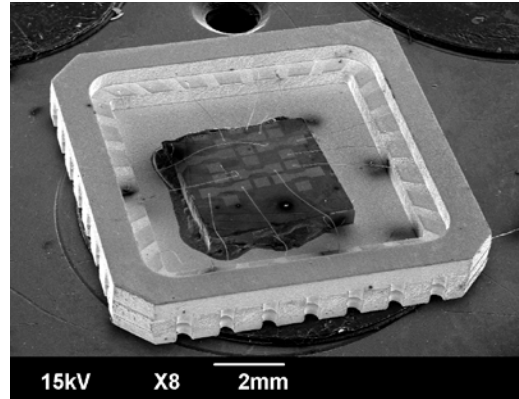


Fig. 2: SEM picture of a substrate with several ZnO-NW-FET structures on top. The sample is glued with conducting silver paste on a commercial sample holder chip which can be mounted to a chip carrier for convenient macroscopic contacting. Bonding wires connect some chosen contacts to the chip.

contacts with a commercial sample holder chip (shown in Fig. 2). The electrical properties were recorded with a Source-Measure Unit (SMU) Keithley Model 237 and a Digital Sourcemeter Keithley 2420 3A under different ambient conditions.

## Results and discussion

As the experimental approach involves only little control about geometrical parameters of single NW, their diameter varies largely between about 100 and 230 nm. Furthermore, the random positioning causes a fluctuating number of contacted NW for different SD-pairs. Thus, comparative investigations always correspond to a fixed contact pair. However, also characteristic  $I_{SD}-V_G$ -measurements of one FET turned out to be problematic as a strong dependence on measurement conditions was observed. Therefore, these effects were studied first. Despite annealing procedure all contacts showed either (almost) rectifying or (almost) symmetric but not linear  $I-V$  characteristics. This observation is consistent with



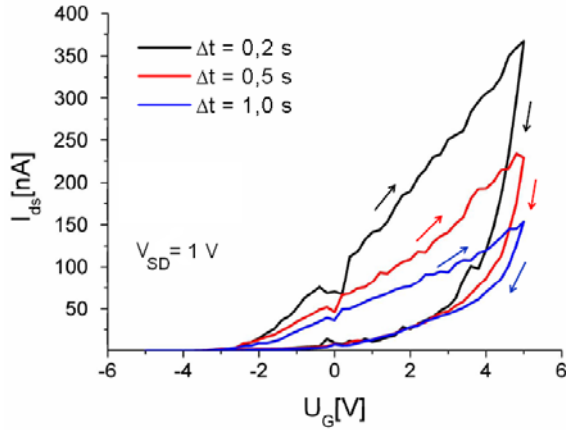
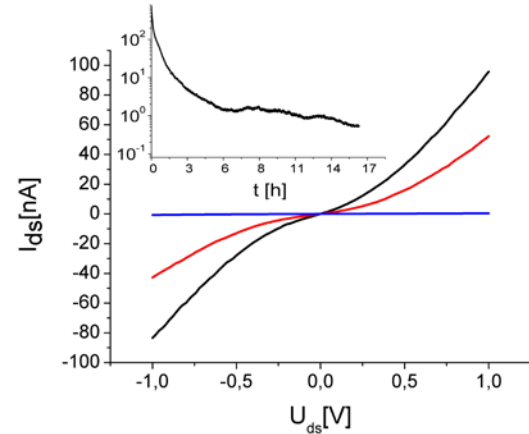


Fig. 3: The longer the delay time  $\Delta t$  is set the more source-drain current at a constant SD voltage decreases. The arrows depict the direction of gate voltage variation. The measurements were carried out in the dark at RT and normal air pressure.

the formation of Schottky contacts, which may have more or less pronounced barrier heights on both sides of the metal semiconductor metal (MSM) structure.

Figure 3 shows a typical characteristic of SD-current as function of the gate voltage  $V_G$  for different times between two measurements (delay time  $\Delta t$ ). All curves show a hysteresis-like characteristics where for each  $\Delta t$  the current is always higher when  $V_G$  is maximized than in the minimizing case. Also, the current decreases when  $\Delta t$  is increased. This effect is associated with dynamic adsorption and desorption processes on the NW surface, which are mainly ascribed to oxygen in the surrounding atmosphere. When oxygen molecules approach the polar ZnO surface they get adsorbed and trap free electrons from the intrinsic n-type semiconductor which creates a depletion layer near the surface. Due to the large surface-to-volume-ratio the NW conductivity decreases significantly [3]. These sorption processes interact with changes in gate voltage but exhibit much larger characteristic time constants: An increasing and positive  $V_G$  reduces the depleted region and the conducting channel expands which increases  $I_{SD}$ . Concurrently, at  $V_G > 0$  more  $O_2$



$I$ - $V$ -characteristics of a NW-FET under different illuminations at  $p = 1$  mbar: room light (black), dark (red) and dark after 24h (blue). The inset shows the decay of  $I_{DS}$  in the dark at  $V_{DS} = 1$  V (PPC effect).

is adsorbed which lowers  $I_{SD}$  the more the smaller the measurement speed is set. When  $V_G > 0$  is reduced again both oxygen adsorption and depletion region extension are superposed and  $I_{SD}$  decreases quickly. At  $V_G < 0$  the increase of depletion region by electrical gate field dominates  $O_2$  desorption and SD-current nearly vanishes. In accordance to these processes an increase of  $I_{SD}$  under vacuum conditions occurs: While pumping the surrounding oxygen away the SD-current raises about more than one order of magnitude. An even larger increase in conductivity was observed when exposing the FET to UV-light with energy close to the ZnO band gap (not shown here) or to room light (Fig.4). In contrast to conventional photoconductivity of semiconductors the current decays very slowly ( $\sim$  tens of hours) after illumination. This so-called persistent photoconductivity (PPC) effect has been reported for many materials and is still to be understood [5].

## References

- [1] J. Park et al., J. Korean Phys. Soc. 55 (2009)
- [2] U. Schröder, Diploma thesis, FSU 2010
- [3] Y. Li et al.; Appl. Phys. Lett. 94 (2009) 023110
- [4] S. Kim et al., J. Elec. Mat. 31 (2002), 868
- [5] P. Lui et al., Appl. Phys. Lett. 94 (2009) 063120

# Lasing in single ZnO nanowires at room temperature

A. Thielmann, S. Geburt, C. Ronning

The prove of lasing in ZnO nanowires (NW) by a previous work [1] provided a new highly localized monochromatic light source. These nanolasers can be of immediate use for the study of the coupling of light to other nanostructures and could potentially resolve the persistent size mismatch between microelectronic and semiconductor optoelectronic devices [2]. The studied NWs are dielectric rods with a high refractive index and two planar end facets, forming a combination of optical waveguide and linear resonator. Stimulated recombination of electron-hole pairs in the crystal material acts as gain mechanism for resonant modes.

## Experimental

ZnO nanowires have been synthesized in a horizontal tube furnace via the vapour-liquid-solid mechanism. The process results in dense ensembles of unordered NWs with diameters from 100 to 200 nm and lengths up to 50  $\mu\text{m}$ . In order to enable the observation of single NWs a clean Si substrate is pressed on top of an as-grown ensemble. Few of the wires will then break from their original underground and adhere to the clean substrate. Fig. 1a) shows a substrate with some NWs. The laser spot for excitation is visible as diffraction pattern of bright concentric rings. Its diameter has been widened to the length of the observed NW by means of a defocusing lens in the laser beam path in order to achieve homogeneous pumping of the whole wire. Partial excitation of a NW usually destroys it before the lasing regime is reached. The samples have been excited with 7 ns pulses of a Nd:YAG laser at 355 nm and a pulse repetition rate of 200 Hz.

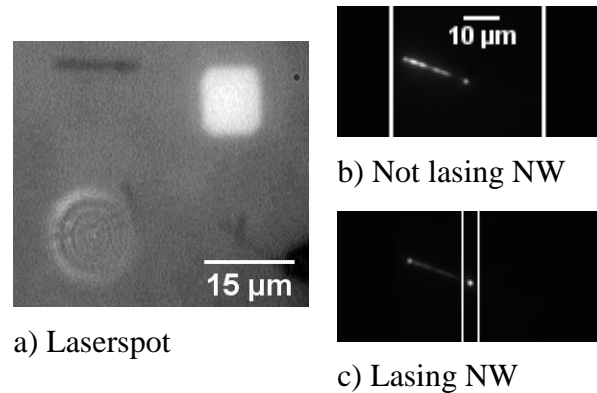


**Figure 1:** a) Picture of widened laserspot for excitation, a 10  $\mu\text{m}$  gold marker square and some nanowires. b) Luminescence of a NW in the ASE regime; white lines indicate the monochromator entrance slit opened to 3 mm for imaging. c) Luminescence of a lasing NW; white lines indicate the slit closed to 50  $\mu\text{m}$  for spectral recording allowing high spatial resolution.

The pulse intensity has been regulated by neutral density filters and by reduction of the Pockels cell voltage in the Nd:YAG laser. The white square in the upper right of Fig. 1a) forms part of a coordinate system of gold markers which has been applied to the substrate by photolithography and e-beam evaporation before the transfer of the NWs. These structures of known size supply a calibration scale for the microscope images and enable relocation of NWs in the scanning electron microscope. Fig. 1b) and 1c) show images of the same NW at different excitation densities, recorded with the spectrograph's CCD detector. For that purpose, the entrance slit (indicated by vertical white lines) has been widened to 3 mm. By aid of a tiltable mirror it is possible to shift a particular part of the NW's image into the center of the entrance slit. For the recording of spectra the slit is closed to 50  $\mu\text{m}$ ; thus, measuring mostly the luminescence originating from the part centered in the slit.



## Results and discussion

Spectra from power dependent measurements on a single ZnO NW are shown in Fig. 2a). At excitation with  $0.06 \text{ MW/cm}^2$ , the intensity of the near band edge emission centered around  $378 \text{ nm}$  is already surpassed by the peak of amplified spontaneous emission (ASE) at  $387 \text{ nm}$ . The intensity ratio of these two peaks varies along the NW. When only a NW end facet is observed by closing the monochromator's entrance slit around its image, the ASE peak is more intensive; whereas, observation of the midpoint between the ends yields mainly the usual near band edge PL. At about  $0.2 \text{ MW/cm}^2$  sharp peaks appear that dominate the whole luminescence spectrum when proceeding to even higher excitation powers. These lines are interpreted as resonator modes from the lasing nanowire. The wavelength separation of adjacent modes at a fixed wavelength has been measured for four lasing nanowires of different lengths. Comparison with SEM measurements of the nanowires shows a clear dependence of the mode spacing on the nanowire length  $L$  that is in agreement with the  $\sim 1/L$  behaviour, which is expected for a Fabry-Pérot resonator. Figure 2b) plots the integrated PL intensity of only the mode structure as a function of the excitation intensity. Three different regimes are clearly distinguishable: at lowest excitation intensities, spontaneous emission is predominant showing a linear dependence on excitation power. Here, luminescence is homogeneously distributed along the whole wire (see Fig. 1b). Above excitation with approximately  $0.1 \text{ MW/cm}^2$  ASE dominates the PL signal, now showing a superlinear behaviour. At even higher pumping the system returns to a linear dependency indicative of laser action in the observed NW. At this point, the

luminescence originates mainly from the NW's end facets (see Fig. 1c).

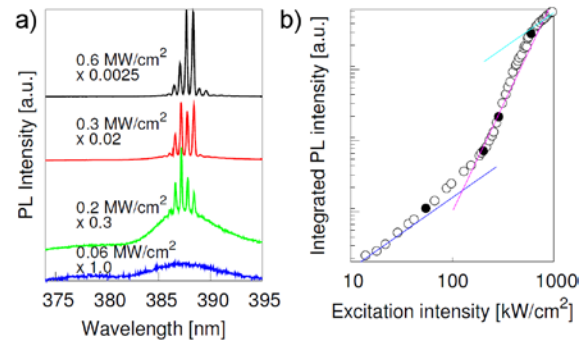


**Figure 2:** a) PL spectra of a single ZnO NW of  $17 \mu\text{m}$  length at different excitation intensities. b) Power dependency of the same NW's PL signal (blue lines: linear dependency, red line: cubic dependency). Black points correspond to spectra shown on the left.

## Conclusion and outlook

Power dependent  $\mu$ -PL measurements at RT proved lasing action in single ZnO nanowires. The observed dependence of the longitudinal mode spacing on NW length is in agreement with the behaviour expected of a Fabry-Pérot resonator. Future measurements will intend to observe lasing in CdS, CdSe and GaAs NWs. A “Head-on” setup for collection of the luminescence light in the emission direction of a single NW laser will be realized, allowing angle dependent measurements of a NW laser's transversal modes and investigation of the excitation polarization's influence on the NW's lasing threshold.

## References

- [1] M.A. Zimmler, F. Capasso, S. Müller, and C. Ronning, *Semiconductor Science and Technology*, vol. 25, 2010, p. 024001.
- [2] C.Z. Ning, *Physica Status Solidi (B)*, vol. 788, Mar. 2010,

# Optical properties of cuprous oxide

Ch. Müller, S. Geburt, A. Laufer\*, B. K. Meyer\*, C. Ronning

\*I. Physikalisches Institut, Justus-Liebig-Universität Gießen

Copper(I) Oxide ( $\text{Cu}_2\text{O}$ , Cuprous Oxide) is a p-type direct semiconductor with a band gap energy of  $\approx 2,1$  eV and a high exciton binding energy of 150 meV [1]. Some interesting characteristics like a good absorption coefficient for light above the gap, good mobilities of the majority carriers and the diffusion length of the minority carriers of several micrometers make  $\text{Cu}_2\text{O}$  thin films promising candidates especially for solar cells [2]. One of the interesting aspects of  $\text{Cu}_2\text{O}$  is the easy preparation process by simple oxidation. Whereas, thin films can be produced by sputtering or electro-deposition. Beside,  $\text{Cu}_2\text{O}$  is composed of very abundant and non-toxic elements, but the electronic structure is not completely clear and it is difficult to get n-doped  $\text{Cu}_2\text{O}$  up to now, which is attributable to the mechanism of self-compensation [3].

## Experiments and discussion

The synthesis of the  $\text{Cu}_2\text{O}$  films were produced by reactive sputtering at the Justus-Liebig-University in Gießen. A metallic copper target, the sputter gas argon and the reactive gas oxygen at a gas flux of 2,0 sccm were involved to deposit  $\text{Cu}_2\text{O}$  on top of glass substrates [4, 5]. The as-grown films were characterised in UV-VIS for transmission properties and thickness. The thickness was estimated to be between 1,2 and 1,5  $\mu\text{m}$ . Out of this data the absorption coefficient (without considering reflection) was calculated. Only above energies of 2,4 eV  $\text{Cu}_2\text{O}$  absorbs light. This behaviour can be understood, because this is a consequence of the forbidden dipole transition between the two higher valence bands

and the lower conduction band. Above 2,4 eV, dipole transitions between the higher valence band and the second lower conduction band are allowed [3].

The absorption coefficient weighted with energy and an exponent of 2/3, which results out of the direct forbidden gap, was plotted in a tauc-plot. The gap energy of the films could be estimated to  $\approx 2,0$  eV (see Fig. 1).

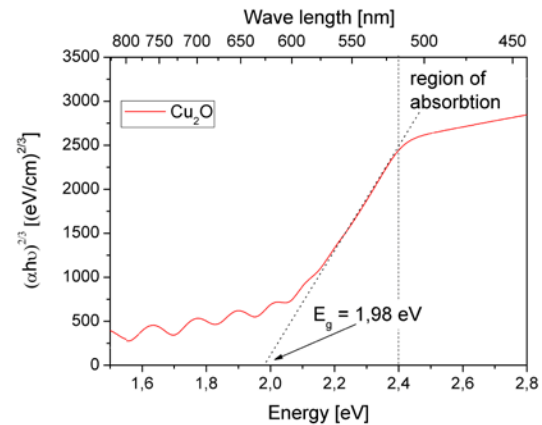


**Fig. 1:** Energy gap of  $E_g = 2,0$  eV estimated by a tauc-plot calculated out of transmission data. Above 2,4 eV  $\text{Cu}_2\text{O}$  starts to absorb light strongly.

For future characterising of ion implanted  $\text{Cu}_2\text{O}$  films, annealing experiments were performed on as-grown films to handle the effect of phase transformation from  $\text{Cu}_2\text{O}$  to  $\text{CuO}$ . Upon heating, different annealing atmospheres like air, argon and pre-vacuum, times of 30 and 60 minutes and temperatures of 400 and 600°C were examined. XRD-measurements showed that annealing in air leads to very strong transformation to  $\text{CuO}$ . Samples threaded in argon atmosphere shows no unwanted  $\text{CuO}$  peak in the XRD spectra and show no difference to the spectra of the as-grown film (see Fig. 2).

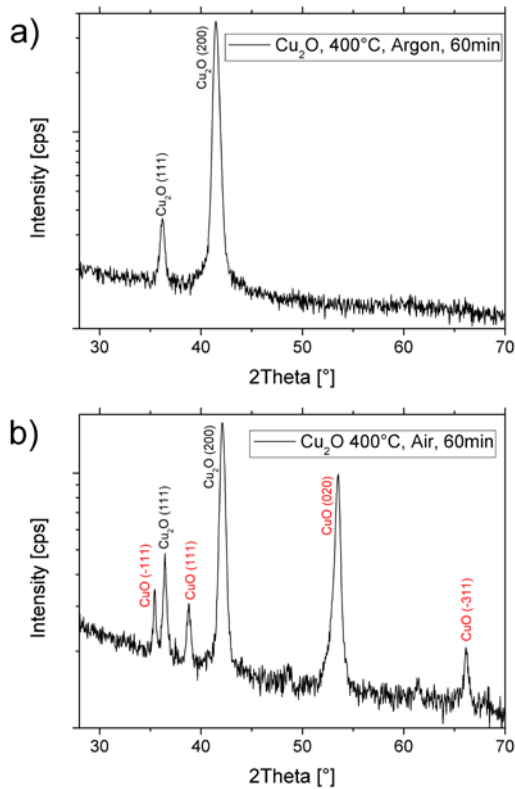


**Fig. 2:** XRD measurements of  $\text{Cu}_2\text{O}$  samples annealed in different atmospheres. Samples annealed in argon at  $400^\circ\text{C}$  for 60 minutes show no unwanted  $\text{CuO}$  peaks (a); whereas, samples treated in

Furthermore, cathodoluminescence (CL) and photoluminescence (PL) characterisation were performed on as-grown  $\text{Cu}_2\text{O}$  films. Unfortunately,  $\text{Cu}_2\text{O}$  films that were processed with a higher quality copper target showed much weaker luminescence intensity. Upon higher excitation density in the CL the  $\text{Cu}_2\text{O}$  films degenerate, because of thermal effects of the electron beam at the excitation spot. So the excitation energy at CL is limited (see Fig. 3). Laser excitation is much more efficient, because its energy is nearly completely absorbed by the material. No degeneration of the  $\text{Cu}_2\text{O}$  could be observed during PL measurements. Three bands could be observed in the luminescence spectra, which originate from different defects. It is suspected that all three bands originate from recombination of bound excitons. The band at  $1,72\text{ eV}$  is caused by double charged oxygen vacancies; the band at  $1,51\text{ eV}$  is produced by

single charged oxygen vacancies, whereas the band at  $1,36\text{ eV}$  results out of copper vacancies, which act as acceptor level and are responsible for the p-type conductivity of  $\text{Cu}_2\text{O}$  [2]. The near band edge luminescence could not be observed, which is a result of either a too high sample temperature or poor  $\text{Cu}_2\text{O}$  film quality.

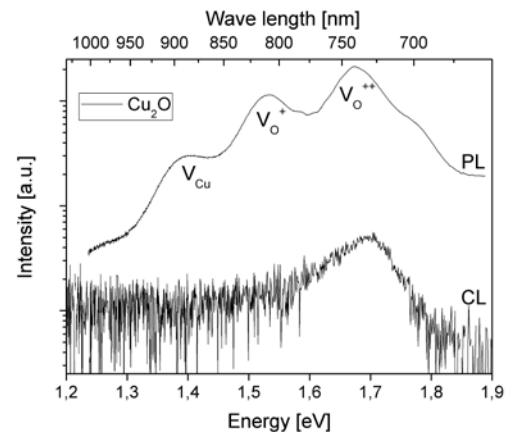


**Fig. 3:** PL measurements have a higher luminescence intensity compared to the CL spectra taken with the same integration time of 100s.

## Conclusion

The band gap energy of sputtered  $\text{Cu}_2\text{O}$  thin films could be determined by transmission measurement to  $2,0\text{ eV}$ . Annealing at argon atmosphere is promising for further characterisation of ion implanted films. Especially PL measurement is a useful instrument to characterise the kind of defects in band gap.

## References

- [1] Liu et al., Semiconductor Science Technology, 20 (2005) 44.
- [2] Solache-Carranco et al., Journal of Luminescence, 129 (2009) 1483.
- [3] F. Biccari, Ph. D. Thesis, University of Rome, 2009
- [4] S. Merita, Ph. D. Thesis, University of Gießen, 2007
- [5] S. Graubner, Ph. D. Thesis, University of Gießen, 2010

# Exploring the luminescence of nanostructures and solar cells

S. Geburt, A. Thielmann, C. Ronning

Photoluminescence (PL) is a powerful technique for the non-destructive investigation of semiconductors, by which the sample is excited by photons with an energy above the material's band gap. The radiative recombination of the excited carriers leads to the emission of luminescence light, which contains e.g. information about the band edge properties, dopand or defect concentrations, binding energies of states and impurity lifetimes. These measurements can now be performed with a new micro- and macro-photoluminescence setup, which was established at the IFK. A sketch of the system is shown in Fig. 1.

Two lasers are available for the excitation of the samples: A continuous-wave HeCd laser emitting at 325 nm with an average power of 33 mW allowing investigations at steady state conditions as well as a pulsed Nd:YAG laser emitting at 266, 355 and 532 nm can be used as excitation source for high excitation and time resolved measurements. The 7 ns pulses with up to 2.5 mJ pulse energy at 200 Hz repetition rate make the computer controlled laser system a valuable and flexible tool. All lasers are guided to a wavelength separator (Pellin-Broca-prism) to suppress unwanted laser lines and are delivered in one beam line to the experiments. The laser intensity can be varied by an attenuator (only for Nd:YAG) and a neutral density filter wheel over more than seven orders of magnitude.

Two experiments are available, which can be switched with only small effort: a *macro PL setup* allows the fast investigation of the PL emission properties of samples up to 50 mm in diameter, which can be mounted in a LHe flow cryostat allowing sample temperatures between 3.5 and 475 K. High pre-

cision translation mechanics are used to change the sample position.

The cryostat can be converted with a different sample holder to a micro-cryostat for the *micro PL setup* ( $\mu$ PL): The laser beam is guided through a beam splitter and focused by a microscope objective to reach a spatial resolution of  $\sim 1 \mu\text{m}$  at the focal spot on the sample. Due to the focussing, very high excitation densities (up to several  $\text{MW}/\text{cm}^2$ ) can be reached. Several reflective and refractive microscope objectives with magnifications between 10 to 40x allow the optimum experimental conditions. White light illumination and imaging on a sensitive TV camera makes the system work like a bright field microscope to adjust the laser spot and the position of the sample. The luminescence signals are guided by a mirror to the detection system.

A 500 mm Czerny-Turner monochromator equipped with two entrance ports (micro & macro setup), triple grating turret and fully computer controlled slits and filter wheels is used for the dispersion of the luminescence light. Two grating turrets with low and high resolution gratings, optimized for either UV-VIS or NIR region, are available and can be interchanged quickly. With the low resolution gratings, the system can monitor a spectrum over 350 nm at once, the high resolution gratings provide a resolution up to 0.04 nm (0.1 meV). The dispersed light is detected either by a liquid nitrogen cooled front-illuminated CCD camera sensitive between 200 - 1100 nm or a liquid nitrogen cooled InGaAs array working between 800 - 1700nm. For time resolved measurements, the CCD camera can be changed to an intensified CCD (iCCD) camera (200 - 860 nm), which can be elec-

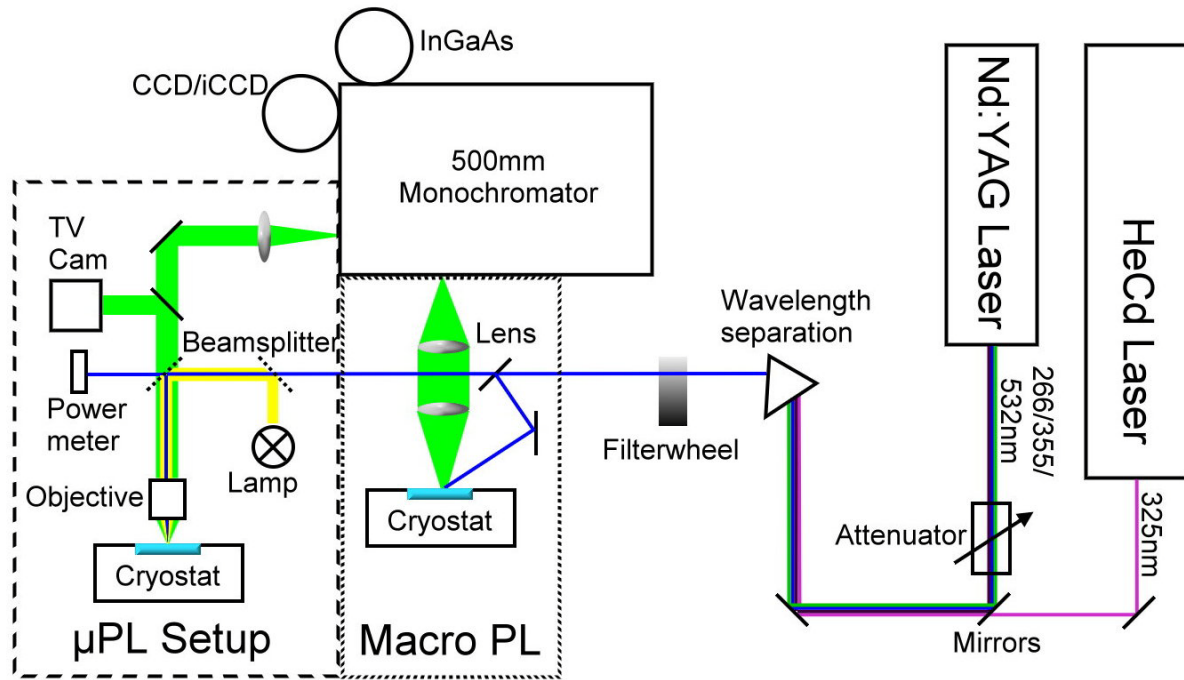


**Fig. 1:** Sketch of the photoluminescence system at the IFK: The laser beam of a cw HeCd (325nm) or the pulsed Nd:YAG (266, 355 & 532nm) are focused in one beamline and wavelength separated by a Pellin-Broca-prism. The intensity of the laser beam can be varied by the attenuator (only Nd:YAG) and the neutral density filter wheel over more than 7 magnitudes of power. For the *macro PL setup*, the beam is guided onto the sample in a LHe flow cryostat (3.5 – 475 K). The emitted PL is collected by a lens system and focussed onto the slit of the 500mm monochromator. The light is detected either by a CCD camera (200-1100nm) or an InGaAs array (800-1700nm). For the *μPL setup*, the laser is guided through a beamsplitter and focussed by a microscope objective onto the sample in the cryostat. White light illumination can be applied to collect an image of the sample with the TV camera and adjust the sample. The luminescence light is collected by the microscope objective and focussed onto the secondary entrance of the monochromator.

tronically gated and allows the temporal resolved recording of spectra with a minimal gate width of 2.7 ns. All detection devices and the monochromator are controlled by an user friendly software, which allows the programming of macro software. Thus, complicated measurement procedures can be simplified to one button.

The setup is completed by a tuneable light source consisting of a high power Xe lamp illuminating a computer controlled monochromator with two gratings optimized for UV and VIS. The emission can be adjusted between 250 to 1000 nm with a band pass between 0.25 to 20 nm. The light is focussed into a light guide and illuminates the sample at the macro setup. The combination of the two systems is used for *photoluminescence excitation spectroscopy* (PLE) experiments, by which the emission intensity

of the sample is monitored as a function of the excitation wavelength. The detected signals lay open the excitation levels or bands of the PL emission.

In first experiments, the very high sensitivity of the photoluminescence system was proved for the investigation of lasing properties of single ZnO and CdS nanowires. Macro PL measurements were used to record the emissions from optical active impurities like the 3d-transitions of  $\text{Co}^{2+}$  in ZnO or intra-4f-transitions from  $\text{Tb}^{3+}$  in ZnS nanowires. The emissions of CIGS solar cells under applied voltage (electroluminescence) could be successfully measured.



# Intense intra-3d-emission from $\text{Co}^{2+}$ doped ZnO nanowires

S. Geburt, F. Riedel, C. Ronning

Semiconductor nanowires offer several fascinating properties which can be used for e.g. waveguides, LEDs or nanolasers [1-3]. Unfortunately, the high excitation densities of  $\sim 300 \text{ kW/cm}^2$  do not allow a realistic integration into optoelectronic devices. An approach to solve this problem is borrowed from conventional laser systems like Nd:YAG lasers: The light emitters are decoupled from the resonator to achieve lower thresholds. This could be transferred to nanowires by implantation with optical active elements like the transition metal Co: the isovalent  $\text{Co}^{2+}$  ion in the ZnO matrix shows an efficient intra-3d-emission at 660 nm (1.88 eV).

## Experimental

ZnO nanowires were synthesized via VLS in the high temperature tube furnace. The nanowire ensembles were implanted with Co with ion energies between 20 to 380 keV to create a homogenous doping between 25 to 200 nm. The ion fluences between  $7.75 \cdot 10^{14}$  to  $1.24 \cdot 10^{17} \text{ cm}^{-2}$  resulting in concentrations from 0.05 to 8 at.%. Annealing was performed at  $700^\circ\text{C}$  for 30min in air, which are suitable conditions for the reduction of ion induced crystal damage and the optical activation of Co.

## Results

Cathodo- (CL) and photoluminescence (PL) measurements were performed to study the emission properties of ensembles and single Co doped nanowires. Fig. 1 shows the PL overview spectra of ZnO nanowire ensembles with different Co concentrations. The ZnO near band edge emission (NBE) arises as a series of sharp peaks between 3.0 and 3.4 eV originating from excitonic recombinations and their phonon replica. A broad

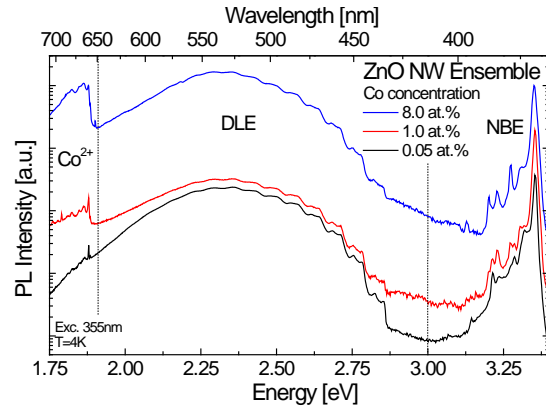


**Fig. 1:** PL overview spectra of Co implanted ZnO nanowires show the intense ZnO NBE as a series of sharp peaks, the defect related DLE as structured emission band which is superimposed with the  $\text{Co}^{2+}$  intra-3d-emission at 1.88 eV (660nm).

and structured band around 2.4 eV appears due to deep level emissions (DLE) from defect states. This band is superimposed by the intra-3d-emission from  $\text{Co}^{2+}$  ions at 1.88 eV [4]. The Co emission intensity increases with concentration. Fig. 2 shows a high resolution spectrum of the  $\text{Co}^{2+}$  luminescence: The direct  ${}^2\text{E}(\text{G}) \rightarrow {}^4\text{A}_2(\text{F})$  transition is detected as a non-symmetric peak at 1.882 eV followed by a sideband at lower energies in which several phonons could be identified. It is remarkable that the lately installed PL setup is able to resolve the TA[A] and the TO[A] phonon having an energy spacing of only 0.63 meV. The intensity of the phonon side band increases

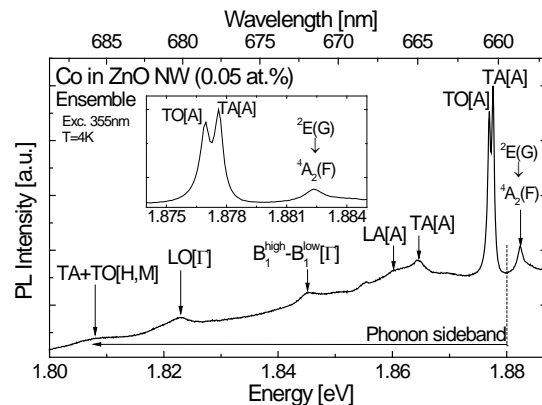


**Fig. 2:** The high resolution spectra of the  $\text{Co}^{2+}$  emission resolves the direct transition as well as several phonon replica in a sideband at the lower energies. Inset: The TA[A] and TO[A] phonon, having an energetic spacing of only 0.63 meV, can be resolved.

with Co content due to a higher fraction of disordered crystal around the ions [5]. The intensity of the Co luminescence is plotted as a function of temperature in Fig. 3. The luminescence is most intense for low temperatures, but the intensity loss is small up to 50K. At higher temperatures, the direct transition as well as the phonon peaks disappear and only a broad band is detected up to room temperature, which shows a shift of lower energies of  $\sim 40$  meV. The intensity loss can be correlated to non-radiative de-excitation mechanisms of the  $\text{Co}^{2+}$  ions, which become more probable at higher temperatures.

CL measurements on single NWs reveal the intense emission from the Co ions, which is more intense compared to the ensemble spectra (e.g. compare spectra of 0.05 at% Co content in Fig.1 and Fig 4.). The explanation is given by the sample structure: The ensemble sample consists of the implanted ZnO nanowires and nanostructures below the nanowires, which were not implanted, but contribute to the emission of the host material. Therefore, a strong  $\text{Co}^{2+}$  luminescence was observed even for low doping concentrations (see Fig. 4).

Measurements as a function of excitation density performed on a single NW show a linear intensity increase of the Co and the

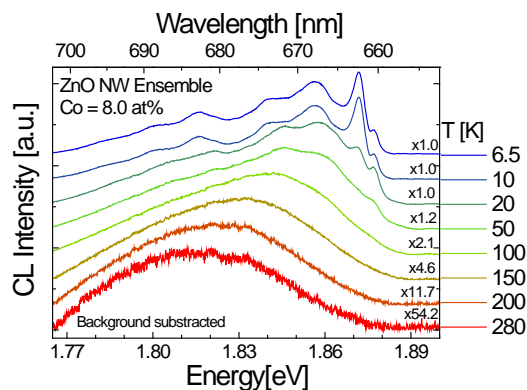


**Fig. 3:** CL measurements of a ZnO NW ensemble as a function of temperature. The  $\text{Co}^{2+}$  emission decreases only slightly up to 100 K, but the sharp peaks of the direct transition and the phonons dis-

appear in the examined range. The ZnO NBE shows a sublinear increase first, followed by a linear rise above  $\sim 500$   $\text{W}/\text{cm}^2$ .

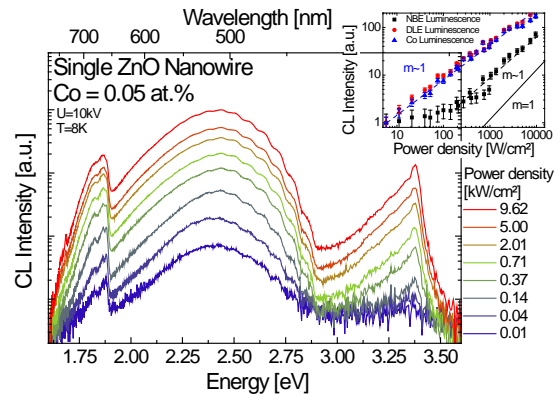


**Fig. 3:** Power dependent CL spectra of single doped ZnO nanowire ( $L=8.3$   $\mu\text{m}$ ,  $\phi \sim 280$  nm,  $\text{Co} = 0.05$  at.%) show the linear increase of the defect and the Co emission intensity with excitation density. The ZnO NBE intensity increases sublinear up to  $\sim 300$   $\text{W}/\text{cm}^2$  and follows a linear trend at higher values.

## Conclusion and Outlook

Co doped ZnO nanowires offer an intense  $\text{Co}^{2+}$  emission from single nanowires, making them a promising candidate for future optoelectronic application.

Further CL and  $\mu\text{PL}$  measurements on single NW will to be performed to become more insights of the luminescence mechanisms and possible effects related to the nanoscale.

## References

- [1] Zimmerler et al., APL. 94, p. 241120 (2009)
- [2] Voss et al., Nanolett. 7(12), p. 3675–3680 (2007)
- [3] Zimmerler et al., APL. 93, p. 051101 (2008)
- [4] Müller et al., Nanotech. 20, p. 135704 (2009)
- [5] S. Müller, PhD thesis, Uni. Göttingen (2009)



# Morphology Changes and Alignment of Semiconductor Nanowires using Ion Beams

S. Spindler, C. Borschel, and C. Ronning

Semiconductor nanowires (NWs) have attained much interest in recent years due to their numerous application possibilities as functional devices as well as interconnecting elements<sup>1</sup>. For several applications it is useful to change the morphology and the orientation of the NWs in a desired way. This is limited by the growth process (e. g. due to epitaxial relations), so post-growth methods are necessary. It was found out, that ion beam irradiation, which is generally used for doping<sup>2</sup>, is also a good method to bend and align NWs after growth<sup>3</sup>. Therefore, a change in morphology and orientation as well as a functionalization of the NWs can be done by the same process.

For gallium arsenide (GaAs) NWs a bending model was established in previous experiments<sup>3</sup>: Irradiation with low ion energies (low penetration depth) leads to a bending away from the ion beam, whereas high ion energies (deep penetration depth) lead to a bending towards the ion beam. The underlying mechanism is the formation of an inhomogeneous defect distribution along the NW cross section, leading to a volume expansion in one part of the NW, which causes a bending momentum<sup>3</sup>. This should be confirmed for zinc oxide (ZnO) NWs.

## Experimental

ZnO NWs ( $\varnothing$  50-100 nm) were grown epitaxial on top of aluminium nitride (AlN) and Al:ZnO (AZO) substrates, respectively. The ZnO NWs were irradiated in two ways: (A) whole samples with a high density of NWs were irradiated with the implanter ROMEO; (B) single NWs were irradiated using a dual-beam focused ion beam (FIB). The FIB only provides Gallium ions ( $\text{Ga}^+$ )

and the energy is optimized to 30 keV (low penetration depth); whereas, every element and a wider energy range is possible at ROMEO, so shallow as well as deep implantation could be investigated. Argon ions ( $\text{Ar}^+$ ) were used at ROMEO in order to analyze the impact of chemical effects, which may occur due to Ga incorporation. The fluence was increased for every implantation step and scanning electron microscopy (SEM) images were taken in between.

Subsequently annealing experiments were carried out, which is necessary to heal out the ion beam induced defects to functionalize the NWs. Furthermore, implantations at high temperatures were made at ROMEO with 20 keV  $\text{Ar}^+$  and  $2 \cdot 10^{16}$  ions/cm<sup>2</sup>.

Transmission electron microscope (TEM) images were made to analyze the impact on crystal structure.

## Results and discussion

Fig. 1 (high energy) and fig. 2 (low energy) show SEM images of  $\text{Ar}^+$  irradiated NWs with increasing fluence. For high energies a bending towards the ion beam occurred. With increasing fluence the NWs get aligned along the ion beam direction, because less ions are implanted with decreasing angle between ion beam and NW.

For low energies a bending away from the ion beam was observed, which increases with increasing fluence and goes into saturation at high fluencies. In fig. 3 the measured curvatures as a function of fluence is shown for a single irradiated NW with 30 keV  $\text{Ga}^+$  (also low penetration depth). Negative values are plotted to indicate a bending downwards.

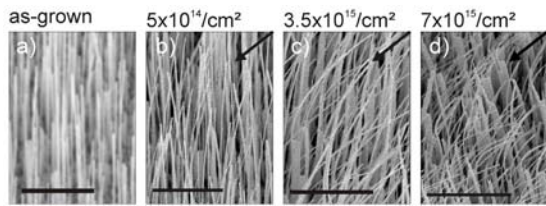


Fig. 1: NWs irradiated with different fluencies of 100 keV Ar<sup>+</sup> (in ions/cm<sup>2</sup>). Arrows denote ion beam direction. Scale bars are 5 μm.

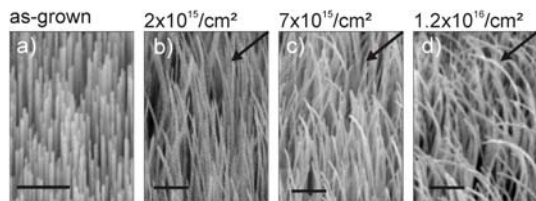


Fig. 2: NWs irradiated with different fluencies of 20 keV Ar<sup>+</sup> (in ions/cm<sup>2</sup>). Arrows denote ion beam direction. Scale bars are 1 μm.

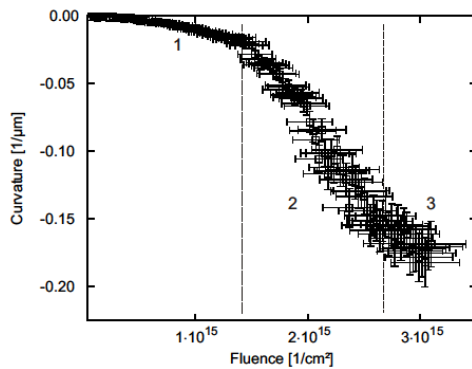


Fig. 3: Curvature as a function of fluence for a single NW irradiated with 30 keV Ga<sup>+</sup> (in ions/cm<sup>2</sup>). Error bars denote inaccuracy of measurements (10%).

First, the curvature increases slowly, because only few ions are implanted (1). With increasing fluence more defects are created and the curvature increases faster (2). With increasing bending the projected ion range increases, too, shifting the defect distribution deeper into the NW. This is amplified by sputtering, which is significant at high fluencies and leads to a thinning of the NW. Therefore, a saturation is observed at high fluencies (3). Another experiments with Ga<sup>+</sup> showed, that for still higher fluencies the tips of the NWs bend back towards the ion beam. This was not observed for Ar<sup>+</sup> irradiated NWs and is therefore attributed to chemical effects.

TEM investigations of Ar<sup>+</sup> irradiated NWs revealed that the NWs are still orientated in c-direction at every point of the NW. The ion induced defects lead to a formation of dislocations, which allows relaxation of the axial stresses making the bending permanent. After annealing dislocations were still present. Therefore, the noble gas ion irradiated NWs showed no change in curvature up to 800 °C. In contrast, a Ga<sup>+</sup> irradiated NW bent back. This is also due to chemical effects: A possible explanation is the formation of different phases with lower density<sup>5</sup>, which would produce tensile stresses at the irradiated side of the NWs.

For high temperature implantations the bending became less at 700 °C and was scarcely observable at 800 °C. This is presumably according to a higher defect mobility, which leads to few dislocations.

### Conclusion and Outlook

The bending model for GaAs NWs could be proofed for ZnO NWs and was analyzed in a more detailed way. The bending is permanent due to the formation of dislocations, which cannot be healed out even at 800 °C. Therefore, the bending of the Ar<sup>+</sup> irradiated NWs was still present after annealing. For Ga<sup>+</sup> irradiated NWs a bending back was observed, which is attributed to chemical effects. In order to prove the assumed explanations, TEM investigations of the FIB irradiated NWs are necessary. Irradiation at high temperatures showed less bending of the NWs. For a controlled bending more experiments have to be carried out with different ion species, ion energies, NW diameters, etc.

### References

1. C. M. Lieber and Z. L. Wang, MRS Bulletin **32**, (2007) 99-108.
2. C. Ronning et al., Mat. Sc. Eng. R **70**, (2010) 30-43
3. C. Borschel et al., Small **5**, (2009) 2576-2580
4. M. Kozlik et al., Annual Report 2008, 14-15
5. J. J. Robbins et al., Journal of Crystal Growth **263**, (2004) 283-290

# Biofunctionalization of ZnO nanowires

U. Schröder, R. Niepelt, J. Sommerfeld, R. Möller\*, B. Rudolph\*, C. Ronning

\* *Institut für Photonische Technologien, Albert-Einstein-Straße 9, 07745 Jena*

We report on the biofunctionalization of ZnO nanowires with organosilanes. The semiconducting nanowires have been covered with fluorescent marked DNA capture molecules. Fluorescence microscopy studies revealed a successful DNA immobilization on the nanowire surface.

## Introduction

During the last decade, there have been several studies concentrating on the development of Si-based nanowire sensors [1]. Si nanowires are CMOS compatible, biocompatible and techniques for the functionalization of Si are well understood. Zinc oxide is not CMOS compatible, but compared to silicon it is stable under oxygen-rich conditions. ZnO is also biocompatible, non-toxic, and easy available. ZnO nanostructures are easy and reliably to produce in a wide manner of different forms and structures [2,3]. The DNA capture molecule immobilization with organosilanes has been successfully shown by Corso and co-workers on planar ZnO surfaces [4], where the biomolecule layer was used to act as an acoustic wave sensor. With the use of ZnO nanowires instead of planar films, the metal oxide itself can be used to build an electrically working biosensor, using the attached DNA capture layer to drive the conductivity properties of the nanowire and detect that way the agglomeration of polar DNA target molecules.

## Experimental

The ZnO nanowires have been grown via VLS-mechanism in a horizontal tube furnace [5] with a growth temperature of

1050 °C. SEM pictures of the as-grown wires reveal a typical spaghetti-like structure with wire diameters around 100 nm and wire lengths up to some tens of  $\mu\text{m}$ . To remove absorbed species from the nanowires and supply a clean and reactive ZnO surface the samples have been oxygen-plasma treated for 30 min at 5 pa oxygen pressure with a plasma energy of 50 W. As this treatment is known to enhance the dissociative adsorption of water on the ZnO surface [6], the samples have been stored in a cabinet dryer at 100 °C for at least 5 min before the silane treatment.

Silanization took place in 10 mM Glycidyoxypropyltrimethoxysilane (GOPS) in a water free toluene solution. The samples have been incubated stirring constantly for at least 6 h at 70 °C. The samples have been rinsed 3 times subsequently with pure toluene for 5 min in each case and then dried with compressed air.

For the biofunctionalization the 5'-amino-modified oligonucleotides were dissolved in 5x PBS buffer (pH 7.4) with a concentration of 10  $\mu\text{M}$ . The DNA solution was pipetted onto the nanowire samples and incubated over night under wet conditions. Afterwards the samples were rinsed for 10 minutes in 15 mM tris-HCl-buffer (pH 8) to get rid of unbound DNA and then dried with compressed air.

The biofunctionalized nanowires were mechanically transferred to silicon or glass substrates and then investigated with fluorescence microscopy.

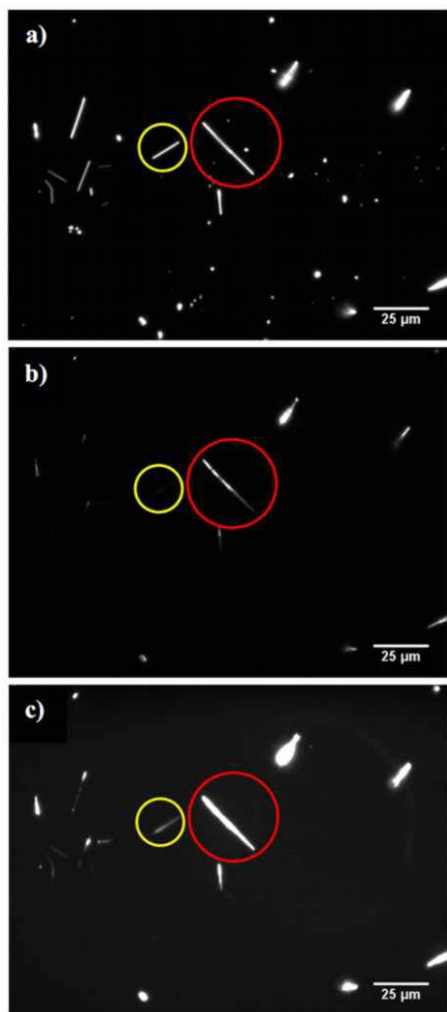


Fig. 1: Dark field (a) and fluorescence (b and c) images of biofunctionalized ZnO nanowires. Nanowires that are not visible in (b) show up at enhanced image contrast in (c).

## Results

Dark field and fluorescence images of biofunctionalized nanowires are shown in figure 1. All functionalized nanowires show fluorescence, but with different intensities. While not every wire is visible to the eye in 1 (b), the covered wires can clearly be seen in figure 1 (c) with aligned image contrast. The intensity contrast can be related to different wire thicknesses and thus more fluorescent molecules on the surface. The thickness variations are not resolvable in an optical microscope. The nanowire diameters can easily differ by a factor of 2 or more with the applied growth method [5], leading to a fluctuation in the amount of

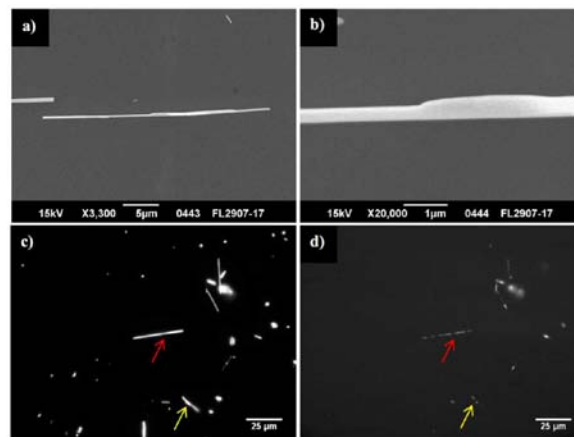


Fig. 2: Nanowires with inconsistent thickness (SEM images in a and b) show a small intensity contrast along the nano-wire in the dark field image (c) and a huge contrast in the fluorescence picture (d).

fluorescent molecules per nanowire by a factor of 4.

Figure 2 (c) and (d) show dark field and fluorescence images of nanowires with inconsistent thickness observable in the SEM pictures in figure 2 (a) and (b). The thickness variation along the nanowires leads to a contrast in fluorescence intensity.

The fluorescence studies have also been carried out on only silanized and as-grown nanowires (not shown here). As there was no fluorescence visible, autofluorescence of the ZnO wires can be excluded as fluorescence origin. Control experiments have also been carried out with ZnO bulk crystals (not shown here). In this case, the biofunctionalized crystal regions showed a strong fluorescence, confirming the functioning of the applied biofunctionalization method.

## References

- [1] Y. Cui, C. Lieber et al., *Science* 17 Vol. 293 no. 5533 (2001)
- [2] Z. L. Wang, *Annu. Rev. Phys. Chem.* 55, pp 159-196 (2004)
- [3] M. H. Hunag et al., *Adv. Mater.* 13(2), pp 113-116 (2001)
- [4] C. Corso et al., *Biosens. Bioelectron.* 24 811-7 (2008)
- [5] C. Borchers, C. Ronning et al., *J. Phys. Chem. B* 110(4), pp 1656-1660 (2006)
- [6] H.-W. Ra et al., *Mater. Lett.* 63(28), pp 2516-2519 (2009)

# Protein adsorption behavior on Si and TiO<sub>2</sub> nanoripples

J. Sommerfeld, J. Hönig, R. Niepelt, T. F. Keller\*, K. D. Jandt\* and C. Ronning

\* Institute for Materials Science and Technology (IMT), Friedrich Schiller University, Löbdergraben 32, 07743 Jena

## Introduction

In the field of biomaterial research titanium dioxide (TiO<sub>2</sub>) is of particular interest as cover material for artificial replacements or nickel titanium (NiTi) stents, because of its non-toxic, non-allergenic and biocompatible character. Silicon on the other hand is ideal as reference material. By variation of the surface morphology via ion beam bombardment we investigated the adsorption behavior of proteins on such surfaces. Human Plasma Fibrinogen (HPF) was the protein of choice, because of its importance for the blood coagulation process. Most notably, it is well understood and has a so-called amphiphilic character, which means that due to its hydrophobic and hydrophilic parts it is attracted to hydrophobic and hydrophilic surface states but assumes different formations, as shown in figure 1. [1]

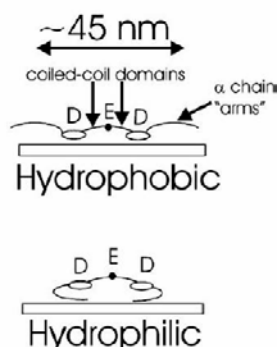


Figure 1: On a hydrophobic surface HPF adsorbs in a stretched, trinodular formation whereas on a hydrophilic substrate a rather globular formation could be observed. [1]

## Experimental

To generate morphology changes of the referring surfaces, Si and TiO<sub>2</sub> single

crystals were irradiated with Xe<sup>+</sup> ions of different ion energies (7-20 keV). With respect to the ion energies, fluences and incident angle, ripple formations with different wavelength and amplitudes could be obtained. A detailed explanation of the ripple formation process is presented elsewhere [2] [3]. The investigations of the surface before and after protein adsorption as well as cross sections were performed with a MultiMode AFM by Veeco with a Nanoscope III controller.

For the protein adsorption four sets of modified Si and TiO<sub>2</sub> substrates with wavelength of approximately 40 nm up to 150 nm were prepared (see figure 2). Additionally plane, untreated samples have been investigated as well.

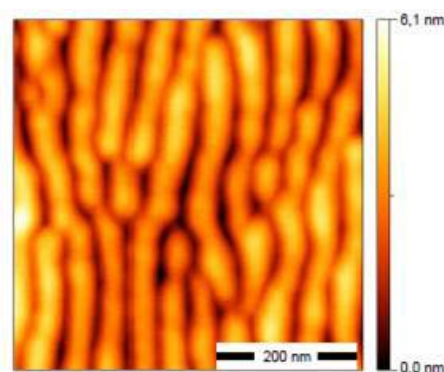


Figure 2: AFM measurement of a ripple structure ( $\lambda = 52\text{nm}$ ) on a Si substrate. [4]

The HPF was dissolved in PBS (phosphate buffered solution) with a concentration of  $c_{\text{HPF}} = 10 \mu\text{g/ml}$ . The samples were cleaned with ethanol and dried. Afterwards the substrates were stored in the HPF solution for 2h at 37°C (human body environment). Thereupon the samples were carefully cleaned with distilled water and



investigated via AFM within 24h to assure the stability of the adsorbed proteins.

## Results

The adsorption behavior of HPF varies with the surface morphology as can be seen in figure 3. Due to the trinodular formation on plane Si an almost ring like structure could be observed (a), whereas on plane TiO<sub>2</sub> the globular formation outweighs (b). For short ripples wavelength ( $\lambda < 100\text{nm}$ ) the adsorption behavior is quite different. On Si (c) the proteins seem to align along the ripples, whereas no adsorption could be observed on TiO<sub>2</sub> (d).

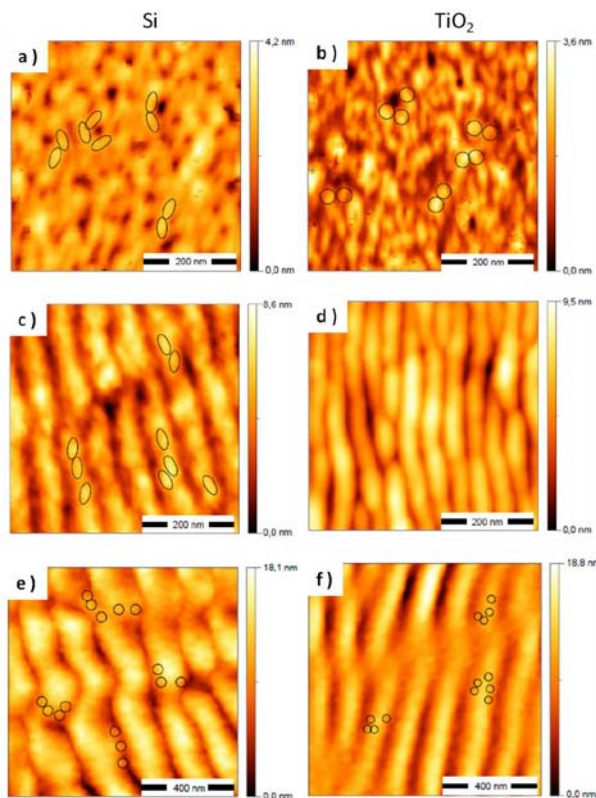


Figure 3: Protein adsorption on Si and TiO<sub>2</sub> substrates with different surface morphologies. a) Rather trinodular like formation of HPF on planar Si. b) Globular formation on planar TiO<sub>2</sub>. c) Trinodular formation along the short-wave ripples ( $\lambda < 100\text{ nm}$ ) on Si and d) no adsorption at all on short-wave TiO<sub>2</sub> ( $\lambda < 100\text{ nm}$ ). e - f) globular formation of HPF on long-wave Si respectively TiO<sub>2</sub> ( $\lambda > 100\text{ nm}$ ).

Cross section measurements confirmed the interpretation of the AFM analysis. For the Si sample an increase of the average ripples amplitude of about 1 nm was determined. This corresponds to the assumed height of a stretched HPF protein. The cross section of the TiO<sub>2</sub> samples showed no change in amplitude. Hence, HPF does obviously not adsorb on short-wave TiO<sub>2</sub>. In the case of long wavelengths ( $\lambda > 100\text{nm}$ ) HPF adsorbs globularly for Si and TiO<sub>2</sub> substrates (e-f). Additionally, contact angle measurements have been performed but did not contribute to a general understanding of the obtained dependencies. [4]

## Conclusion

By variation of the surface morphology via ion beam bombardment we are able to influence the adsorption behavior of HPF. Although the wavelength clearly affects the adsorption behavior of HPF, there has to be another influence that causes the non-adsorption on short-wave TiO<sub>2</sub>. Eventually occurring stoichiometric changes at the surface due to the ion bombardment are of a certain importance.

## References

- [1] K. L. Marchin and C. L. Berrie: *Conformational Changes in the Plasma Protein Fibrinogen upon Adsorption to Graphite and Mica Investigated by Atomic Force Microscopy*, *Langmuir* **19**, 9883-9888 (2003)
- [2] R. Niepelt: *Aufbau und Anwendung eines Mikroionenstrahls zur Untersuchung der Musterbildung durch Sputtererosion*, Diplomarbeit, (2008)
- [3] S. Kosan: *Ionenstrahlerosion von TiO<sub>2</sub>*, Bachelorarbeit, (2010)
- [4] J. Hönig: *Untersuchungen zur Adsorption von Proteinen auf nanostrukturierten Oberflächen*, Diplomarbeit, (2010)

# Modelling the Quantum Efficiency of Cadmium Telluride Solar Cells

M. Hädrich, H. Metzner, U. Reislöhner, C. Kraft

Measurements of quantum efficiency (QE) are a useful tool to trace generation and loss of photocurrent in optoelectronic devices such as thin-film solar cells.

Quantum efficiency is defined as the ratio of extracted electric charges to the number of incident photons. Numerical QE modelling requires a large set of input parameters a lot of which are not easily accessible. Analytical models however usually rely on few parameters only, an important one of which is the minority carrier lifetime [1].

In the commonly used analytical model by Gärtner [2], photocurrent collection in the electric field of the space-charge region (SCR) of a p-n solar cell is considered complete, i.e. recombination losses are neglected. This case applies for cells in which the photocurrent is predominantly generated in the neutral region (outside the electric field of the SCR). In a cadmium telluride (CdTe) thin-film solar cell with weakly p-doped absorber ( $\sim 10^{14} \text{ cm}^{-3}$ ), the SCR extends to several  $\mu\text{m}$ , i.e. deeper than the absorption length. Hence, generation of photocurrent and recombination losses predominantly occur within the SCR.

We introduce a simple analytical model for quantum efficiency in which the specific situation of incomplete photocurrent collection in the space-charge region is taken into account. The fundamental optical and electrical parameters were measured on experimental CdTe solar cells from our own laboratory.

QE depending on the wavelength  $\lambda$  is calculated from the generation and collection functions  $G$  and  $C$ , respectively, by one-dimensional spatial integration:

$$QE(\lambda) \sim \int_x G(x', \lambda) C(x') dx'. \quad (1)$$

$G(x', \lambda) = \alpha(\lambda) \exp[-\alpha(\lambda)x']$  describes depth dependent generation with the spectral absorption coefficient  $\alpha(\lambda)$ .

$C(x')$  entails the temporal decay of the photogenerated carriers during transport, which is  $\exp(-t/\tau_e)$  in general,  $t$  being the time and  $\tau_e$  the lifetime of the electrons (minority carriers). In our model, we use the following assumptions: (i) the SCR is on the p-CdTe side of the p-n junction, due to significantly higher doping of n-CdS, (ii) CdS does not contribute to the photocurrent, (iii) the electric field is homogeneous with an average half maximum value  $E_0/2$  instead of linearly decreasing with depth. The collection functions of the SCR and of the neutral region are calculated based on these considerations, consistent with the Drude theory. Further details are published elsewhere [3]. We obtain the complete QE:

$$QE = T_{sub} \times \exp(-\alpha_{CdS} d_{CdS}) \times \left(1 + \frac{S \times W}{\mu_e 2V_{bi}}\right)^{-1} \times \left\{ \frac{L_{Drift}}{L_{Drift} + \frac{1}{\alpha_{CdTe}}} \left[1 - \exp\left(-W \left[\alpha_{CdTe} + \frac{1}{L_{Drift}}\right]\right)\right] + \frac{L_e}{L_e + \frac{1}{\alpha_{CdTe}}} \exp\left(-W \left[\alpha_{CdTe} + \frac{1}{L_{Drift}}\right]\right) \right\}. \quad (2)$$

The parameters in Eq. (2) are explained in Table 1. Most of them were measured except the free variables  $S$  and  $\tau_e$ . The lifetime  $\tau_e$  is included both in  $L_{Drift} = \mu_e \tau_e E_0/2$  and in  $L_e = kT/e \times \mu_e \tau_e$  (Boltzmann constant  $k$ , temperature  $T$ , elemental charge  $e$ ,  $E_0 = 2V_{bi}/W$ ).  $L_{Drift}$  and  $L_e$  are average paths of the electrons before recombination, the former within the electric field of the SCR and the latter within the field-free neutral region.



$T_{\text{sub}}(\lambda)$	transmission of substrate	m
$\alpha_{\text{CdS}}(\lambda)$	absorption coefficient of CdS	m
$d_{\text{CdS}}$	thickness of CdS window layer	m
$S$	interface recombination velocity	v
$W$	width of SCR	m
$\mu_e$	electron mobility	c
$V_{\text{bi}}$	built-in voltage of p-n junction	m
$L_{\text{Drift}}$	drift length	d
$\alpha_{\text{CdTe}}(\lambda)$	absorption coefficient of CdTe	m
$L_e$	diffusion length	d
$\tau_e$	electron lifetime	v

Table 1: Parameters in Eq. (2); m=measured, v=free variable, c=constant, d=dependent on v.

$S$  is included in  $h=[1+S \times W/(2\mu_e V_{\text{bi}})]^{-1}$  in Eq. 2. The factor  $h$  describes recombination losses at the p-n heterojunction interface and is wavelength independent [4], with a range between 0 and 1 or rather between 0.95 and 1 for good solar cells.

In Fig. 1, experimental QE data are shown which were fitted by our analytical model. The only free parameter is  $\tau_e$ .

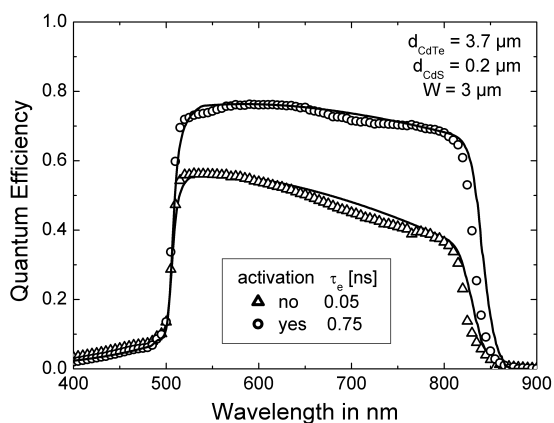


Fig. 1: Experimental QE curves of cells with 3.7  $\mu\text{m}$  CdTe thickness (symbols) with and without activation. The fit curves (solid lines) using Eq. (2) show improved electron lifetime  $\tau_e$  after the treatment.

The calculated QE curves are in good agreement with the measured ones. After the thermo-chemical activation treatment, which is critical for the performance of CdTe solar cells,  $\tau_e$  improves significantly. Another example is shown in Fig. 2.

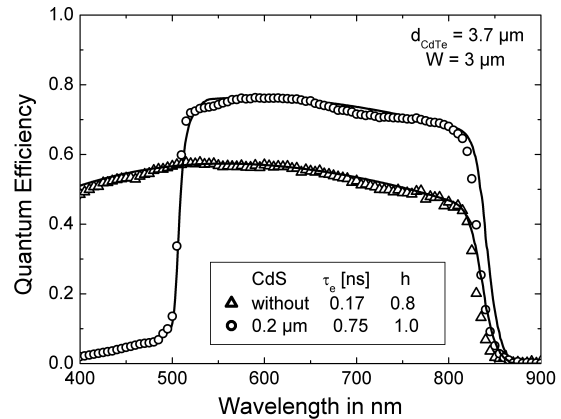


Fig. 2: Experimental QE curves (symbols) with and without CdS window layer. The parameters for the fit curves (solid lines) are  $\tau_e$  and  $h$ .

Both  $\tau_e$  and  $h$  are adjusted in order to attain close fits. The solar cell without CdS window layer has a lower QE plateau, mainly due to higher interface recombination velocity at the p-n junction.

Application of our model to solar cells allows differentiation between optical losses and electrical losses either by bulk or by interface recombination. The lifetimes obtained by fitting experimental data of CdTe cells with our model are between 0.01 and 1 ns and thus correspond to those measured by time-resolved photoluminescence [5]. Furthermore the results show lifetimes of about 1 ns to be necessary for highly efficient solar cells.

This work was funded by Bundesministerium für Umwelt, Naturschutz und Reaktorsicherheit and Thüringer Kultusministerium.

## References

- [1] S.S. Hegedus, W.N. Shafarman, Prog. Photovolta.: Res. Appl. 12 (2004) 155.
- [2] W.W. Gärtner, Phys. Rev. 116 (1959) 84.
- [3] M. Hädrich, H. Metzner, U. Reislöhner, C. Kraft, Sol. Energy Mater. Sol. Cells 95 (2011) 887–893.
- [4] K.W. Mitchell, A.L. Fahrenbruch, R.H. Bube, J. Appl. Phys. 48 (1977) 4365.
- [5] W.K. Metzger, D. Albin, M.J. Romero, P. Dippo, M. Young, J. Appl. Phys. 99 (2006) 103703.

# Back Contact Formation in Cadmium Telluride Thin Film Solar Cells

M. Hädrich, C. Heisler, U. Reislöhner, C. Kraft, H. Metzner

A common feature of the electronic properties of CdTe solar cells is the appearance of the roll-over in the current-voltage (I-V) characteristic. Instead of the ideal exponential diode characteristic, an inflexion point is observed in the vicinity of the open-circuit voltage ( $V_{oc}$ ) thus limiting the forward current of the diode. The undesired roll-over phenomenon mainly affects the solar cell efficiency by reducing the fill factor. In the literature, the roll-over is mostly explained by a Schottky barrier at the back contact [1].

Measured J-V (current density vs. voltage) characteristics of CdTe solar cells with Au and Cu-Au back contact are shown in Fig. 1. In the case of cells with Au back contact, the increase of the roll-over with increasing CdTe thickness becomes apparent. Cells with 0.2 to 1.0  $\mu\text{m}$  thicknesses show almost no roll-over. At 2.0  $\mu\text{m}$ , the roll-over is significant and for 3.5 and 5.0  $\mu\text{m}$  even more pronounced, with a tendency to forward current saturation. In contrast to these results, the cells with Cu-Au contact were found to yield no appreciable roll-over. Hence, the roll-over can be identified as an issue of the back contact formation and has to be attributed both to the CdTe thickness and to the Au back contact.

A helpful approach to understand the roll-over phenomenon is to describe the solar cell as the series connection of two diodes. The p-n junction is represented by a diode with dark saturation current  $I_{01}$  and the back contact by a reverse diode with dark saturation current  $I_{02}$  and shunt resistance  $R_{sh}$ . The J-V characteristics of the complete device is obtained by numerically forming the inverse diode characteristics  $V_1(J)$  and  $V_2(J)$  and by summation of these voltages.

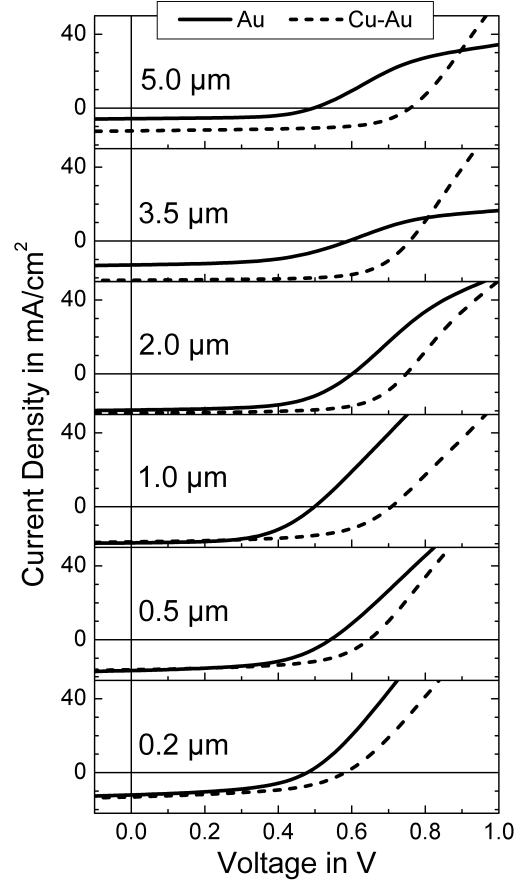


Fig. 1 Experimental J-V characteristics of solar cells with Au back contact (solid lines) and Cu-Au back contact (dashed lines). The CdTe thickness was varied between 0.2 and 5  $\mu\text{m}$ .

A similar model has been suggested in the literature [2, 3]. Thus, the J-V characteristic of a CdTe solar cell including the roll-over can be computed accurately. The saturation current density of the back contact diode  $J_{02}$  is directly given by the inflexion point in the J-V characteristic and yields information on the height of the back contact barrier  $\Phi_b$ . Assuming thermionic emission, the relation is given by [4]

$$J_{02} = ev_r N_v \exp(-e\Phi_b/kT), \quad (1)$$

in which  $e$  is the elementary charge of the electron,  $v_r$  the Richardson velocity,  $N_v$  the effective density of states in the valence

band,  $k$  the Boltzmann constant and  $T$  the temperature. Using Eq. (1), the evaluation of the J-V data in Fig. 1 yields different  $\Phi_b$  values for the samples with Au contact and different CdTe thicknesses. However, this model cannot explain why  $\Phi_b$  is thickness dependent.

A different approach describing the implications of the back contact barrier on the properties of the CdTe solar cells has been suggested by Roussillon et al. [5]. These authors assume the space charge region of the main junction and the one of the back contact to overlap, depending on the barrier height of the back contact. Thus, the changed band diagram would affect the collection and recombination of the carriers significantly.

In order to study this effect, we performed numerical calculations of the energy band diagram depending on the CdTe thickness using the simulation tool SCAPS-1D [6]. The valence band part of the discussed band diagram is shown in Fig. 2 for CdTe thicknesses between 0.5 and 3.5  $\mu\text{m}$ .

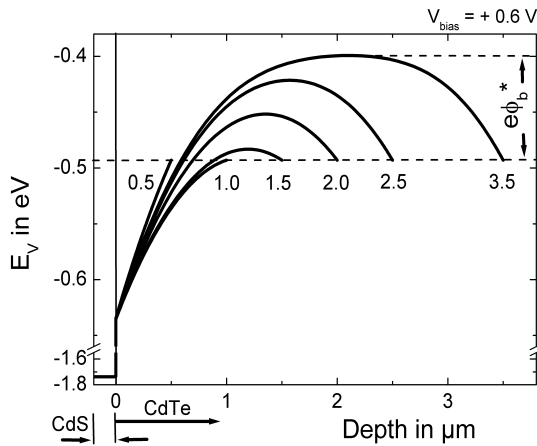


Fig. 2 Simulation of the depth dependence of the valence band energy  $E_v$  in a CdTe solar cell.  $E_v$  under forward bias and standard illumination conditions is shown for CdTe thicknesses between 0.5 and 3.5  $\mu\text{m}$ . The respective effective back contact barrier is  $e\Phi_b^*$ .

The marked effective back contact barrier  $\Phi_b^*$  is associated with  $\Phi_b$  according to:

$$\Phi_b = \Phi_b^* + (E_F - E_v)/e \quad (2)$$

In the band diagram, distinct space charge regions are visible at the p-n junction and at the back contact for 3.5  $\mu\text{m}$  CdTe thickness. However, when the thickness is reduced, the space charge regions overlap resulting in a reduced effective barrier height  $\Phi_b^*$ . If the CdTe film is sufficiently thin, i.e. 1  $\mu\text{m}$  or less, the barrier disappears completely.

The evaluation of  $\Phi_b^*$  from the band diagram simulation yields a good agreement with the values extracted from experimental J-V data using Eq. (1) [7].

Hence, our investigations not only reveal the back contact barrier to cause the roll-over but also allow quantifying the dependence on the thickness of the CdTe films. The back contact barrier and the roll-over can be eliminated for sufficiently small absorber thicknesses even if a simple Au contact is used. Although cells with Cu-Au contact generally yield better performances, this concept is beneficial for contacts to extremely thin absorbers, when Cu incorporation has to be avoided for stability reasons.

This work was funded by Bundesministerium für Umwelt, Naturschutz und Reaktorsicherheit and Thüringer Kultusministerium.

## References

- [1] A.L. Fahrenbruch, Mater. Res. Soc. Symp. Proc. 1012 (2007), p.583, San Francisco, CA, USA.
- [2] A. Niemegeers, M. Burgelman, J. Appl. Phys. 81 (1997) 2881.
- [3] S.H. Demtsu, J.R. Sites, Thin Solid Films 510 (2006) 320.
- [4] S.M. Sze, Physics of Semiconductor Devices, Wiley, New York, 1981.
- [5] Y. Roussillon, V.G. Karpov, D. Shvydka, J. Drayton, A.D. Compaan, J. Appl. Phys. 96 (2004) 7283.
- [6] M. Burgelman, P. Nollet, S. Degraeve, Thin Solid Films 361 (2000) 527.
- [7] M. Hädrich, C. Heisler, U. Reislöhner, C. Kraft, H. Metzner, Thin Solid Films (2010), doi:10.1016/j.tsf.2010.12.144.

## The zinc oxide – molybdenum specific contact resistance for applications in Cu(In,Ga)Se<sub>2</sub> solar cell technology

M. Oertel, S. Götz, J. Cieslak, J. Haarstrich, H. Metzner, and W. Wesch

We developed an improved measuring structure based on the transmission line model (TLM) which allows us to determine the specific contact resistance between rf-sputtered aluminium doped zinc oxide (ZnO:Al) and dc-sputtered molybdenum despite inhomogeneities in film thickness and conductivity which normally prevent an accurate determination of this value with the TLM. The improvement was achieved by an interchange between the contact and the conduction bar material to get a lower resistance of the conduction bar. Using this structure, the specific contact resistance is ascertained to be  $(1.37 \pm 0.14) \times 10^{-5} \Omega \text{cm}^2$ . In addition, the effects of variations of certain sputter deposition parameters and their influence on the specific contact resistance are demonstrated. In particular, a small amount of oxygen in the sputter gas during the molybdenum sputter process remarkably increases the specific contact resistance. For an optimization of the integrated series connection of Cu(In,Ga)Se<sub>2</sub> (CIGS) thin-film solar cells, it is important to know the exact specific contact resistance between aluminium doped zinc oxide (ZnO:Al) and molybdenum (Mo). This knowledge allows the calculation of the exact series resistance of CIGS solar cell modules with tens to hundreds of such contacts and to search for an optimum between the contact widths, the current transport, and the loss of active area as discussed e.g. by Burgelman et al. [1]. Many efforts have been made to determine the specific contact resistance between ZnO:Al and different metals [2,3]. Unfortunately, the literature values for the specific contact resistance between ZnO:Al and mo-

lybdenum vary in the range from  $2 \times 10^{-4}$  to  $0.2 \Omega \text{cm}^2$  [4,5,6]. We perform I-U-measurements at specially designed test structures the results of which are analysed by means of the transmission line model (TLM) [7]. As H.H. Berger showed [7], in case of direct current, the resistance  $R_C$  between a semiconductor and a metal can be calculated by

$$R_C = \frac{\sqrt{R_S \cdot \rho_C}}{w} \times \coth\left(\frac{d}{L_T}\right) \quad (1),$$

where  $R_S$  is the sheet resistance of the semiconductor bar,  $\rho_C$  is the specific contact resistance,  $d$  is the length,  $w$  the width of the contact, and  $L_T$  is the transfer length given by

$$L_T = \sqrt{\rho_C / R_S} \quad (2).$$

The typical structure is shown in Figure 1a with the important dimensions given in Figure 1c. Plotting the resistance between two contacts

$$R(l) = 2R_C + \frac{R_S}{w} \times l \quad (3)$$

versus the distance  $l$  of the contacts yields  $2 \times R_C$  by extrapolating to  $l = 0$  and  $R_S$  by multiplying the slope of the graph with  $w$ . Here, a kind of inverted TLM structure was employed. Figure 1b shows the modified structure. The resistivity of molybdenum is about three orders of magnitude lower than that of ZnO:Al and so inhomogeneities in the sheet resistance of the molybdenum lead to much smaller errors. The Mo bar itself is composed of two layers of molybdenum following the idea of Scofield et al. [8]. Here, only the thickness of the ZnO:Al layer was varied between 120 and 480 nm.

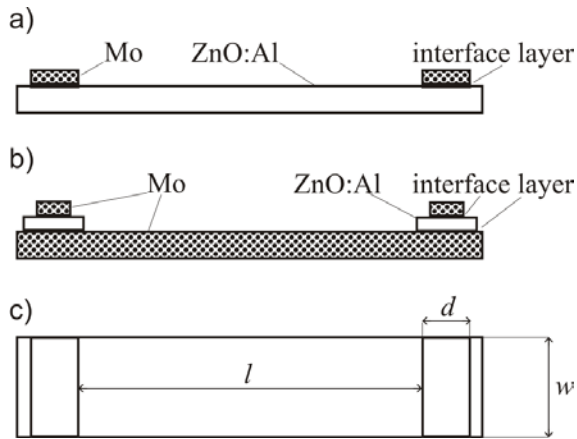


Fig. 1 (a) Conventional TLM test structure for determination of Mo-ZnO:Al-specific contact resistance (cross section), (b) improved TLM test structure (cross section), (c) geometric dimensions of the TLM test structure (top view).

A demonstration of the independence of the specific contact resistance and the ZnO:Al-layer thickness is given in Figure 2. The calculated specific contact resistance is plotted versus the thickness of the ZnO:Al-layer. In this Figure, the error bars mark the statistical error of the mean value of several measurements at identically processed sample structures. From the experimental data, a weighted average value for the specific contact resistance of  $(1.37 \pm 0.14) \times 10^{-5} \Omega\text{cm}^2$  is determined. The weighted average and its standard deviation are used to accommodate the variation of the results at each ZnO:Al-layer thickness. The result thus achieved is the lowest value for the specific contact resistance reported in the literature and provides the opportunity of further improvement in CIGS-solar cell interconnection.

However, the effect of oxygen in the sputter gas is remarkable, since a little amount of oxygen in the sputter gas during the molybdenum sputter process strongly increases the specific contact resistance between molybdenum and ZnO:Al (data not shown). Since ZnO:Al is known to become highly resistive if it is sputtered with argon plus oxygen, the increase of the specific contact

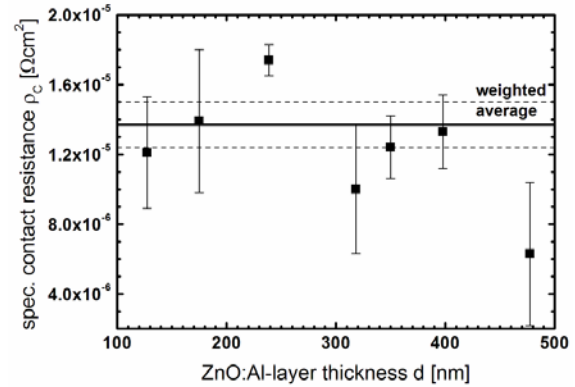


Fig. 2 Plot of the specific contact resistance between ZnO:Al and Mo with changing ZnO:Al-layer thickness. The calculated weighted average value (straight line) with its standard deviation (dashed lines) is also plotted.

resistance can possibly be explained by oxygen diffusion into the ZnO:Al-surface layer.

In conclusion, an improved TLM test structure was introduced yielding the specific contact resistance at the interface of sputtered molybdenum and ZnO:Al layers to be  $(1.37 \pm 0.14) \times 10^{-5} \Omega\text{cm}^2$  for optimized deposition parameters.

The authors would like to thank the BMU for financial support under the contract number 0327665E.

## References

- [1] M. Burgelman, A. Niemegeers, Sol. Energy Mater. Sol. Cells 51 (1998) 129.
- [2] H.-K. Kim, J.-M. Lee, Superlattices Microstruc. 42 (2007) 255.
- [3] H.-K. Kim, J. W. Bae, K.-K. Kim, S.-J. Park, T.-Y. Seong, I. Adesida, Thin Solid Films 447-448 (2004) 90.
- [4] J. Wennerberg, J. Kessler, L. Stolt, Sol. Energy Mater. Sol. Cells 67 (2001) 59.
- [5] J. Johansson, Rapport EBD-R--08/19, Lunds University, ISSN 1651-8128 (2008).
- [6] A. E. Delahoy, L. Chen, M. Akhtar, B. Sang, S. Guo, Sol. Energy 77 (2004). 785
- [7] H. H. Berger, Solid-State Electron. 15 (1972) 145.
- [8] J. H. Scofield, A. Duda, D. Albin, B. L. Ballard, P.K. Predecki, Thin Solid Films 260 (1995) 26.

## Production of CIGS solar cells in a non-vacuum process using high-temperature sintering

C.Wolf, W.Wesch, H.Metzner, L.Hentschel, M.Oertel

In 2010, the project "Production of CIGS solar cells in a non-vacuum process using high-temperature sintering" was completed successfully at the Institute for Solid State Physics.

It was a collaborative project of the promoter "Arbeitsgemeinschaft industrieller Forschungsvereinigungen „Otto von Guericke“ e.V." supported by the "Bundesministerium für Wirtschaft und Arbeit (PRO INNO II)". It was characterized by close cooperation between the partners out of industry and universities. A main goal of the project was to demonstrate a way to produce solar cells with a light absorber out of the chalcopyrite  $\text{CuInSe}_2$  in a process without the use of expensive vacuum systems.

The focus of the work at the IFK within the project was to analyze the solar cell layers produced by the industry partners and to compare the results to the reference process line at the IFK. This was done by employing methods available at the IFK such as SEM, EDX, XRD and IU measurements. Complementing the studies at the IFK, the PL measurements of the cooperation partner TU-Ilmenau helped to establish the desired process successfully.

In the first part of the project, the industry partner tested different ways to grow CIS absorbers on metal foils. Several non-vacuum methods for applying the metallic copper-indium precursor and several selenization methods were investigated. REM analyses in Jena and PL-investigations in Ilmenau showed best results with galvanic deposition of precursor layers.

These precursor layers were then selenized in  $\text{H}_2\text{Se}$  atmosphere at atmospheric pressure. The layers showed a loss of Indium and insufficient homogeneity in morphology and chemical composition as already described in [1].

To increase the homogeneity of the CIS-absorbers in the experiments and to avoid the toxic  $\text{H}_2\text{Se}$  gas, the IFK also carried out experiments on this subject in the second part of the project. For this purpose a new furnace for rapid thermal annealing (RTP) was installed in 2009 [2]. This RTP process allows to avoid the formation of volatile indium-selenides in a temperature range of 350 to 400°C (described in [3]) due to high heating rates.

Precursor layers were prepared (as in the reference process) with a conventional sputter coater and then selenized in a selenium containing argon atmosphere at atmospheric pressure. The resulting absorber films initially showed the stoichiometry of  $\text{Cu}_1\text{In}_1\text{Se}_2$  but still showed inhomogeneities. To improve the homogeneity of the absorber, it was necessary to examine the behavior of the selenium vapor in the atmosphere of the furnace.

It was found that the offered gas flow was not sufficient to equally distribute the selenium vapor over the whole sample. Only an additional deposition of selenium on the samples (SEL method) could ensure the absorber to grow uniformly over the entire surface. Figure 1 and 2 show photographic images of two samples after the selenization with two methods of selenium supply. During the selenization, one of them only reacted with the selenium placed in the



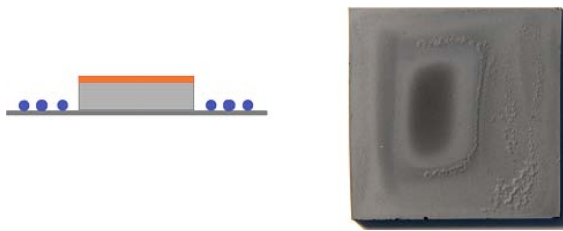


Fig.1: Samples selenized in Ar-atmosphere without additional Se-layer.

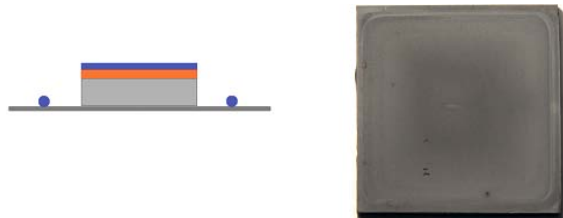


Fig.2: Samples selenized in Ar-atmosphere with additional Se-layer.

chamber, while the other one had an additional selenium. On the other hand, all absorbers which were prepared without additional selenium surrounding the sample were poor of indium. Best results were achieved with selenium deposited above the sample and surrounding it.

Also several other process parameters were varied. For instance by varying the time of selenization it could be shown that even after a selenization of only about 4 minutes no foreign phases except for the  $\text{CuInSe}_2$  phase were detected with XRD measurements in the absorber. This confirms with previous results obtained in our group like [4].

Best results with a selenization in argon atmosphere were achieved with the SEL method, heating rates of 15 K/s, a selenization time of 15 min, a selenization temperature of 500°C, and a limitation of the maximum heating power. Using these parameters, we were able to homogeneously selenize samples of up to 5x5 cm<sup>2</sup> and make cells with conversion efficiencies of up to 8%. In Figure 4, a typical J-V-characteristic of such a cell is shown. Compared to the vacuum reference process at the IFK, we have comparable short circuit currents but less open

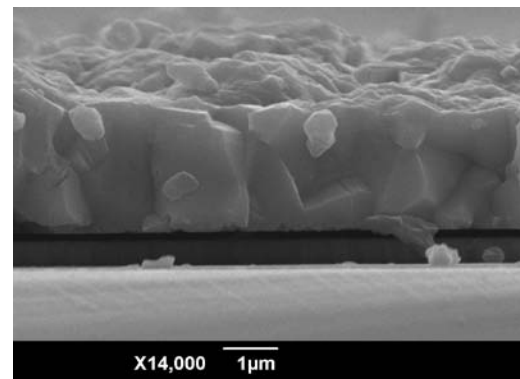


Fig.3: REM image of atmospheric selenized CIS-absorber (cross section)

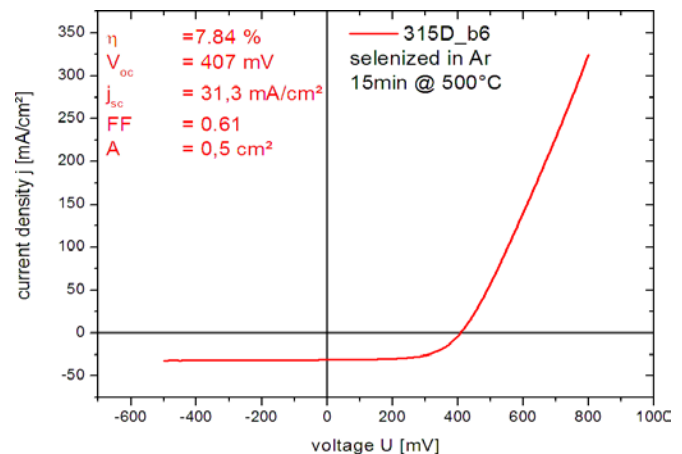


Fig.4: J-V-characteristic of atmospheric selenized CIS-absorber

circuit voltage. Further experiments are necessary to investigate this issue.

With these experiments and analysis the IFK and the cooperation partners were able to successfully demonstrate the possibility of atmospheric preparation of  $\text{CuIn}$ -precursor and  $\text{CuInSe}_2$ -absorber layers for a cheaper solar cell production.

## References

- [1] J. Cieslak, Th. Hahn, B. Poppinga, H. Metzner, W. Witthuhn ; Institut of solid state physics annual report 2007
- [2] C. Wolf, L. Hentschel, M. Oertel, H. Metzner ; Institut of solid state physics annual report 2009
- [3] V. Alberts, J. H. Schön and E. Bucher; Journal of applied physics (1998) Vol84 #12
- [4] M. Oertel. Entwicklung eines sequentiellen Prozesses zur Herstellung von  $\text{CuInSe}_2$ -Dünnschichtsolarzellen. Friedrich-Schiller-Universität Jena, 2007. diploma thesis

# Phosphorus Implanted Cadmium Telluride Solar Cells

C. Kraft, A. Brömel, S. Schönherr, M. Hädrich, H. Metzner, U. Reislöhner, P. Schley<sup>a</sup>,  
G. Gobsch<sup>a</sup>, R. Goldhahn<sup>b</sup>, W. Wesch

<sup>a</sup> *Inst. für Physik, Techn. Universität Ilmenau, PF 100565, 98684 Ilmenau, Germany*

<sup>b</sup> *Inst. für Exp. Physik, Universität Magdeburg, PF 4120, 39016 Magdeburg, Germany*

Polycrystalline cadmium telluride layers were implanted with phosphorus (P) in order to obtain an enhanced p-type doping close to the back contact of CdTe solar cells. The implantation parameters were adjusted based on computer simulations using SRIM. While the implantation profile was kept constant, different CdTe layer thicknesses were investigated. Furthermore, different annealing and activation processes and their influence on the P distribution in the device as well as ion beam induced damage were investigated. The P level was identified by photoluminescence measurements, the effective doping was investigated by means of capacitance-voltage measurements, and the effect on the solar cell properties was analyzed by current-voltage characteristics. The results show the P distribution in the CdTe layer to depend strongly on the thermal and chemical post-implantation treatment. The effect of the P doping on the solar cell properties becomes obvious by an increase of the open-circuit voltage due to the implantation.

According to reference [1], the p-doping of CdTe should be done by using non-equilibrium processes such as ion implantation. No compensating defects should limit this way of p-doping (as long as no annealing occurs). Layers which were grown by molecular beam epitaxy were already successfully doped by phosphorus and other group-V elements [2-4]. In reference [5], the doping of CSS-grown CdTe by ion-implanted antimony with a doping concentration of up to  $10^{16} \text{ cm}^{-3}$  is reported and in reference [6] arsenic doping on MOCVD-

grown CdTe is investigated yielding doping concentrations of up to  $10^{16} \text{ cm}^{-3}$ . However, nitrogen and phosphorus are regarded as the best candidates for p-type doping of CdTe due to their shallow energy levels. It was shown experimentally by means of photoluminescence in single crystalline CdTe [7] that phosphorus has an energy level of 68 meV above the valence band maximum. However, the solar cell properties of implanted polycrystalline devices were not investigated so far.

Figure 1 shows the results of the PL measurements of different samples, which were (i) as-grown (A), (ii) CdCl<sub>2</sub>-activated (B), (iii) P-implanted and annealed (C2), and (iv) P-implanted and CdCl<sub>2</sub>-activated (D).

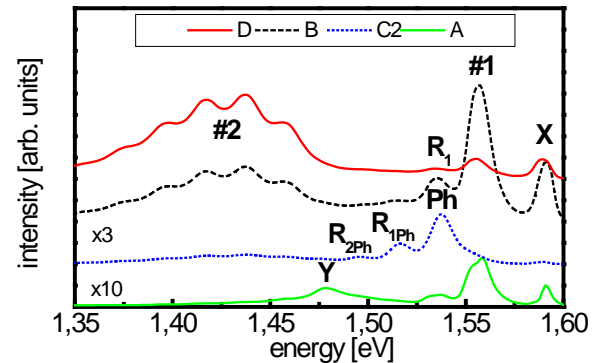


Figure 1: PL measurements of phosphorus implanted samples (C2: implanted and annealed, D: implanted and activated) compared with an as-grown (A) and standard sample (B).

The spectra show typical transitions of excitons (X), free-to-bound transitions (#1) with phonon replica ( $R_1$ ), the so-called Y-band (Y), and a broad band which appears due to any of the applied post deposition treatments (#2). Additionally, another transition level (Ph) with phonon replicas ( $R_{1Ph}$

and  $R_{2Ph}$ ) is created in sample B which can be associated with the phosphorus acceptor state 67 meV above the valence band maximum. The improved doping was also demonstrated by CV measurements. In figure 2 samples of type B and C are compared with respect to the doping profile. The maximum measured doping level was about  $10^{15} \text{ cm}^{-3}$  and up to one order of magnitude higher than in the undoped reference sample, although the intrinsic doping level is quite low in this case.

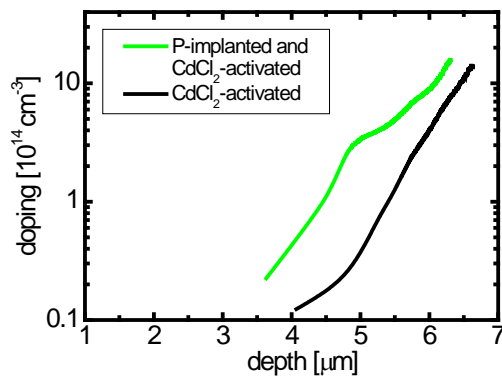


Figure 2: CV measurements which compare an implanted and a standard sample.

Investigating different thicknesses of CdTe absorbers, we can notice that the implantation seems to cause significant damage within the crystalline structure of the cell, and so cells with thin absorbers fail due to the implantation. Still, the IV characteristics of samples with 8  $\mu\text{m}$  absorber thickness were improved by increasing the open circuit voltage by 5%. In figure 3 the IV-characteristics of samples B and C are compared exemplarily. Without implantation, the solar cell characteristics are comparable to earlier results [8]. After the implantation the open circuit voltage was increased from  $738 \pm 6 \text{ mV}$  to  $774 \pm 10 \text{ mV}$ . This increase of the open circuit voltage is due to the increased doping at the rear side of the cell which is expected to lead to an improved back contact and a back surface field.

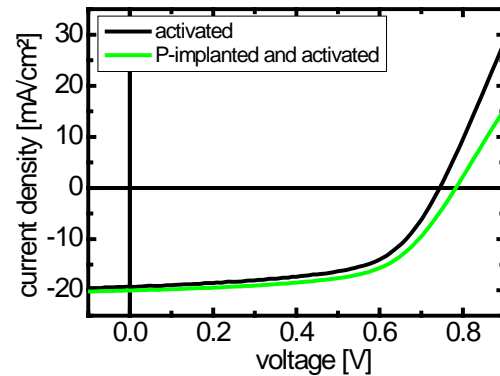


Figure 3: IV characteristics which compare an implanted and a standard sample.

Furthermore, solar cells can not be prepared successfully after the implantation without an annealing with  $\text{CdCl}_2$ . This activation step is still crucial for well operating CdTe solar cells.

This work is part of a project which is supported by the Bundesministerium für Umwelt, Naturschutz und Reaktorsicherheit (BMU).

## References

- [1] Su-Huai Wei, B.S. Zhang, Phys. Rev. B 66 (2002) 155211.
- [2] T. Baron, K. Saminadayar, N. Magnea, J. Fontenille, Journal of Applied Physics 83 (1998) 1354.
- [3] H.L. Hwang, K.Y.J. Hsu, H. Y. Ueng, Journal Crystal Growth 161 (1996) 73.
- [4] Y. Hatanaka, M. Niraula, A. Nakamura, T. Aoki, Applied Surface Science 175-176 (2001) 462.
- [5] H. Zhao, Alvi Farah, D. Morel, C.S. Ferekides, Thin Solid Films 517 (2009) 2365–2369.
- [6] R.L. Rowlands, S.J.C. Irvine, V. Barrioz, E.W. Jones, D.a.Lamb, Journal of Semiconductor Science and Technology 23 (2008) 015017.
- [7] E. Molva, J.L. Pautrat, K. Saminadayar, G. Milchberg, N. Magnea, Phys. Rev. B 30 (1984) 3344.
- [8] M. Hädrich, C. Kraft, C. Löffler, H. Metzner, U. Reislöhner, W. Witthuhn, Thin Solid Films 517 (2009) 2282.

# Increased homogeneity and open-circuit voltage of Cu(In,Ga)Se<sub>2</sub> solar cells due to higher deposition temperature

J. Haarstrich, H. Metzner, M. Oertel, C. Ronning, T. Rissom\*, C.A. Kaufmann\*, T. Unold\*, H.W. Schock\*, W. Mannstadt\*\*, E. Rudigier-Voigt\*\*

\*Helmholtz-Zentrum Berlin für Materialien und Energie, Solar Energy Research, Institute for Technology, Hahn-Meitner-Platz 1, 14109 Berlin

\*\*Schott AG, Hattenbergstraße 10, 55122 Mainz

Recent studies on Cu(In,Ga)Se<sub>2</sub> (CIGS) thin-film solar cells suggest the homogeneity of the CIGS absorber layer to be a key issue in production of high-efficiency thin-film solar cells [1-3]. This concerns lateral as well as vertical homogeneity of different physical properties. Theoretical and experimental investigations clearly show how lateral variations of the local open-circuit voltage can deteriorate the global solar cell performance [1,2]. The commonly employed vertical Ga-gradient in the absorber may be beneficial, but can also be detrimental for solar cell performance [3]. We discuss how a higher temperature of the substrate during absorber deposition can reduce both the lateral inhomogeneity and the vertical Ga-gradient and, thus, be a simple and important contribution to achieving highly efficient CIGS solar cells.

Standard absorbers were fabricated on Mo-coated soda lime glass at the Helmholtz-Zentrum-Berlin using substrate temperatures of 530°C (LT samples) [4]. The high temperature (HT) absorbers were prepared at 610°C in the same high-efficiency baseline on a high-temperature resistant glass designed by Schott AG Mainz without changing any other parameters. Solar cells were fabricated from both types of absorbers using the standard ZnO/CdS-window-structure. The luminescence properties of the absorbers were investigated using cathodoluminescence (CL) at a scanning electron microscope at temperatures of 8 K and acceleration voltages of 10 kV. The crystallographic structure was analyzed by X-ray-

diffraction (XRD), the integral stoichiometry by X-ray fluorescence (XRF).

Normalized CL-spectra of both kinds of absorbers are shown in Figure 1. In both cases the spectra are dominated by one broad emission which is typical for slightly Cu-poor CIGS thin-films [5]. While the shape of the spectra is similar, the energy of the emission line is considerably higher for the HT absorber when compared to the LT absorber. The emission at 1.13 eV (HT) can be assigned to the DA1-transition of CIGS with a [Ga]/([Ga]+[In])-ratio (GGI) of approximately 30% [5], while a luminescence at 0.98 eV originates from pure CuInSe<sub>2</sub>. Note that both LT and HT absorbers contain the same amount of Ga according to XRF data (GGI = 27-30%).

In Figure 2, the XRD (112)-reflection of the chalcopyrite phase is shown for both HT and LT samples. HT samples show one single reflection at 26.94° corresponding to a GGI of around 27±5% [6] indicating a high degree of homogeneity of the vertical Ga-distribution. LT samples exhibit reflections

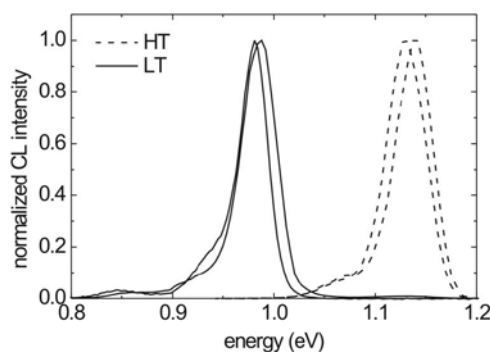


Fig. 1: Normalized CL-spectra of HT and LT absorbers, respectively.

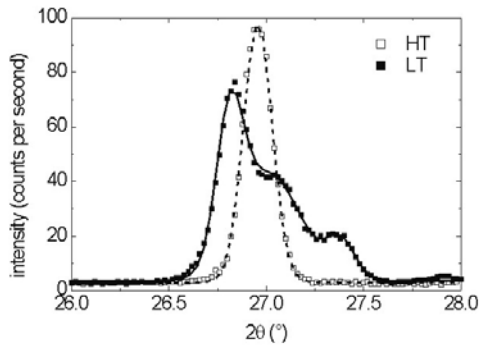


Fig. 2: Fitted XRD patterns of the (112)-reflection of the chalcopyrite ordering for HT and LT samples, respectively.

at  $26.81^\circ$ ,  $27.05^\circ$  and  $27.35^\circ$ , corresponding to regions with a GGI of  $7\pm 7\%$ ,  $27\pm 7\%$  and  $55\pm 13\%$ . SIMS profiles allow us to assign the reflections to the front (GGI = 27%), medium (GGI = 7%) and back (GGI = 55%) region of the absorber, respectively [7].

This analysis helps to elucidate the CL spectra in Figure 1, especially the low temperature case. Here, the thickness of the front layer with a GGI of 27% has a thickness of 200 nm, comparable to the electron penetration range at 10 kV, so most of the electron excitation takes place in the front layer of the LT absorber. But due to diffusion and drift in the quasi-electric-field induced by band gap grading, most recombination will take place in the low band-gap region (GGI = 7%). Hence, the band gap of the medium layer which is close to the one of pure  $\text{CuInSe}_2$  governs the observed recombination.

The lateral homogeneity is analyzed by spatially resolved detection of luminescence spectra. While only a slight fluctuation in the energy of the peak maximum (20 meV) is observed for HT absorbers, the peak shifts over a range of 80 meV for the LT case (not shown), thus showing the higher temperature to reduce the lateral homogeneity of the absorber layer.

The j-V-characteristics of a solar cell made from HT-absorbers are shown in Fig. 3. A

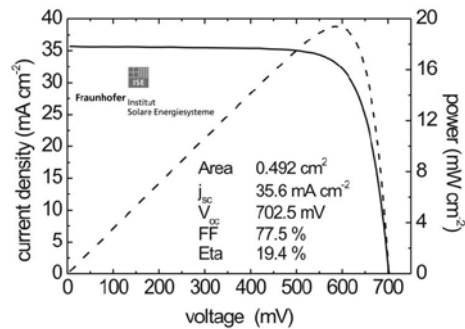


Fig. 3: j-V-characteristic of the best cell with an  $\text{MgF}_2$  AR-coating obtained with the high-temperature process as certified by Fraunhofer ISE.

certified efficiency of 19.4% is obtained, showing an increase in open-circuit voltage of almost 100 mV compared to the standard LT process. Together with an improved fill factor it overcompensates a loss in short-circuit current density. The latter is due to the higher effective band-gap corresponding to the homogeneous Ga-distribution.

In conclusion, CIGS absorbers deposited at higher substrate temperatures reveal (i) a reduced lateral variation of luminescence peak-energy and (ii) a strongly reduced vertical Ga-grading in the absorber layer. Solar cells made from these absorbers show a considerable improvement of the solar cell performance.

The authors would be like to thank the BMU for financial support under the contract number 0327665B/D/E.

## References

- [1] V.G. Karpov et al., *Appl. Phys. Lett.* **80** (2002), 4256.
- [2] G.H. Bauer et al., *Thin Solid Films* **480** (2005), 259.
- [3] M. Gloeckler, J.R. Sites, *J. Phys. Chem. Solids* **66** (2005), 1891.
- [4] Kaufmann et al., *Sol. Energy Mater. Solar Cells* **93** (2009), 859.
- [5] N. Rega et al., *Thin Solid Films* **480–481** (2005), 286.
- [6] M.R. Balboul et al., *Appl. Phys. A* **92** (2008), 557.
- [7] J. Windeln et al., *Proceedings of the 24th EU PVSEC*, Hamburg (2009), 2443.



# Investigation of the Excitonic Luminescence Band of CdTe Solar Cells by Photoluminescence Excitation Spectroscopy

C. Kraft, M. Hädrich, H. Metzner, U. Reislöhner, P. Schley\*, and R. Goldhahn\*#

\**Inst. für Physik, Techn. Universität Ilmenau, PF 100565, 98684 Ilmenau, Germany*

#*Inst. für Exp. Physik, Universität Magdeburg, PF 4120, 39016 Magdeburg, Germany*

Polycrystalline cadmium telluride (pc-CdTe) is an established material for the production of low-cost solar cells. However, a detailed understanding of intrinsic defects and their changes due to post deposition treatments, is still outstanding. A post deposition treatment or activation is essential for well performing CdTe solar cell devices. The commonly employed substance for activation is cadmium chloride ( $\text{CdCl}_2$ ), but experiments with hydrochloric acid or sodium chloride were also reported [1,2].

Photoluminescence excitation spectroscopy (PLE) is particularly suitable in order to gain information on the recombination pathways of certain radiative transitions and also to observe transitions which normally cannot be seen in PL spectra.

The excitonic emission region in the PL spectra of CdTe is especially important. Some peaks in the excitonic luminescence band can be attributed to excitons bound to defects [3]. These defects are normally responsible for other transitions at lower energies, too, so correlations such as Haynes rule [4] can be applied. For single crystalline CdTe, many investigations were done, which propose the existence of 4 major peaks within the excitonic luminescence band. They are located at energies of about 1.596 eV, 1.594 eV, 1.591 eV and 1.586 eV at 5K [5]. In pc-CdTe the excitonic transition band is often observed as well, but due to the high bandwidth of the bands in the polycrystalline material, single peaks are difficult to observe. In measurements of Consonni et al. [3] on close-space-sublimation grown (CSS) pc-CdTe, the

characteristic 4 peaks of the excitonic luminescence region can be seen at similar energetic positions as in the single crystalline material. They are attributed to the free exciton at 1.596 eV, a donor-bound exciton at 1.593 eV and excitons at 1.590 eV and 1.587 eV which are assumed to be bound to acceptor complexes such as  $(V_{\text{Cd}}-D_{\text{Te}})$  [6] or  $(V_{\text{Cd}}-2D)$  [7], where D is a donor atom such as chlorine which is discussed in [8].

As the PL-spectra of the excitonic band of the heat-treated samples are not resolved very well [9], PLE measurements are performed in order (i) to gain a better resolution of transitions in the respective energetic region and (ii) to yield information about the recombination paths of certain transitions. In figure 1, the PLE spectrum of the heat-treated sample is shown for different detection energies  $E_{\text{det}}$  at temperatures of 5K. The detection energies were chosen in order to gain information on the recombination behavior of the most prominent peaks in pc-CdTe which are located at about 1.43 eV and between 1.55 and 1.56 eV. Additionally, the detection energy was matched to the bound exciton transition at 1.587 eV. The spectra show peaks and dips, in which peaks mean, that an excited state recombines via a defect which is supposed to be located at the detection energy and a dip means that the excited state has a different relaxation path. For all detection energies, the spectra look similar except for the spectrum which was observed with a detection energy of 1.587 eV. For that detection energy, a small peak can be seen at 1.596 eV and 1.605 eV, where the free exciton



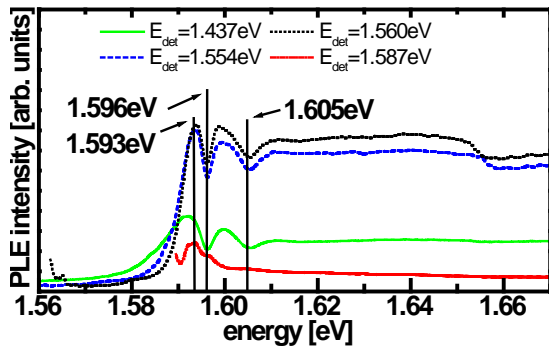


Fig. 1: PLE measurements on the heat-treated sample with different detection energies  $E_{\text{det}}$ .

and the band to band transition are expected to be located. For those excitation energies the spectra for the other detection energies show dips. All spectra show peaks at an excitation energy of 1.593 eV. For detection energies of 1.554 and 1.560 eV, however, a dip is observed at 1.655 eV excitation energy, which cannot be explained here.

A comparison of the PLE spectra for the same detection energies of 1.554 eV, 1.560 eV and 1.587 eV is shown in figure 2 for a HCl-activated sample, which confirms the observations on the heat-treated sample. The PLE spectrum of the HCl treated sample represents all other chlorine-treated samples which look almost identical. Dips appear quite clearly at excitation energies of 1.596 eV and 1.605 eV for detection energies of 1.554 eV and 1.560 eV and small peaks appear instead at a detection energy of 1.587 eV. The shoulders which can be seen in the high energetic edge of the excitonic band PL definitely correspond to transitions. It is remarkable, that there are no peaks visible at an excitation energy of 1.591 eV, although at this energetic position the PL had the most prominent signal. As the defect density in the crystal lattice is smaller than the number of free excitons which are generated by the laser excitation

it must be very improbable to observe the respective bound excitons by PLE spectroscopy here.

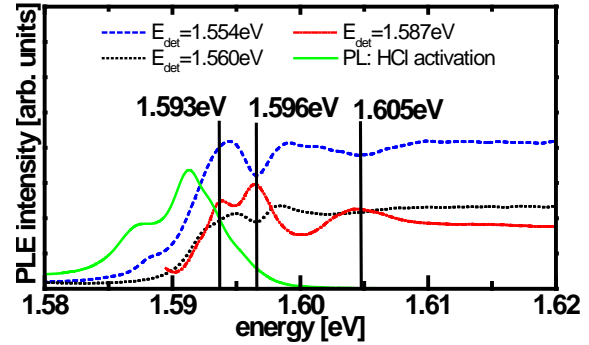


Fig. 2 PLE measurements on the HCl-treated sample with different detection energies  $E_{\text{det}}$ .

This work is supported by the Bundesministerium für Umwelt, Naturschutz und Reaktorsicherheit (BMU).

## References

- [1] M.A. Hernandez-Fenollosa, D.P. Halliday, K. Durose, M.D. Campo, J. Beier, Thin Solid Films 431-432(2002)176.
- [2] M. Köntges, PhD Thesis, Universität Oldenburg, Germany, 2002.
- [3] V. Consonni, G. Feuillet, S. Renet, Journ. App. Phys. 99(2006)053502.
- [4] J.R. Haynes, Phys. Rev. Lett. 4 (1960) 361.
- [5] P. Horodysky, R. Grill, P.Hlidek, Phys. Stat. Sol. (b) 243(2006)2882.
- [6] S. Seto, A. Tanaka, Y. Masa, S. Dairaku, M. Kawashima, Appl. Phys. Lett. 53(1988)1524.
- [7] H.Y. Shin, C.Y. Sun Mat. Sci. Eng. B52(1998)78.
- [8] V. Consonni, G. Feuillet, Journ. Appl. Phys. 105(2009)083535.
- [9] C. Kraft, H. Metzner, M. Hädrich, U. Reislöhner, P. Schley, G. Gobsch, R. Goldhahn, Journ. Appl. Phys. 108(2010)124503.

# Electrical behaviour of CIS solar cells under spectral illumination

S. Schönherr, M. Oertel, U. Reislöhner and H. Metzner

With regard to an application as bottom-cell of tandem solar cells, the behaviour of CIS cells produced in our laboratory were analysed under spectral illumination.

The pure  $\text{CuInSe}_2$  absorbers were produced in a sequential process by reactive annealing of sputtered Cu/In-alloys. The CdS-buffers (50 nm) were deposited onto the absorber in a chemical-bath deposition. To complete the cells, a 75 nm i-ZnO layer and a 300 nm ZnO:Al layer were deposited by magnetron RF-sputtering, and Mo/Cu-grids were added for better carrier collection.

The efficiency of  $\text{CuInSe}_2$  (CIS) thin-film solar cells is often reduced by a current-inhibiting secondary barrier in the energy bands. A positive conduction-band offset between compensated CdS, most commonly used as buffer layer, and hence the CIS absorber limits the fill-factor. The effect is particularly pronounced when high energy photons are removed from the spectrum, and was hence termed “red kink”. Previous work analysed this phenomenon in detail in CIGS solar cells with different Ga-concentrations [1, 2].

For CdS/CIS solar-cells, and for modest Ga-concentration CdS/CIGS, the conduction-band offset ( $\Delta E_c$ ) between CdS and the CIS (or CIGS) absorber is positive. The dashed line in figure 1 shows the conduction-band at thermal equilibrium. The positive offset between the buffer and absorber, often referred to as a “spike”, forms a secondary barrier that may inhibit electron transport, especially when the cell is in forward bias. In many cases, n-type buffer layers such as CdS have a significant concentration of acceptor traps and are therefore heavily compensated. In general, ac-

ceptor traps will have a much smaller electron-capture cross-section when neutral than hole-capture cross-section when negatively ionized. This asymmetry leads to the phenomenon of photo-doping, in which electron-hole pairs that are photo-generated in the buffer push the acceptor traps towards neutrality, and hence the buffer layer towards a more positive charge [1, 2]. The effect on the band diagram (solid line in figure 1) is a downward shift in the conduction-band and a reduced barrier to electron transport. Depending on band gaps of absorber and buffer, large spikes  $\geq 0.5$  eV are possible and carriers may be blocked even with photo-doping.

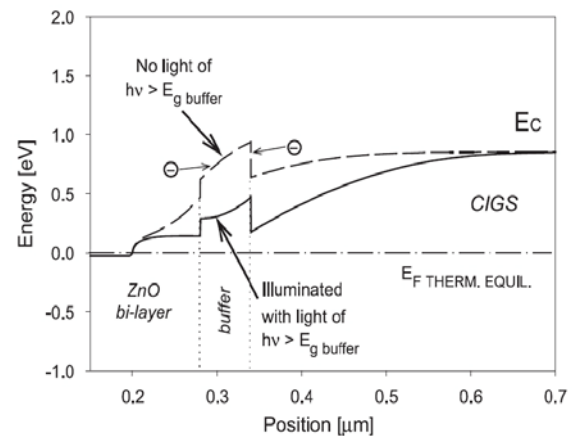


Fig. 1. Conduction-band of a ZnO/CdS/CIGS structure when the buffer is either compensated or n-doped due to light absorption. [1]

Current-voltage measurements under dark, red and white light conditions are illustrated in figure 2. The curve becomes distorted when only light with long wavelengths was used.

The curve under red illumination (dashed line) has three regions: (1) a reverse region with well behaved collection, (2) a mid-bias transition region, and (3) a high-bias region

where the red curve coincides with the dark curve (no collection).

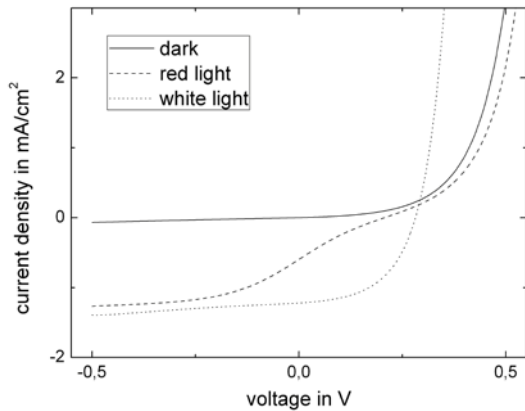


Fig. 2. Dark-red-white J-V curves from a CIS solar cell at room temperature.

With regard to tandem cells, the photo-doping in our CIS solar cells was characterised with different intensities of blue light (420 nm). The “red kink” was generated using red LEDs and subsequently the cell was illuminated additionally with blue LEDs. An array of  $5 \times 3$  LEDs operates with currents between 0 and 70 mA. Figure 3 shows the dependence on the blue light intensity. Even with minimal illumination, the photo-doping was induced and does not change significantly under higher intensity.

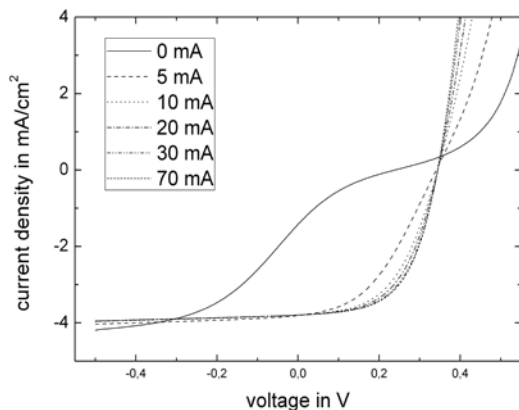


Fig. 3. Dependence on blue light intensity (current flow across a LED-array) with red bias light at room temperature.

In order to analyse the stability of the photo-doping a series of red light J-V

curves was measured as a function of time after white light exposure (figure 4). Without the high-energy photons, the fill factor decreases with time and the exponential slope shifts to progressively higher forward voltage. It took several days until the curve returned to its initial shape with the strongest kink.

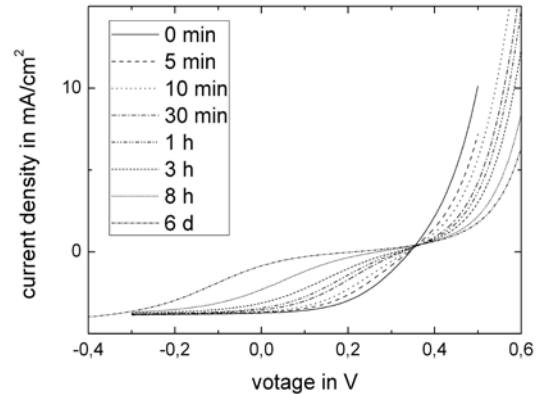


Fig. 4. Disappearance of the red kink for CIS solar cells with blue light exposure at room temperature.

In conclusion, the conduction-band offset model for distortions in the current-voltage curves have been extended to the offsets between CIS and CdS buffer layer. The CIS/CdS system forms a large positive offset and produces a kink-shaped J-V curve. The red-kink could be reduced by an illumination with high-energy photons. The resulting photo-doping is already induced by a minor intensity and shows a stable behaviour over many hours at room temperature. If the design of the tandem top-cell admits the transmission of at least a minor intensity of high-energy photons, then also a bottom-cell based on CdS/CIS can be employed.

## References

- [1] A. O. Pudov, J. R. Sites, M. A. Contreras, T. Nakada and H.-W. Schock, *Thin Solid Films* 480-481 (2005) 273-278
- [2] I. L. Eisgruber, J. E. Granata, J. R. Sites, J. Hou and J. Kessler, *Solar Energy Materials and Solar Cells* 53 (1998) 367-377

## Thermal admittance spectroscopy on Cu(In,Ga)(Se,S)<sub>2</sub>-based solar cells

U. Reislöhner, H. Metzner, C. Ronning

Thin-film solar cells based on Cu(In,Ga)(Se,S)<sub>2</sub>-absorbers (CIGS) are already industrially produced on a high level of quality. High conversion efficiencies are not only achieved on usual glass substrates. The mass production of flexible modules on metal or polymer foils has started (see e.g. www.globalsolar.com). These light-weight modules are especially suitable for flat rooftops, which are typical in sunny regions, and thereby establish a huge market. Due to rising production capacities and promising non-vacuum processes like chemical deposition or printing techniques a further cost reduction is expected.

But contrary to the great success in production there is a peculiar lack of comprehension concerning basic electrical spectroscopy of band-gap levels in this material system. A prominent example is the so called N1-defect observed by capacitance based methods like thermal admittance spectroscopy (TAS) and DLTS. It has been controversially discussed for longer than a decade [1] due to its unusual properties: e.g. a curved Arrhenius representation, and a continuous and distinct shift of its band-gap level after moderate annealing. A typical result of TAS measurements on CIGS-cells is shown in Fig. 1. The measurements were performed in the dark at 0 V bias and  $V_{ac} = 50$  mV. The standard TAS-evaluation of the large conductance peaks between 55 K and 200 K yields the curved Arrhenius-plot (Fig. 2a). By evaluating the slope, regardless of the nonlinear behavior, we get activation energies between 29 and

50 meV. However, the TAS-measurements extend to temperatures well below 200K and thereby overlap with the temperature domain where charge carrier transport by variable range hopping (VRH) was reported [2] to occur in the absorber.

In the standard evaluation of TAS-spectra, only a dependence of the measured emission rate  $e_p = 1/\tau_e$  on trap properties is as-

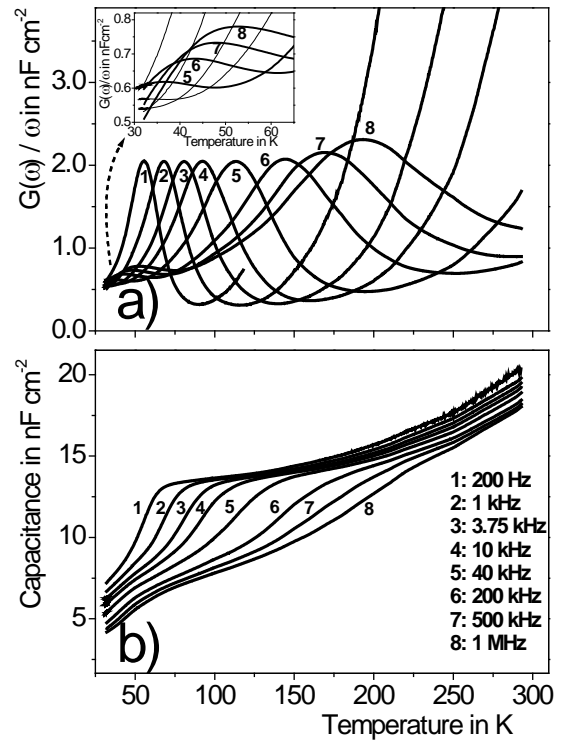


Fig. 1 Conductance (a) and capacitance spectra (b) of a CIGS thin-film solar cell as a function of temperature and frequency. For clarity reasons only eight out of 32 measured curves are displayed.

sumed. This assumption presupposes a sufficiently fast transport of carriers which is not expected in the case of hopping conduction.

The characteristic carrier transport time  $\tau$  is proportional to the inverse of the diffusion constant  $D$  which shows the temperature dependence  $D \sim T^{-1/2} \exp(-B/T^{1/4})$  [3] in the case of variable range hopping. When hopping conduction prevails, the diffusivity of majority carriers decreases strongly with decreasing temperature and the carriers can follow the ac-signal without phase shift on-

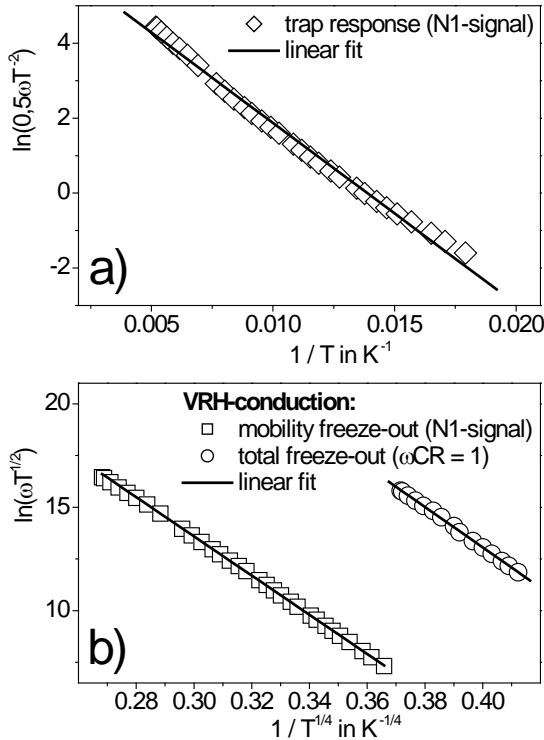


Fig. 2 (a) Standard evaluation of the trap response obtained from Fig. 1a gives the known curved line. (b) The evaluation in terms of mobility freeze-out under VRH-conduction shows a clear linear behavior. Only  $G(\omega)$ -maxima below 150 K were used for the linear fit, to avoid the influence of a transition region in the conduction mechanism. The evaluation of total freeze-out ( $\omega CR = 1$ ) for  $G(\omega)$ -peaks at  $T < 55$  K (see inset in Fig. 1a) according to VRH-conduction gives a parallel line (for details see reference [3]).

ly up to a limiting frequency of  $\omega \approx \tau^{-1} \sim D$ . By further lowering the temperature, the measured capacitance is reduced and a step in  $C(T)$  appears (corresponding to a peak in  $G$ ) as a function of frequency, even when the basic condition  $\omega CR < 1$  is fulfilled. This mobility freeze-out effect is a third, hi-

therto not recognized source for a TAS-signal beside trap response and carrier freeze-out. Faster carrier emission processes which may take place cannot be observed under this condition and the measured apparent emission rate  $e_p$  is approximately given by  $e_p \propto D$ . Thus, we replace the usual Arrhenius evaluation  $\ln(1/2\omega T^{-2})$  vs.  $T^{-1}$  by plotting  $\ln(\omega T^{1/2})$  vs.  $T^{-1/4}$  and the result is a straight line as shown in Fig. 2b. From the slope we get the density of states  $N_{EF}$  (per unit energy) around the Fermi energy which is in perfect agreement with data of Schmitt et al. [2] who obtained  $N_{EF} = 2.4 \times 10^{18} \text{ eV}^{-1} \text{ cm}^{-3}$  by dc-conduction measurements on CIGS-films.

In summary, a too small carrier mobility, which is expected in case of hopping conduction, inhibits the observation of carrier capture and emission at traps by thermal admittance spectroscopy. Then, the admittance signal displays the freezing-out of majority carrier mobility instead of trap response. As shown, intricate interpretations concerning the origin of the N1-signal in CIGS and the reason for its curved Arrhenius representation become redundant accepting the transition to variable-range hopping conduction at low temperatures and its implications to the TAS measurement process. The results were published in more detail in reference [3].

We thank Dr. Palm and Dr. Dalibor of AVANCIS GmbH & Co. KG for interesting discussions and providing the samples.

## References

- [1] M. Igalson, A. Urbaniak, and M. Edoff, Thin Solid Films 517, 2153 (2009).
- [2] M. Schmitt, U. Rau, and J. Parisi, Phys. Rev. B 61, 16052 (2000).
- [3] U. Reislöhner, H. Metzner, C. Ronning, Phys. Rev. Lett. 104, 226403 (2010).

# Interface modification by ion implantation in Cu(In,Ga)Se<sub>2</sub> solar cells

M. Teichmann, J. Haarstrich, T. Rissom\*, H. Metzner

\*Helmholtz Zentrum Berlin für Materialien und Energie, Solar Energy Research, Institute for Technology, Lise-Meitner-Campus, Hahn-Meitner-Platz 1, 14109 Berlin

The standard device structure of current high-efficiency solar cells based on Cu(In,Ga)Se<sub>2</sub> (CIGS) absorber layers include a chemical-bath-deposited (CBD) CdS buffer layer between the CIGS absorber layer and the transparent ZnO front-electrode. However, because of environmental and technical reasons, there have been intensive efforts to replace the CBD-CdS buffer. The substance is carcinogenic, moreover the interruption of the vacuum processes and the usage of large area liquids for CBD cause problems in production. Additionally, the absorption of the CdS layer ( $E_{\text{gap}} \approx 2,4\text{eV}$ ) limits the short circuit current of the solar cells.

The main function of the buffer layer is the formation of an interface with a low recombination velocity. It has been shown that the interface recombination can be minimized if the Fermi level is close to the conduction band of the absorber [1]. Numerical simulations confirm that it may be possible to omit the CdS buffer if a successful inversion of the surface is realised [2].

Low-energy ion implantation were performed in order to achieve a well-defined doping profile that inverts the surface layer. The profile has been calculated by SRIM-calculation (Stopping and Range of Ions in Matter [3]) and was confirmed by SIMS measurements (secondary ion mass spectroscopy). Cadmium was chosen as a possible n-type dopant in CIGS [4]. Ion implantation is accompanied by defect creation. Therefore, a thermal treatment is necessary in order to restore the lattice and to activate the dopant. Thus, implantations were carried out with xenon ions, which were chosen because xenon presumably causes a comparable number and distribution of defects due to the similar atomic mass without inducing doping effects. This offers the possibility to analyze the annealing of the implantation defects only. Afterwards, the

implanted absorber layers were annealed at various temperatures up to 500°C in argon-atmosphere without dwell time as well as in vacuum ( $p \approx 3\text{mbar}$ ) with dwell time (30 minutes). Finally, solar cells with CdS buffer layer were fabricated and characterized

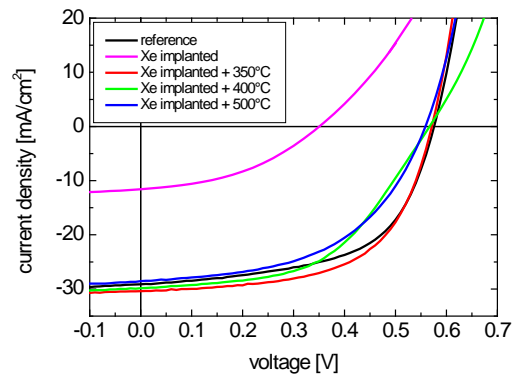


Fig. 1 j-V characteristics of a typical reference sample and a sample fabricated from Xe implanted absorbers before and after annealing without dwell time at different temperatures with CdS buffer layer.

electrically.

Figure 1 shows the j-V characteristics for solar cells made from reference and xenon-implanted samples. The reference yields an efficiency of about 10%. The implanted absorbers show a strong degradation in  $V_{\text{OC}}$  together with  $j_{\text{SC}}$  which can be already recovered by annealing in Ar-atmosphere for the lowest temperature shown. Further increase of the annealing temperature initially reduces the fill factor. This can be ascribed to a degradation of the material that also occurs after annealing of unimplanted samples (not shown). A full recovery of the solar cell parameters is also achieved by heat-treatment in vacuum at 300°C (not shown). For a beneficial doping, cadmium must not diffuse into the bulk material due to the heat-treatment. Before and after the annealing step, cadmium depth profiles were measured using SIMS. These samples were annealed in inert gas atmosphere at 200 and 300°C with a dwell time of 30 minutes.



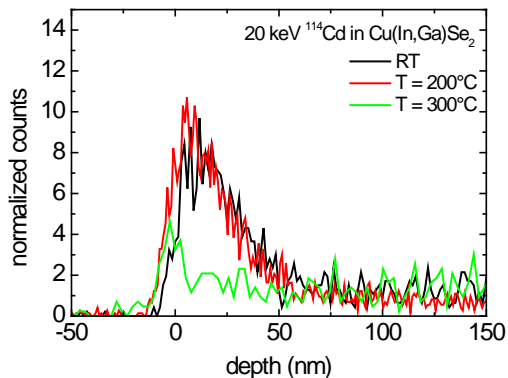


Fig. 2 Depth profiles of  $^{114}\text{Cd}$  implanted in CIGS absorbers with a fluence of  $1.4 \times 10^{15} \text{ cm}^{-2}$  and an energy of 20keV before and after annealing in inert gas atmosphere.

Figure 2 shows the SIMS data indicating no change in cadmium depth profile after annealing at 200°C. But a strong decrease of the signal is observed after annealing at 300°C. This indicates an increasing diffusion of cadmium at this temperature.

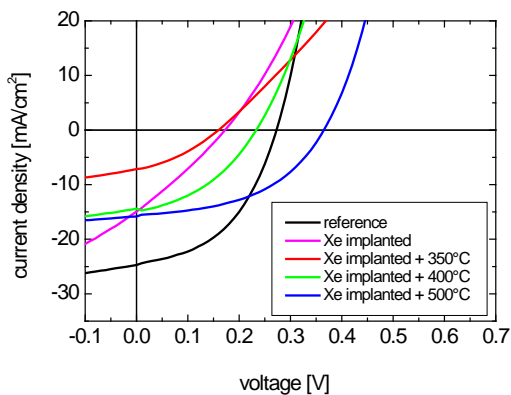


Fig. 3 j-V characteristics of a typical reference sample and a sample fabricated from Cd implanted absorbers before and after annealing in Ar at different temperatures without CdS buffer layer.

The same annealing processes as for xenon implanted samples were performed on cadmium implanted absorbers. After the heat-treatment those absorbers were processed without CdS buffer layer in order to investigate the effect of surface inversion. To this end, the transparent ZnO front-electrode is directly sputtered onto the implanted absorber. Figure 3 and 4 show the j-V characteristics of the solar cells made

from implanted absorbers. In comparison to cells with CdS,  $V_{OC}$  and  $j_{sc}$  of the reference is considerably reduced. Further degradation occurs through implantation. As a consequence of the heating without dwell time, a progressive increase of the fill factor is

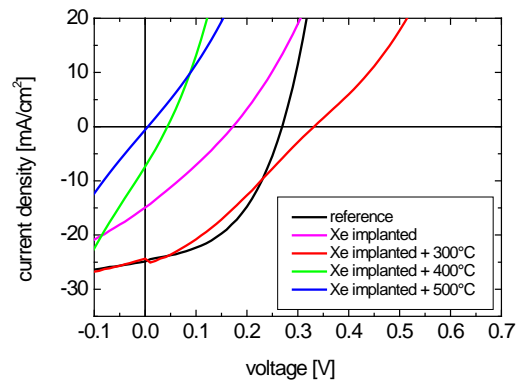


Fig. 4 j-V characteristics of a typical reference sample and a sample fabricated from Cd implanted absorbers before and after annealing in vacuum at different temperatures without CdS buffer layer.

visible (Fig.3). Furthermore, higher open-circuit voltages are measured after annealing at 500°C. Figure 4 illustrates the dependence of j-V-characteristics on the temperature when annealing with dwell time. For the lowest temperature, a healing of defects is also detectable. But for rising temperature, the solar cell parameters become worse. This behavior can be explained by a stronger diffusion of cadmium due to the longer annealing procedure.

In summary, a successful annealing procedure after ion implantation is described. The investigation of solar cells without CdS buffer layer revealed that n-doping of a thin surface layer is hampered due to an increasing diffusion of the dopant.

This work was supported by the BMU under the contract number 0327665B/D/E.

## References

- [1] R. Klenk, Thin Solid Films 387 (2001), 135.
- [2] J. Haarstrich et al., Thin Solid Films, in press, <http://dx.doi.org/10.1016/j.tsf.2010.12.090>
- [3] J. F. Ziegler et al., Pergamon Press, New York, 2003.
- [4] P. Migliorato et al., Journal of Applied Physics 46 (1975), 1777.

### 3. Technical reports and equipment

#### Operation of the Ion-accelerator JULIA and the Ion-implanter ROMEO

U. Barth, F. Jehn, G. Lenk, W. Wesch, C. Ronning

The 3 MV high current tandemron accelerator **JULIA** (Jena University Laboratory for Ion Acceleration) went in operation end of 1996. Since the beginning of the routine-operation in 1997 it has been used for different types of experiments requiring a broad spectrum of ion-beams. With the exception of helium, where the duoplasmatron ion-source followed by a lithium exchange channel was used, all ions were extracted from a sputter-type ion-source. The beam-on-target-time of 1273 h was about 20% lower than in 2009. The 400 kV ion-accelerator **ROMEO** is in routine operation since 1998, here the beam-on-target-time of 1260 h was in the same order of magnitude as in the preceding years.

Both accelerators can be operated separately or in combination. The ion-beams produced until 2010 are summarized in table 1. The ion-beam currents quoted are typical values of the ion source currents used for the experiments, the maximum currents available are significantly higher for most ions.

Period	Element	Julia	Romeo
1	Hydrogen (H)	5 $\mu$ A	4 $\mu$ A
	Helium (He)	0,2 $\mu$ A	4 $\mu$ A
2	Lithium (Li)	2 $\mu$ A	1 $\mu$ A
	Boron (B)	0,2 $\mu$ A	5 $\mu$ A
	Carbon (C)	9 $\mu$ A	1 $\mu$ A
	Nitrogen (N)	10 $\mu$ A	4 $\mu$ A
	Oxygen (O)	17 $\mu$ A	2 $\mu$ A
	Flourine (F)	-	2 $\mu$ A
3	Neon (Ne)	-	5 $\mu$ A
	Sodium (Na)	-	6 $\mu$ A
	Magnesium (Mg)	-	5 $\mu$ A
	Aluminium (Al)	-	4 $\mu$ A
	Silicon (Si)	16 $\mu$ A	4 $\mu$ A
	Phosphorus (P)	-	4 $\mu$ A
	Chlorine (Cl)	-	2 $\mu$ A
	Argon (Ar)	-	20 $\mu$ A

Table 1. Ion-beams accelerated during 2010. The currents given are measured at the Q-Snout-Faraday-cup after the low-energy mass separator (JULIA) and at the target position (ROMEO), respectively.

Period	Element	Julia	Romeo	
4	Potassium (K)	-	3 $\mu$ A	
	Calcium (Ca)	-	5 $\mu$ A	
	Titanium (Ti)	0,7 $\mu$ A	-	
	Vanadium (V)	0,2 $\mu$ A	1 $\mu$ A	
	Manganese (Mn)	0,017 $\mu$ A	5 $\mu$ A	
	Chromium (Cr)	0,2 $\mu$ A	3 $\mu$ A	
	Iron (Fe)	0,8 $\mu$ A	2 $\mu$ A	
	Cobalt (Co)	-	3 $\mu$ A	
	Nickel (Ni)	-	6 $\mu$ A	
	Copper (Cu)	0,5 $\mu$ A	-	
	Zinc (Zn)	1 $\mu$ A	6 $\mu$ A	
	Gallium (Ga)	1 $\mu$ A	3 $\mu$ A	
	Germanium (Ge)	1,6 $\mu$ A	4 $\mu$ A	
	Arsenic (As)	0,4 $\mu$ A	1 $\mu$ A	
	Selenium (Se)	0,5 $\mu$ A	1,5 $\mu$ A	
	Bromine (Br)	19 $\mu$ A	8 $\mu$ A	
	Krypton (Kr)	-	10 $\mu$ A	
	5	Rubidium (Rb)	0,075 $\mu$ A	1 $\mu$ A
		Strontium (Sr)	-	3 $\mu$ A
Yttrium (Y)		-	4 $\mu$ A	
Zirconium (Zr)		0,3 $\mu$ A	1,5 $\mu$ A	
Rhodium (Rh)		0,2 $\mu$ A	-	
Palladium (Pd)		0,095 $\mu$ A	1 $\mu$ A	
Silver (Ag)		1,6 $\mu$ A	10 $\mu$ A	
Cadmium (Cd)		-	0,8 $\mu$ A	
Indium (In)		5 $\mu$ A	8 $\mu$ A	
Tin (Sn)		-	3 $\mu$ A	
Antimony (Sb)		0,6 $\mu$ A	4 $\mu$ A	
Tellurium (Te)		-	2 $\mu$ A	
Iodine (I)		3 $\mu$ A	-	
Xenon (Xe)		-	10 $\mu$ A	
6	Caesium (Cs)	-	4 $\mu$ A	
	Barium (Ba)	-	1 $\mu$ A	
	Praseodymium (Pr)	-	1 $\mu$ A	
	Neodymium (Nd)	-	0,5 $\mu$ A	
	Samarium (Sm)	0,01 $\mu$ A	1,5 $\mu$ A	
	Europium (Eu)	0,035 $\mu$ A	2 $\mu$ A	
	Gadolinium (Gd)	0,03 $\mu$ A	-	
	Terbium (Tb)	-	3 $\mu$ A	
	Erbium (Er)	0,04 $\mu$ A	2 $\mu$ A	
	Tantalum (Ta)	0,2 $\mu$ A	2 $\mu$ A	
	Tungsten (W)	0,3 $\mu$ A	0,01 $\mu$ A	
	Osmium (Os)	0,05 $\mu$ A	-	
	Iridium (Ir)	0,3 $\mu$ A	6 $\mu$ A	
	Platinum (Pt)	0,2 $\mu$ A	-	
	Gold (Au)	24 $\mu$ A	20 $\mu$ A	
	Lead (Pb)	0,035 $\mu$ A	15 $\mu$ A	
	Bismuth (Bi)	-	3 $\mu$ A	

As in the preceding years the ion-beam facility was used by external research groups:

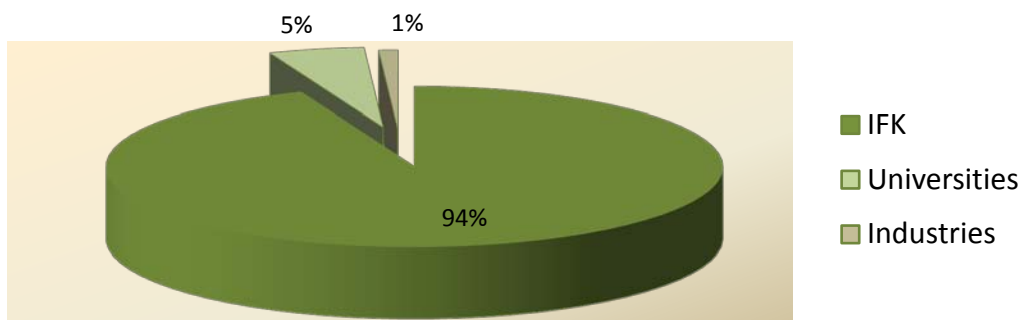
### 3MV-Tandetron „JULIA”

University Jena  
University Stuttgart (Frau Guilliard)  
IPHT Jena (Dr. Diegel)  
Firma Layertec (Herr Heyer)

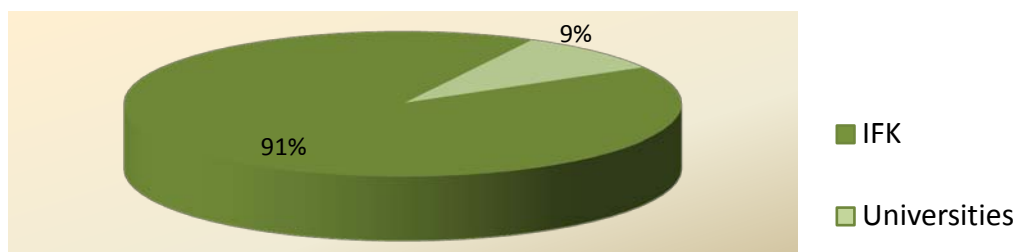
### 400kV Implanter „ROMEO“

University Jena  
University Ilmenau (Prof. Schaaf)  
University of Pretoria (Prof. Malherbe)  
University of Pretoria (Prof. Friedland)  
University of Pretoria (Dr. Theron)  
University Minsk (Prof. Kamerow)

### 3 MeV-Tandetron "JULIA"



### 400 kV Implanter "ROMEO"



## Cryogenic Services 2010-TTS

All in-house customers of cryogenic liquids, which are all faculties of natural sciences, the medical division of the university, including several hospitals, and other external scientific institutes (e.g. Institute for Photonic Technology Jena, , Leibnitz Institute Hans-Knöll Jena) as well as some private customers like the Innovent e.V. Jena or some medical practices were provided with liquid helium (LHe), high purity gases (He, N<sub>2</sub>) and with liquid nitrogen (LN<sub>2</sub>) by the Cryogenic Services. Roughly 74.000 litres of LN<sub>2</sub> were delivered by the cryogenic services this year.

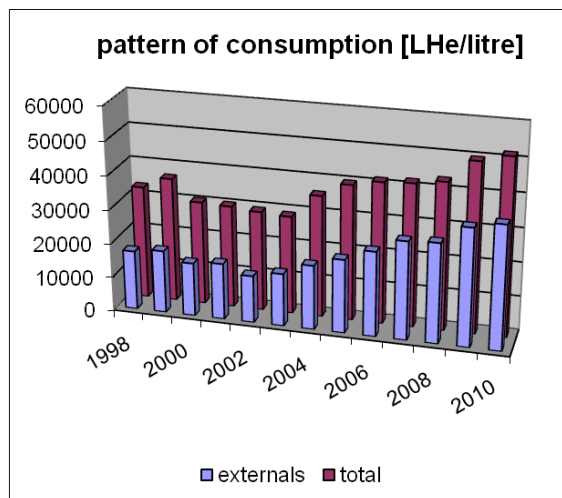


Fig. 1.: Liquid helium output

As illustrated in Figure 1, the production of LHe has levelled off in the recent two years. Roughly 43.00 litres of LHe were delivered which calls for an annual gross refrigeration value of 51.000 litres. That is the highest amount ever produced in the history of the Cryogenic Services Department. In the period under report our focus was on stabilizing the ongoing helium liquefaction by performance-enhancing some circumferential sup-processes like high-pressure storage and the carriage conditions of both the LHe-delivery and the return of it as a gas in portable high-pressure storage vessels. The following sub-steps of the reconstruction were all accomplished on time:

- disassembling of the existing installation of one of the three high-pressure compressors
- workings on the building structure like basement and the ground floor
- rearrangement of the existing piping
- insertion of the new 30m<sup>3</sup>/h high-pressure compressor (centrepiece in Fig.2)
- rebuilding of the electrical installation

- erection of a emergency shut-down
- adjustment of the automatic process-oriented sequential control to implement the new components
- extension of the high-pressure storage capacity by a 1.2 m<sup>3</sup>-300bar storage
- reconstruction of the refuel-area according to the legal requirements of the German Technical Inspection Authority
- extension of the driving surface at the street level entry in order to create a wide doorway for larger LN<sub>2</sub>-trucks Fig.3

During the whole reconstruction period the stuff managed ongoing refrigeration operations without any breakdown of the LHe –delivery. In the past the snowmelt had drained on the cargo area of the TTS. Hence the loading area went slippery or icy sometimes. The loading of cargo in danger of tipping has been secured considerably by installing roof gutters on the gasholder.



Fig.2: High-pressure compressors



Fig.3: Enlargement of the doorway

The TTS-staff executed design, installation control and commissioning of the pure nitrogen equipment at the Helmholtzweg 4 site and the Steiger site as well as the rebuilding of the utilities supplies in the extension of the Helmholtzweg 5 building.

## Equipment

### Preparation of thin films and devices

- HV evaporation facilities for thermal evaporation and rf-sputtering with oxidation system
- UHV evaporation facilities, including electron gun and in situ RHEED system
- Equipment for laser deposition of thin films and material systems, especially high temperature superconductors (KrF excimer laser,  $\lambda = 248$  nm)
- Molecular Beam Epitaxy (MBE) facilities: MBE for silicon carbide (RIBER EVA 32 R&D)
- Organic Molecular Beam Epitaxy (OMBE) facilities including surface analysis techniques and *in situ* optical spectroscopy (PL and DRS)
- dc and ac sputtering systems for thin films and multilayers
- Ion beam etching with Ar ions at sample temperatures down to 80 K
- Reactive ion beam etching with sample diameters up to 6 cm
- Ultrasonic wire bonder
- Equipment for photolithographic patterning

### Surface analysis systems

- AUGER electron spectrometer
- Surface analysis system UNISPEC with XPS, UPS, AES, LEED, STM
- Atomic force microscopes (AFM and Microstructure Measuring Device VERITEKT 3 with needle sensor)
- Surface profilometer DEKTAK 100
- Scanning electron microscopes
- Several UHV-Scanning probe devices (STM, AFM)

### Electrical measurement techniques

- Electrical transport measurements (resistance, critical current density, point contact and tunneling spectroscopy)
- Hall-effect and Four-point probe equipment
- Current-voltage characteristics ( $2\text{ K} < T < 300\text{ K}$ ,  $B \leq 5\text{ T}$ )
- Current-voltage characteristics by microwave irradiation ( $2\text{ GHz} < f < 300\text{ GHz}$ )
- Noise measurements (frequency range  $60\ \mu\text{Hz} - 100\text{ kHz}$ ) at low temperatures
- LTS-SQUID characterization at 4.2 K (current-voltage, flux-voltage, noise, screening properties)
- HTS-SQUID characterization up to 100 K (current-voltage, flux-voltage, noise)
- 2 Deep level transient fourier spectrometers (temperature range 80 K - 690 K, 30 K - 330 K)
- 3 Admittance spectrometers (frequency range 40 Hz - 100 kHz, 20 Hz - 1 MHz and 75 kHz - 30 MHz, temperature range 30 K - 690 K)
- Microwave signal generator (frequency range 1 - 20 GHz, resolution: 1 kHz)
- Electrical and optical characterization of high power diode laser arrays

### **Equipment for optical characterization**

- UV-VIS spectrometer
- FTIR spectrometer
- Cathodoluminescence at SEM, equipped from IR - UV
- Micro-Photoluminescence, IR-UV, time-resolution ~ 1ns
- Photoluminescence excitation (PLE)
- Optical microscopes

### **Equipment for thermal treatment**

- Furnace for conventional thermal treatment in inert gas atmosphere or vacuum (temperatures up to 2050 K)
- RTA apparatus (double graphite strip heater) for short time annealing (annealing time in the order of seconds, temperature range 1000 K to 1950 K, temperature rise rate 100 K s<sup>-1</sup>)

### **Ion beam techniques**

#### 3 MV Tandatron accelerator "JULIA", equipped with

- Sputter ion source and Duoplasmatron source
- Universal beam line for ion implantation and ion beam analysis
- Second beam line for ion beam analysis, combined with implantation chamber of 400 kV implanter
- Irradiation chamber with cooled and heated sample holder and four axis goniometer

#### *Application:*

- Ion implantation: energy range 500 keV - 12 MeV, temperature range 15 K - 1500 K
- Ion beam analysis: RBS and PIXE in combination with channeling, ERDA

#### 400 kV implanter "ROMEO", equipped with

- Hot filament, hollow cathode ion source
- Irradiation chamber with cooled and heated sample holder and four axis goniometer, combined with beam line of 3 MV Tandatron accelerator

#### *Application:*

- Ion implantation: energy range 20 keV - 400 keV, temperature range 15 K - 1500 K
- Ion implantation at low temperatures and subsequent RBS analysis using H- or He-ions from 3 MV Tandatron accelerator

#### Low Energy implanter "LEILA", equipped with

- Colutron Ion source 100-Q
- Colutron Ion Gun System G-2-D
- Irradiation chamber with heated sample holder

#### *Application:*

- Irradiation of surfaces: energy range sub-keV, temperature range 300 K - 750 K



Low Energy implanter “Mr. JIM Stringer”, equipped with

- Hot filament, hollow cathode ion source
- Irradiation and deposition chamber

*Application:*

- Deposition of diamond-like thin films: energy range 100eV – 30 keV, RT

Focused Ion Beam system FEI NanoLab Helios 600i

- Liquid ion source, E = 500 eV – 30 keV
- Electron microscope, E = 350 eV – 30 keV

*Application:*

- TEM-lamella preparation, etc.

**Low temperature measuring equipment**

- He-4 cryostats for temperatures down to 4.2 K
- He-4 refrigerator for the temperature range 1.3 K - 4.2 K
- He-3 cryostat for temperatures down to 300 mK
- He-3/He-4 dilution refrigerator with a base temperature of 35 mK
- He-3/He-4 dilution refrigerator with a base temperature of 7 mK
- Electronic equipment for characterization of cryoelectronic devices
- SQUID sensor systems for magnetic measurements under unshielded conditions
- SQUID sensor system for spatially resolved magnetorelaxometry
- Cryostats ( $2\text{ K} < T < 300\text{ K}$ ; optical window; magnetic field)
- Cryocoolers (Gifford-McMahon and Stirling)
- Pulse tube refrigerators (for sensor cooling)

**CIS-LAB**

- MBE system NEBULA for  $\text{Cu}(\text{In,Ga})\text{S}_2$  layers on 4” substrates including RHEED setup
- Two HV systems for closed-space sublimation (CSS)
- Solar simulator (AM 1.5) with Current-Voltage measurement
- RF reactive sputtering system for transparent conducting oxides (TCO’s) and molybdenum
- DC sputtering system for copper and indium
- UHV system ULS400 for  $\text{Cu}(\text{In,Ga})(\text{Se,S})_2$  on (100x100) mm<sup>2</sup> substrates
- Scanning electron microscope JEOL JSM-6490 with LaB<sub>6</sub>-cathode
- Quantum efficiency measurements of solar cells
- Wet chemical processing and chemical bath deposition of photoactive layers

**SQUID application laboratories**

- Measurement system for non-destructive evaluation in unshielded environment based on high-T<sub>C</sub>-SQUID gradiometers
- Heart monitoring system for biomagnetic investigation in unshielded environment based on high-T<sub>C</sub>-SQUID gradiometers
- High precision position detection system based on low-T<sub>C</sub>-SQUIDS
- Magnet-Relaxation-Measuring System in unshielded environment based on low-T<sub>C</sub> SQUID gradiometers

**Clean room (number of particles/cu/t < 100)**

- Foto lithography
- Wet chemical etching
- minimum lateral resolution: few micrometers

**Shielded rooms**

- Faraday room
- Magnetic shielded room

**Laboratory for cryogenic measurement of mechanical quality factors of gravitational wave detector components**

- room temperature stability of  $\pm 0.2$  K at best
- vibration isolation (decoupled foundation)
- acoustic isolation
- remote controlled operation of the measurement equipment
- separated room for disturbing machines (e.g. pumps)
- full supply of technical media to perform cryogenic measurements

## 4. Current research projects

**(A) Supported by the Bundesministerium für Bildung, Wissenschaft, Forschung und Technologie (BMBF), Bundesministerium für Wirtschaft und Arbeit (BMWi), and Bundesministerium für Umwelt, Naturschutz und Reaktorsicherheit (BMU)**

*Ioneninduzierte Strukturumbildungs- und Ausheilprozesse in Halbleitern*

Teilprojekt 4 im Verbund „Hochauflösende in-situ-Charakterisierung der Strukturumbildungsprozesse in Halbleitern“

Verbund Forschung mit Sonden und Ionenstrahlen im Gesamtverbund Erforschung der kondensierten Materie mit Großgeräten

Prof. Dr. W. Wesch 05KK7SJ1 07/07 – 12/10

*Ioneninduzierte Strukturumbildungsprozesse in amorphen Halbleitern*

Teilprojekt 4 im Verbundprojekt „Ioneninduzierte Strukturumbildung“

Verbund Forschung mit Sonden und Ionenstrahlen im Gesamtverbund Erforschung der kondensierten Materie mit Großgeräten

Prof. Dr. W. Wesch 05K10SJ1 07/10 – 06/13

*Verbundprojekt: Computational Materials Science gestützte Optimierung des Wirkungsgrades von CIGS-Dünnschichtsolarzellen*

Prof. Dr. W. Wesch 0327665E 07/07 – 05/11

*CdTe-CdS-Solarzellen hoher Effizienz für eine verbesserte Modul-Produktionstechnologie*

Prof. Dr. W. Wesch 0329881A 09/08 – 04/12

*Strahlenschädenbildung und Diffusion energetischer Teilchen in SiC*

Dr. E. Wendler SUA 08/028 03/09 – 12/11

*Forschungsprämie*

Prof. Dr. C. Ronning 03FPB00345 01/10 – 12/10

*Forschungsprämie*

Prof. Dr. C. Ronning 03FPB00384 04/10 – 03/11

*Toxikologische Charakterisierung von Nanomaterialien für die diagnostische Bildgebung in der Medizin – NanoMed*

Prof. Dr. P. Seidel BMBF (Ausschreibung NanoCare) 09/10 – 08/13

**(B) Supported by the Deutsche Forschungsgemeinschaft (DFG)**

*Untersuchung astrophysikalischer Reaktionen in flüssigen Helium-Tröpfchen*

Prof. Dr. Fr. Huisken HU 474/22-1 01/09 – 03/10

*Formation of GEMS from interstellar silicate dust*

Prof. Dr. Fr. Huisken HU 474/23-1 01/10 – 12/10

*Spektroskopische Untersuchungen an polyzyklischen aromatischen Kohlenwasserstoffen mit aliphatischen Seitengruppen*

Prof. Dr. Fr. Huisken HU 474/24-1 02/10 – 12/10

*Synthesis, processing, and spectroscopic characterization of PAHs with astrophysical impact*

Prof. Dr. Fr. Huisken HU 474/21-2 08/10 – 01/12

*Gütemessungen bei kryogenen Temperaturen*

(Teilprojekt C 4 im SFB/TR 7 „Gravitationswellenastronomie“)

Prof. Dr. P. Seidel, Dr. W. Vodel, Prof. A. Tünnermann DFG–SFB/TR7 01/03 – 12/10

*Josephson effects at iron pnictides*

Prof. Dr. P. Seidel DFG (SPP 1458) 05/10 – 04/13

*Ion beam doping of semiconductor nanowires*

Prof. Dr. C. Ronning Ro1198/7-3 (SPP1165) 07/06 – 10/10

*Rastertunnelspektroskopie an einzelnen Molekülen in epitaktischen Nanoschichten*

Prof. Dr. T. Fritz FR 875/11 10/09 – 12/12

*Strukturierungsverfahren für mikro- und nanooptische Elemente in Lithiumniobat*

Dr. E.-B. Kley, Prof. Dr. W. Wesch KL1199/2-2 05/10 – 04/12

*Großgeräte für die Forschung (Mikro-Photolumineszenz Apparatur)*

Prof. Dr. C. Ronning INST 275/242-1 01/10 – 12/10

*Großgeräte für die Forschung (Dual beam – focused ion beam (FIB)system)*

Prof. Dr. C. Ronning INST 275/240-1 01/10 – 12/10

### **(C) Support by the EU**

*Marie-Curie ITN network “Nanowiring”*

Prof. Dr. C. Ronning 265073 11/10 – 10/14

*Bio-Imaging with Smart Functional Nanoparticles (BONSAI)*

6<sup>th</sup> Framework Programme: Specific Targeted Research Projects (STREP)

Prof. Dr. Fr. Huisken European Commission 01/07 – 02/10

### **(D) Supported by the Thüringer Ministerium für Bildung, Wissenschaft und Kultur (TKBWK)**

*Optische und strukturelle Untersuchung ultradünner molekularer Schichten*

Prof. Dr. T. Fritz B 515-10030 09/10 – 12/11

*Ionenstrahlmodifikation und -analyse von Titanoberflächen*

Prof. Dr. W. Wesch 02/9125 IBA Heiligenstadt 05/02 – 12/11

*Dünnschicht Solarzellen der dritten Generation: transparente Dünnschicht Solarzellen / Tandem-Solarzellen II*

Prof. Dr. W. Wesch B 514-09001 12/08 – 05/10

**(E) Supported by other institutions**

<i>Strukturuntersuchungen an dem für die Photovoltaik relevanten Cu(In,Ga)(Se,S)<sub>2</sub> Halbleitersystem mittels Synchrotronstrahlung</i>		
Dr. C.S. Schnohr	Carl-Zeiss-Stiftung	06/10 – 05/12
<i>Experimente zur Labor-Astrophysik</i>		
Prof. Dr. Fr. Huisken	MPI Heidelberg	01/02 – 05/12
<i>Untersuchungen von CIGS-Photovoltaikzellen, hergestellt im Non-Vakuumverfahren</i>		
Prof. Dr. W. Wesch	KF0314502DA6	09/06 – 06/10
<i>Projektbezogener Personenaustausch USA (DAAD)</i>		
Prof. Dr. C. Ronning	D/08/11051	01/09 – 12/10
<i>Phase dynamics of coupled system of Josephson junctions</i>		
Prof. Dr. P. Seidel, Dr. Yu. M. Shukrinov	Heisenberg-Landau Programm	01/10 – 12/10
<i>Personengebundene Förderung - DAAD-Promotionsstudium Boris Ivanov (Russische Förderung)</i>		
Prof. Dr. P. Seidel	DAAD	10/09 – 10/10
<i>Basisuntersuchungen an transkritischen kryogenen Fluiden: Untersuchungen zur Speicherung überkritischen Wasserstoffs</i>		
Prof. Dr. P. Seidel	ILK Dresden	04/10 – 11/10
<i>Zerstörungsfreie Strahldiagnose für Linear- und Ringbeschleuniger</i>		
Prof. Dr. P. Seidel	GSI Darmstadt	01/07 – 06/10
<i>Kryostromkomperator für DESY Hamburg</i>		
Prof. Dr. P. Seidel	DESY Hanburg	01/10 – 06/10

## 5. Publications, invited talks, and conference contributions

### 5.1 Publications in scientific journals

- T. Dienel, A. Krause, R. Alle, R. Forker, K. Meerholz und T. Fritz  
*Alkali metal doped organic molecules on insulators: Charge impact on the optical properties*  
Adv. Mater. **22** (2010) 4064
- A.A. Levin, T. Leisegang, R. Forker, M. Koch, D. C. Meyer und T. Fritz  
*Preparation and crystallographic characterization of crystalline modifications of 3,4:9,10-perylene-tetra-carboxylic dianhydride at room temperature*  
Cryst. Res. Technol. **45** (2010) 439
- C. Wagner, D. Kasemann, C. Golnik, R. Forker, M. Esslinger, K. Müllen und T. Fritz  
*Repulsion between molecules on a metal: Monolayers and submonolayers of hexa-perihexabenzocoronene on Au(111)*  
Phys. Rev. B **81** (2010) 035423
- F.F. Komarov, O.V. Milchanin, L.A. Vlasukova, W. Wesch, A.F. Komarov, A.V. Mudry  
*Ion beam synthesis of InAs nanocrystals in single crystal silicon (in Russian)*  
Izvestija RAN, Seria Fisicheskaya **74** (2010) 323
- M. Katsikini, J. Arvanitidis, S. Ves, E.C. Paloura, E. Wendler, W. Wesch  
*Indium implantation and annealing of GaN: Lattice damage and recovery*  
Phys. Status Solidi **C7** (2010) 36
- H. Hartung, E.-B. Kley, Th. Gischkat, F. Schrempel, W. Wesch, A. Tünnermann  
*Ultra thin high index contrast photonic crystal slabs in lithium niobate*  
Optical Materials **33** (2010) 19
- E. Friedland, N.G. van den Berg, J.B. Malherbe, R.J. Kuhudzaj, A.J. Botha, E. Wendler, W. Wesch  
*Study of iodine diffusion in silicon carbide*  
Nucl. Instr. and Methods B **268** (2010) 2892
- E. Wendler, Th. Bierschenk, W. Wesch, E. Friedland, J.B. Malherbe  
*Temperature dependence of damage formation in Ag ion irradiated 4H-SiC*  
Nucl. Instr. and Methods B **268** (2010) 2996
- K. Gärtner  
*MD simulation of ion implantation damage in AlGaAs: II. Generation of point defects*  
Nucl. Instr. and Methods B **268** (2010) 149
- K. Gärtner, T. Clauß  
*MD simulation of ion implantation damage in AlGaAs: III Defect accumulation and amorphization*  
Nucl. Instr. and Methods B **268** (2010) 155
- U. Reislöhner, H. Metzner, C. Ronning  
*Hopping Conduction Observed in Thermal Admittance Spectroscopy*  
Physical Review Letters **104** (2010) 226403
- C. Kraft, H. Metzner, U. Reislöhner, P. Schley, G. Gobsch, R. Goldhahn  
*Comprehensive photoluminescence study of chlorine activated polycrystalline Cadmium telluride layers*  
Journal of Applied Physics **108** (2010) 124503



- M.A. Zimmler, F. Capasso, S. Müller, C. Ronning  
*Optically pumped nanowire lasers: invited review*  
Semicond. Sci. Technol. **25** (2010) 024001
- A. Dev, R. Niepelt, J.P. Richters, C. Ronning, T. Voss  
*Stable enhancement of near-band-edge emission of ZnO nanowires by hydrogen incorporation*  
Nanotechnology **21** (2010) 065709
- W. Dewald, C. Borschel, D. Stichtenoth, T. Niermann, C. Ronning  
*Phase diagram of Si nanowire growth by disproportionation of SiO*  
Journal of Crystal Growth **312** (2010) 1751
- P. Neumaier, A. Bergmaier, W. Eckstein, R. Fischer, H. Hofsäss, H. U. Jäger, H. Kröger, C. Ronning and G. Dollinger  
*Bimodal range distributions of low-energy carbon ions in tetrahedral amorphous carbon*  
European Physics Letters, **90** (2010) 46002
- J. Geurts, M. Schumm, M. Koerdel, C. Ziereis, S. Müller, C. Ronning, E. Dynowska, Z. Goacki, W. Szuszkiewicz  
*Annealing effects and generation of secondary phases in ZnO after high-dose transition metal implantation*  
Physica Status Solidi B **247** (2010) 1469
- S. Jebril, H. Kuhlmann, S. Müller, C. Ronning, L. Kienle, V. Duppel, Y.K. Mishra, R. Adelung  
*Epitactically Interpenetrated High Quality ZnO Nanostructured Junctions on Microchips Grown by the Vapor-Liquid-Solid Method*  
Cryst. Growth Des. **10** (2010) 2842
- Limei Chen, W. Heimbrodt, P.J. Klar, M. Fröba, C. Ronning, H.-A. Krug von Nidda  
*Optical and magnetic properties of quasi one-dimensional dilute magnetic ZnMnS and antiferromagnetic MnS*  
Physica Status Solidi B **247** (2010) 2522
- C. Ronning, C. Borschel, S. Geburt, R. Niepelt, S. Müller, D. Stichtenoth, J. -P. Richters, A. Dev, T. Voss, L. Chen, W. Heimbrodt, C. Gutsche, W. Prost  
*Tailoring the properties of semiconductor nanowires using ion beams*  
Physica Status Solidi B **247** (2010) 2329
- P. Schaaf, S. Günschmann, M. Hopfeld, J. Wilden, V. Drescher, C. Borschel, C. Ronning  
*Self-organized nanostructuring of composite coatings at high temperatures for drag reduction and self-cleaning*  
Surface and Coatings Technology **205** (2010) 1584
- C. Ronning, C. Borschel, S. Geburt, R. Niepelt  
*Ion beam doping of semiconductor nanowires*  
Materials Science and Engineering **R70** (2010) 30
- R. D'Amato, R. Alexandrescu, V. Bello, F. Huisken *et al.*  
*Advances in the preparation of novel functionalized nanoparticles for bioimaging*  
in: *Proceedings of the 9th IEEE Conference on Nanotechnology 2009*  
2010 IEEE NANO Organizers 597
- C. Jäger, H. Mutschke, Th. Henning, and F. Huisken  
*Analogs of cosmic dust*

in: *Cosmic Dust – Near and Far*, ed. by Th. Henning, E. Grün, and J. Steinacker, Astronomical Society of the Pacific Conference Series, Vol. CS **414** (2010) 319

M. Arold, F. Piuzzi, C. Jäger, and F. Huisken  
*Silicon nanocrystals as matrix material for the desorption of biomolecule-water complexes*  
Chem. Phys. Lett. **484** (2010) 100

M. Steglich, C. Jäger, G. Rouillé, F. Huisken, H. Mutschke, and Th. Henning  
*Electronic spectroscopy of medium-sized polycyclic aromatic hydrocarbons: Implications for the carriers of the 2175 Å UV bump*  
Astrophys. J. **712** (2010) L16

S. Krasnokutski and F. Huisken  
*Ultra-low-temperature reactions of Mg atoms with O<sub>2</sub> molecules in helium droplets*  
J. Phys. Chem. A **114** (2010) 7292

S. Krasnokutski, J. S. Lee, and D.-S. Yang  
High-resolution electron spectroscopy and structures of lithium-nucleobase (adenine, uracil, and thymine) complexes  
J. Chem. Phys. **132** (2010) 044304

L. B. Ma, T. Schmidt, C. Jäger, and F. Huisken  
*Evolution of multiple peak photoluminescence of Ge-doped silicon oxide nanoparticles upon thermal annealing*  
Phys. Rev. B **82** (2010) 165411

A. M. Chizhik, A. I. Chizhik, A. J. Meixner, T. Schmidt, and F. Huisken  
*Fluorescence imaging and spectroscopy of single Si and SiO<sub>2</sub> nanoparticles using confocal microscopy*  
in: Proceedings of the BONSAI Symposium *Breakthroughs in Nanoparticles for Bio-Imaging*, ed. by E. Borsella, AIP Conference Proceedings **1275** (2010) 63

T. Schmidt, L. B. Ma, and F. Huisken  
*Photoluminescence studies of Ge-doped silicon nanocrystals and silicon oxide nanoparticles*  
in: Proceedings of the BONSAI Symposium *Breakthroughs in Nanoparticles for Bio-Imaging*, ed. by E. Borsella, AIP Conference Proceedings **1275** (2010) 71

S. Krasnokutski and F. Huisken  
*Oxidative reactions of silicon atoms and clusters at ultralow temperature in helium droplets*  
J. Phys. Chem. A **114** (2010) 13045

A. Grib, D. Heinert, R. Nawrodt, C. Schwarz, V. Grosse, P. Seidel, I. Martin, S. Rowan, J. Hough  
*Acoustic losses in a thick-quartz plate at low temperatures*  
Journal of Applied Physics **107** (2010) 013504

R. Loetzsch, A. Lübcke, I. Uschmann, E. Förster, V. Große, M. Thuerk, T. Koettig, F. Schmidl, P. Seidel  
*The cubic to tetragonal phase transition in SrTiO<sub>3</sub> single crystals near its surface under internal and external strains*  
Appl. Phys. Lett. **96** (2010) 071901

M. Punturo et al. (u.a. D. Heinert, R. Nawrodt, C. Schwarz, P. Seidel)  
*The third generation of gravitational wave observatories and their science reach*  
Class. Quantum Grav. **27** (2010) 084007

- V. Grosse, S. Engmann, F. Schmidl, A. Undisz, M. Rettenmayr, P. Seidel  
*Formation of gold nano-particles during pulsed laser deposition of  $YBa_2Cu_3O_{7-\delta}$  thin films*  
 Phys. Status Solidi RRL **4** (2010) 97
- V. Grosse, C. Pansow, A. Steppke, F. Schmidl, A. Undisz, M. Rettenmayr, A. Grib, P. Seidel  
*Pulsed laser deposition of niobium thin films for in-situ device fabrication and their superconducting properties*  
 Journal of Physics: Conference Series **234** (2010) 012015
- D. Heinert, A. Grib, K. Haughian, J. Hough, S. Kroker, P. Murray, R. Nawrodt, S. Rowan, C. Schwarz, P. Seidel, A. Tünnermann  
*Potential mechanical loss mechanisms in bulk materials for future gravitational wave detectors*  
 Journal of Physics: Conference Series **228** (2010) 012032
- A. Lübcke, F. Zamponi, R. Loetzsch, T. Kämpfer, I. Uschmann, V. Große, F. Schmidl, T. Köttig, M. Thürk, H. Schwoerer, E. Förster, P. Seidel, R. Sauerbrey  
*Ultrafast structural changes in  $SrTiO_3$  due to a superconducting phase transition in a  $YBa_2Cu_3O_7$  top layer*  
 New Journal of Physics **12** (2010) 083043
- P. Seidel, F. Schmidl, V. Grosse, S. Döring, S. Schmidt, M. Kidszun, S. Haindl, I. Mönch, L. Schultz, B. Holzapfel  
*Iron pnictide thin film hybrid Josephson junctions*  
 Advances in Science and Technology Vol. **75** (2010) 136
- M. Punturo et al. (u.a. D. Heinert, R. Nawrodt, C. Schwarz, P. Seidel)  
*The Einstein Telescope: a third-generation gravitational wave observatory*  
 Class. Quantum Grav. **27** (2010) 194002
- I. W. Martin, R. Bassiri, R. Nawrodt, M. M. Fejer, A. Gretarsson, E. Gustafson, G. Harry, J. Hough, I. MacLaren, S. Penn, S. Reid, R. Route, S. Rowan, C. Schwarz, P. Seidel, J. Scott, A. L. Woodcraft  
*Effect of heat treatment on mechanical dissipation in  $Ta_2O_5$  coatings*  
 Class. Quantum Grav. **27** (2010) 225020
- S. Schmidt, S. Döring, F. Schmidl, V. Grosse, P. Seidel, K. Iida, F. Kurth, S. Haindl, I. Mönch, B. Holzapfel  
 *$BaFe_{1.8}Co_{0.2}As_2$  thin film hybrid Josephson junctions*  
 Appl. Phys. Lett. **97** (2010) 172504
- A. Grib, P. Seidel  
*The origin of multibranch IV-characteristics of shunted Josephson junction Arrays*  
 Journal of Physics: Conference Series **248** (2010) 012063
- A. Grib, Y. Shukrinov, F. Schmidl, P. Seidel  
*Experimental and theoretical investigation on high- $T_c$  superconducting intrinsic Josephson junctions*  
 Journal of Physics: Conference Series **248** (2010) 012038
- P. Kh. Atanasova, T. L. Boyadjiev, Yu. M. Shukrinov, E. V. Zemlyanaya, P. Seidel  
*Influence of Josephson current second harmonic on stability of magnetic flux in long junctions*  
 Journal of Physics: Conference Series **248** (2010) 012044
- M. Büttner, M. Schiffler, P. Weber, F. Schmidl, M. Röder, M. Schnabelrauch, K. Wagner, G. Glöckl, W. Weitschies, P. Seidel  
*Investigation of magnetically active core size distributions utilising magnetic measurements*  
 AIP Conference Proceedings **1311** (2010) 65

P. Seidel

*Neue supraleitende Materialien*

Proceedings Deutsche Kälte-Klima-Tagung 2010, Magdeburg, 17.-19.11.2010, 8pp.

S. Schmidt, S. Döring, F. Schmidl, V. Grosse, P. Seidel, K. Iida, F. Kurth, S. Haindl, I. Mönch, B. Holzapfel

*BaFe<sub>1.8</sub>Co<sub>0.2</sub>As<sub>2</sub> thin film hybrid Josephson junctions*

Appl. Phys. Lett. **97**, 172504 (2010)

## 5.2 Invited talks and colloquia

C. Ronning

*Ion beam doping of semiconductor nanowires*

IEEE INEC conference 2010, Hong Kong, 04.01.2010

F. Huisken

*PL studies on silicon-based nanomaterials*

Bio-Imaging with Smart Functional Nanoparticles (BONSAI), Padova, Italy, January 25 – 26, 2010

H. Metzner

*CdTe thin-film solar cells*

Frühjahrstagung der DPG, Tutorial: Modern Photovoltaics – Techniques beyond Silicon, Regensburg, 21.03.2010

C. Ronning

*Multifunctional semiconductor nanowires for photonic applications*

Frühjahrstagung der DPG, Section MM, Regensburg, 24.03.2010

H. Metzner

*CdTe Thin-Film Solar Cells*

ANTEC Solar Energy, Arnstadt, Kolloquium, 28.05.2010

C. Jäger

*From PAHs to solid carbon*

PAHs and the Universe, Toulouse, France, May 31 – June 4, 2010

C. Jäger

*Formation and spectral properties of carbonaceous cosmic dust analogs*

Bereichsseminar am Fritz-Haber-Institut, Berlin 14. Juni 2010

F. Huisken

*Photoluminescence studies on silicon quantum dots and silicon oxide nanoparticles*

NanoLum Summer School, Porquerolles, France, June 28 – July 1, 2010

F. Huisken

*Absorption spectroscopy of astrophysically relevant molecules in supersonic jets*

27th International Symposium on Rarefied Gas Dynamics, Asilomar, USA, July 10 – 16, 2010

E. Wendler

*In-situ RBS Channelling Studies of Ion Implanted Semiconductors and Insulators*

21<sup>st</sup> International Conference on the Application of Accelerators in Research and Industry (CAARI 2010), August 8 -13, 2010, Fort Worth, Texas USA

C. Borschel

*Simulating and Fitting High Resolution RBS Spectra*

21<sup>st</sup> International Conference on the Application of Accelerators in Research and Industry, Fort Worth (USA), 10.08.2010

C.S. Schnohr, P. Kluth, R. Giulian, D.J. Llewellyn, A.P. Byrne, D.J. Coohson, M.C. Ridgway

*Swift heavy ion irradiation of III-V semiconductors*

17<sup>th</sup> International Conference on Ion Beam Modification of Materials (IBMM), August 21 – 27, 2010, Montreal, Canada

H. Metzner

*CdTe Thin-Film Solar Cells*

Technische Universität Darmstadt, Expertentreffen CdTe, Institute of Materials Science, 26.08.2010

C. Ronning

*CIGS and CdTe photovoltaics*

Workshop of German and Shanghai Vacuum Societies: “Application of Vacuum Technologies for photovoltaic systems, flat panels and solid-state lighting”, Shanghai, 29.08.2010

R. Geithner

*Installation and testing of a rapid DC-SQUID system for a Cryogenic Current Comparator for measuring dark current in the  $\mu\text{A}$  range in superconducting cavities*

DESY, Cavity Meeting, Hamburg, September 1, 2010

E. Wendler, Th. Bierschenk, D. Alber, G. Bukalis, L. Prinsloo, W. Wesch, N. van der Berg, J. Malherbe, E. Friedland

*Damage Formation in Neutron Irradiated 4H-SiC*

6. Workshop RCA (Radiochemische Analytik bei Betrieb und Rückbau kerntechnischer Anlagen, der Deklaration von Abfällen und im Strahlenschutz) & 23. SAAGAS (Seminar Aktivierungsanalyse und Gammaskopie), September 6 – 8, 2010, Dresden-Rossendorf

C. Jäger

*Laboratory astrophysics of dust*

Conditions and Impact of Star Formation: New results with Herschel and beyond, Zermatt, Switzerland, September 19 – 24, 2010

M. Thürk

*Heliumcryogenics for low power applications*

Institutseminar Institut für Photonische Technologien Jena, September 22, 2010

H. Metzner

*Photovoltaik: Elektrische Energie aus Sonnenlicht*

Bundesministerium für Bildung und Forschung, Tag der Energie, Physikalisch-Astronomische Fakultät der FSU Jena, 25.09.2010

C. Ronning

*Challenging issues in CIGS photovoltaics*

5<sup>th</sup> Symposium on Vacuum based Science and Technology, Kaiserslautern, 30.09.2010

W. Wesch  
*Effect of high electronic energy deposition in amorphous silicon and germanium*  
International Conference on Swift Heavy Ion induced Materials Engineering and Characterization (SHIMEC 2010), October 5 – 8, 2010, New Delhi, India

J. Sommerfeld  
*Ion Beam Modifications of Surfaces for Biomedical Applications*  
Physics Colloquium, University of Pretoria, 14.10.2010

W. Wesch  
*Swift heavy ion irradiation of amorphous silicon and germanium*  
Third International Meeting on Recent Developments in the Study of Radiation Effects in Matter (REM), October 24 – 28, 2010, Gramado, Brazil

H. Metzner  
*Photovoltaik: Elektrische Energie aus Sonnenlicht*  
CampusThüringenTour 2010 der Thüringer Koordinierungsstelle Naturwissenschaft und Technik für Schülerinnen, Studentinnen und Absolventinnen FSU Jena, 19.10.2010

R. Geithner  
*Cryogenic Current Comparator CCC*  
GSI, Gruppenseminar der Gruppe Accelerator Beam Diagnostics (SD), Darmstadt, October 25, 2010

H. Metzner  
*Thin-Film Photovoltaics at the Institute of Solid State Physics*  
DAAD und BMBF-Pressereise mit internationalen Journalisten, FSU Jena, 04.11.2010

C. Ronning  
*ZnO nanowires for photonic applications*  
5th Workshop on Nanowire Growth, Rom, 04.11.2010

C. Jäger  
*Laboratory studies on the formation and spectral properties of cosmic dust*  
Synchrotron Radiation in Earth, Space & Planetary Science – Exploiting the UK's newest facility, Diamond Light Source, Oxfordshire, UK, November 10 – 11, 2010

T. Fritz  
*Optische in-situ Spektroskopie an epitaktisch gewachsenen Molekülschichten*  
Universität Paderborn, Physikalisches Kolloquium, (Prof. Dr. W.G. Schmidt), Paderborn, 25.11.2010

C.S. Schnohr  
*Amorphous phase formation and structure in III-V semiconductors via Swift Heavy Ion irradiation*  
Forschungszentrum Dresden-Rossendorf, Institut für Ionenstrahlphysik und Materialforschung, November 28, 2010

H. Metzner  
*CdTe Thin-Film Solar Cells*  
Universität Münster, Institutskolloquium, Institut für Materialphysik, 30.11.2010

R. Nawrodt  
*Thermal Noise in the Monolithic Final Stage*  
Gravitational-Wave Advanced Detector Workshop GWADW2010, Kyoto/Japan, 16.-21.05.2010



R. Nawrodt  
*Thermal Noise and Material Issues for ET*  
Gravitational-Wave Advanced Detector Workshop GWADW2010, Kyoto/Japan 16.-21.05.2010

R. Nawrodt  
*Substrate specifications for the ET mirrors - state of the art*  
3rd Annual ET Workshop, Academy of Science of Hungaria, Budapest/Ungarn, 21.-24.11.2010

P. Seidel  
*Ba-122 and La-1111 thin film Josephson junctions*  
Japanese-EU Workshop "Superconductivity", Washington D.C., USA, August 1, 2010

P. Seidel  
*Neue supraleitende Materialien*  
Deutsche Kälte-Klima-Tagung 2010, Magdeburg, November 17 – 19, 2010

P. Seidel, F. Schmidl, V. Grosse, S. Döring, S. Schmidt, M. Kidszun, S. Haindl, I. Mönch, L. Schultz, B. Holzapfel  
*Iron pnictide thin film hybrid Josephson junctions*  
CIMTEC 2010, 5<sup>th</sup> Forum on New Materials, 6th Int. Conf. Science and Engineering of Novel Superconductors, Montecatini, Italy, June 13-18, 2010

A. Grib, Y. Shukrinov, F. Schmidl, P. Seidel  
*Experimental and theoretical investigation on high-Tc superconducting intrinsic Josephson junctions*  
Dubna-Nano 2010, Dubna, Russische Förderation, July 5-10, 2010

### **5.3 Conference contributions**

#### **Hasselt Diamond Workshop 2010, SBDD XV, Hasselt, Belgium, February 22 – 24, 2010**

B. Benmoussa, J. D'Haen, C. Borschel, L. Goris, A. Soltani, V. Mortet, C. Ronning, M. D'Olieslaeger, H.G. Boyen, K. Haenen  
*Growth and Characterization of hexagonal Boron Nitride by unbalanced RF magnetron sputtering*

#### **16th National Space Science Symposium, Rajkot, India, February 24 – 27, 2010**

A. Maurya, S. Rastogi, G. Rouillé, H. Mutschke, F. Huisken, and Th. Henning  
*Study of vinyl PAH in relation to the infrared 6.2 micron emission feature*

#### **Deutsche Tagung für Forschung mit Synchrotronstrahlung, Neutronen und Ionenstrahlen an Großgeräten (SNI2010), Berlin, February 24 - 26, 2010,**

T. Steinbach, W. Wesch, C.S. Schnohr, P. Kluth, Z.S. Hussain, L.L. Araujo, R. Giulian, D.J. Sprouster, A.P. Byrne, M.C. Ridgway  
*Structural modification of swift heavy ion irradiated amorphous Germanium layers*

#### **Einstein Telescope Meeting Jena, Germany, March 01 – 03, 2010**

D. Heinert  
*Investigations of mechanical losses in bulk materials at low temperatures*

**Frühjahrstagung der DPG, Regensburg, March 21 - 26, 2010**

T. Steinbach, W. Wesch, C.S. Schnohr, L.L. Araujo, R. Giulian, D.J. Sprouster, M.C. Ridgway  
*Influence of electronic energy deposition on structural modification of SHI irradiated amorphous Ge layers*

S. Geburt, G. Bulgarini, C. Borschel, C. Ronning  
*Conversion of rare earth doped ZnS to ZnO nanowires*

C. Borschel, S. Spindler, R. Niepelt, S. Geburt, C. Gutsche, I. Regolin, W. Prost, F.-J. Tegude, D. Stichtenoth, D. Schwen, C. Ronning  
*Ion Beam Induced Alignment of Semiconductor Nanowires*

S. Milz, V. Sivakov, G. Brönstrup, M. Gnauck, R. Niepelt, S. Christiansen, C. Ronning  
*Ion beam doped semiconductor nanowires for energy applications*

J. Kühnel, S. Geburt, C. Borschel, M. Kozlik, A. McDonnell, K. Sunter, F. Capasso, C. Ronning  
*Growth, Characterization and Lasing of CdS Nanostructures*

S. Geburt, C. Borschel, C. Ronning  
*Optical properties of transition metal doped ZnO nanowires*

S. Jankowski, L. Chen, J. Helzel, S. Ye2, C. Ronning, D. Schulz, B. Heimbrodt, D. Klimm, W. Heimbrodt  
*Optical properties of transition metal doped ZnO*

A. Dev, R. Niepelt, J.-P. Richters, C. Ronning, T. Voss  
*Stable enhancement of near band edge emission of ZnO nanowires by hydrogen incorporation*

U. Kaiser, L. Chen, W. Heimbrodt, S. Geburt, C. Ronning  
*Defect induced changes on the dynamics of the Mn 3d<sup>5</sup> luminescence in ZnS:Mn nanowires*

A. Laufer, S. Graubner, H. Metelmann, B.K. Meyer, S. Geburt, C. Ronning  
*Quantification of Impurities in Cu<sub>2</sub>O*

M. Gnauck, U. Schröder, R. Niepelt, C. Ronning, R. Adelung  
*Alternative contacting concept for ZnO nanostructures with regard to sensing applications*

C. Heilmann, D. Heinert, C. Schwarz, A. Tünnermann, P. Seidel  
*Investigation of mechanical losses in bulk materials for gravitational wave detectors*

S. Döring, S. Schmidt, V. Große, F. Schmidl, P. Seidel, M. Kidszun, S. Haindl, B. Holzapfel, I. Mönch  
*Investigation on ironarsenide superconductors for their application in Josephson junctions*

S. Schmidt, S. Döring, V. Große, F. Schmidl, P. Seidel, M. Kidszun, S. Haindl, B. Holzapfel, I. Mönch  
*Preparation and investigation of tunnel junctions based on ironpnictide superconductors*

M. Schiffler, M. Büttner, P. Weber, P. Seidel, C. Lang, D. Schüler, M. Röder  
*Temperaturabhängige Magnetrelaxometrie an magnetischen Nanopartikeln aus Magnetit im Temperaturbereich von 4,2K bis 320K*

**Thüringer Werkstofftag 2010, Ilmenau, Germany, March 24, 2010**

S. Günschmann, J. Wilden, V. Drescher, M. Hopfeld, Elvira Remdt, P. Schaaf, C. Borschel, C. Ronning  
*Selbststrukturierende Oberflächen von Verbundschichten bei Hochtemperaturanwendungen mit Minderung des Strömungswiderstandes und Selbstreinigungseffekt*

**Workshop Ion Beam Physics, Dresden-Rossendorf, March 29 – 31, 2010**

W. Wesch, T. Steinbach, C.S. Schnorr, P. Kluth, Z.S. Hussain, L.L. Araujo, R. Giulian, D.J. Sprouster, A.P. Byrne, M.C. Ridgway  
*Structural modification of swift heavy ion irradiated amorphous germanium*

E. Wendler, Th. Bierschenk, W. Wesch, J.B. Malherbe, E. Friedland  
*Temperature dependence of damage formation in Ag ion irradiated 4H-SiC*

**Thin Film Week on “International Workshop on CIGS solar cell technology“, Berlin, Germany, March 21, 2010**

Jakob Haarstrich  
*Near-interface doping by ion implantation in Cu(In,Ga)Se<sub>2</sub> solar cells*

**BONSAI Symposium: Breakthroughs in nanoparticles for bio-imaging, Frascati, Italy, April 8 – 9, 2010**

A. M. Chizhik, A. I. Chizhik, A. J. Meixner, T. Schmidt, and F. Huisken  
*Fluorescence imaging and spectroscopy of single Si and SiO<sub>2</sub> nanoparticles using confocal microscopy*

T. Schmidt, L. B. Ma, and F. Huisken  
*Photoluminescence studies of Ge-doped silicon nanocrystals and silicon oxide nanoparticles*

T. Schmidt, L. Ma, O. Guillois, K. Potrick, and F. Huisken  
*Synthesis and characterization of light-emitting SiGe nanocrystals*

**Gravitational-Wave Advanced Detector Workshop GWADW2010, Kyoto, Japan, May 16 – 21, 2010**

R. Nawrodt  
*Thermal Noise in the Monolithic Final Stage*

R. Nawrodt  
*Thermal Noise and Material Issues for ET*

D. Heinert  
*Properties of candidate materials for cryogenic mirrors*

C. Schwarz  
*Losses in silicon surfaces relevant for suspension elements in future detectors*

**8<sup>th</sup> International Conference on the Scientific and Clinical Applications of Magnetic Carriers, Rostock, Germany, May 25 – 29, 2010**

M. Büttner, M. Schiffler, P. Weber, F. Schmidl, M. Röder, M. Schnabelrauch, K. Wagner, G. Glöckl, W. Weitschies, P. Seidel

*Investigation of the connection of magnetic active core sizes and hydrodynamic diameters of a magnetically fractionated ferrofluid*

**PAHs and the Universe, Toulouse, France, May 31 – June 4, 2010**

G. Rouillé, M. Steglich, Y. Carpentier, F. Huisken, and Th. Henning  
*Spectroscopy of PAHs carrying polyynyl side chains*

M. Steglich, C. Jäger, G. Rouillé, F. Huisken, and Th. Henning  
*PAHs and the interstellar extinction in the UV-vis wavelength range*

Y. Carpentier, T. Pino, F. Huisken, and P. Bréchignac  
*UV spectroscopy of PAHs produced in a hydrocarbon flame*

G. Féraud, T. Pino, Y. Carpentier, E. Dartois, M. Godard, L. d'Hendecourt, J.-N. Rouzaud, E. Charon, and P. Bréchignac  
*Production and characterization of interstellar-like PAHs and carbonaceous nanograins*

K. Gadallah, H. Mutschke, and C. Jäger  
*UV irradiation makes hydrogenated amorphous carbons (HACs) be a carrier candidate of the interstellar UV bump at 217.5 nm*

**E-MRS Spring Meeting 2010, Strasbourg, France, June 07 – 11, 2010**

C. Kraft, A. Brömel, M. Hädrich, U. Reislöhner, H. Metzner, W. Wesch  
*Phosphorus implanted Cadmium Telluride solar cells*

S. Goetz, M. Oertel, J. Haarstrich, H. Metzner, J. Cieslak  
*Determination of the zinc oxide – molybdenum specific contact resistance for Applications in CIGS-technology*

M. Hädrich, C. Heisler, U. Reislöhner, C. Kraft, H. Metzner  
*Back Contact Formation in Thin Cadmium Telluride Solar Cells*

J. Haarstrich, H. Metzner, M. Oertel, C. Ronning, T. Rissom, C.A. Kaufmann, H.W. Schock, W. Mannstadt, E. Rudigier-Voigt, V. Scheumann  
*Near-interface doping by ion implantation in Cu(In,Ga)Se<sub>2</sub> solar cells*

C. Kraft, M. Hädrich, U. Reislöhner, H. Metzner, P. Schley, R. Goldhahn  
*Investigation of the Excitonic Luminescence Band of Polycrystalline Cadmium Telluride for solar cells*

U. Reislöhner, H. Metzner, C. Ronning  
*Hole Mobility in Cu(In,Ga)(Se,S)<sub>2</sub>-Based Solar Cells at Low Temperatures*

**CIMTEC 2010, 5<sup>th</sup> Forum on New Materials, 6<sup>th</sup> Int. Conf. Science and Engineering of Novel Superconductors, Montecatini, Italy, June 13 - 18, 2010**

P. Seidel, F. Schmidl, V. Grosse, S. Döring, S. Schmidt, M. Kidszun, S. Haindl, I. Mönch, L. Schultz, B. Holzapfel  
*Iron pnictide thin film hybrid Josephson junctions*

**European Summer School NanoLum, Porquerolles, France, June 28 – July 1, 2010**

T. Schmidt, L. Ma, K. Potrick, and F. Huisken

*Laser-induced synthesis and photoluminescence studies of indirect semiconductor quantum dots: Si and Si/Ge nanocrystals*

K. Potrick, T. Schmidt, and F. Huisken

*UV irradiation-induced photoluminescence of Si nanocrystals*

**Dubna-Nano 2010, Dubna, Russische Förderung, July 5 – 10, 2010**

A. Grib, Y. Shukrinov, F. Schmidl, P. Seidel

*Experimental and theoretical investigation on high-T<sub>c</sub> superconducting intrinsic Josephson junctions*

P.Kh. Atanasova, T.L.Boyadjiev, Yu.M. Shukrinov, E.V. Zemlyanaya, P. Seidel

*Influence of Josephson current second harmonic on stability of magnetic flux in long junctions*

A. Grib, P. Seidel

*The origin of multibranch IV-characteristics of shunted Josephson junction Arrays*

**WP2 Meeting Einstein Telescope, Glasgow, UK, July 21 – 22, 2010**

R. Nawrodt

*Status of the WP2, Material and thermal noise issues for ET*

**Junior EuroMat conference 2010, Lusanne, Switzerland, July 26 – 30, 2010**

J. Sommerfeld, T. Keller, T. Schüler, R. Möller, C. Ronning

*Biofunctionalization of diamond like carbon layers*

J. Hönig, T. Keller, T. Schüler, R. Möller, C. Ronning

*Biocompatibility of nanostructured Silicon and TiO<sub>2</sub>*

**Japanese-EU Workshop “Superconductivity”, Washington D.C., USA, August 1, 2010**

P. Seidel

*Ba-122 and La-1111 thin film Josephson junctions*

**Applied Superconductivity Conference (ASC2010), Washington D.C., USA, August 1 – 6, 2010**

M. Büttner, F. Schmidl, M. Schiffler, P. Seidel

*Magnetorelaxation (MRX) measurements with DC-SQUID gradiometers*

R. Geithner, R. Neubert, W. Vodel, M. Schwickert, H. Reeg, R. von Hahn, P. Seidel

*A non-destructive beam monitoring system based on an LTS-SQUID*

**21<sup>st</sup> International Conference on the Application of Accelerators in Research and Industry, Fort Worth (USA), August 08 – 13, 2010**

C. Borschel, S. Spindler, R. Niepelt, S. Geburt, D. Lerose, S.H. Christiansen, C. Ronning

*Ion Beam Induced Bending and Alignment of Semiconductor Nanowires*

**17<sup>th</sup> International Conference on Ion Beam Modification of Materials (IBMM), Montreal, Canada, August 21 – 27, 2010**

T. Steinbach, W. Wesch, C.S. Schnohr, R. Giulian, P. Kluth, L.L. Araujo, D.J. Sprouster, A.P. Byrne, M.C. Ridgway  
*Structural modification of swift heavy ion irradiated amorphous germanium layers*

C.W. Rischau, C.S. Schnohr, E. Wendler, W. Wesch  
*Ion-Beam-induced damage formation in CdTe at a temperature of 15 K*

C.C. Jacobi, T. Steinbach, W. Wesch  
*Development of porous structures in GaSb by ion irradiation*

**8th International Conference on Low Temperature Chemistry, Yerevan, Armenia, August 22 – 27, 2010,**

S. Krasnokutski and F. Huisken  
*Oxidation reactions in helium droplets at ultra-low-temperature ( $T = 0.37$  K)*

**21<sup>st</sup> European Conference on Diamond, Diamond- Like Materials, Carbon Nanotubes, and Nitrides, Budapest, Hungary, September 05 – 09, 2010**

B. Benmoussa, J. D’Haen, C. Borschel, L. Goris, A. Soltani, V. Mortet, C. Ronning, M. D’Olieslaeger, H.G. Boyen, K. Haenen  
*Growth and Characterization of hexagonal Boron Nitride by unbalanced RF magnetron sputtering*

**Zooming in: The cosmos at high resolution, Splinter meeting – ISM Physics of the interstellar medium, Bonn, Germany, September 13 – 17, 2010**

C. Jäger, F. Huisken, and H. Mutschke  
*Laboratory astrophysics experiments in Jena*

**12<sup>th</sup> International Conference on Plasma Surface Engineering, Garmisch-Partenkirchen, Germany, September 13 – 17, 2010**

S. Geburt, C. Ronning, J. Ye, M. Stüber, S. Ulrich  
*Oxygen- and Neon-Ion Irradiation of Oxygen-Containing Cubic Boron Nitride Films*

**Japanese-German Workshop "DUST IN PLANETARY SYSTEMS", Jena, Germany, September 27 - October 1, 2010**

C. Jäger, H. Mutschke, F.Huisken, Th. Henning, and M.Steglich  
*Condensation and processing of cosmic dust*

**Joint meeting: “Paneth Kolloquium” & “The first 10 million years of the solar system”, Nördlingen, Germany, October 27 – 30, 2010**

C. Jäger, H. Mutschke, Th. Henning, and F. Huisken  
*Processing of silicates by ion irradiation*

**Deutsche Kälte-Klima-Tagung 2010, Magdeburg, November 17 – 19, 2010**

P. Seidel  
*Neue supraleitende Materialien*



**Fall meeting of the Materials Research Society (MRS), Boston, USA, November 29 to December 03, 2010**

R. Niepelt, A. Johannes, M. Gnauck and C. Ronning

*In-situ electrical characterization of ion implanted semiconductor nanowires*

Z. Su, C. Ronning, S. Geburt, A. Bensaoula, Q. Yu, S.-S. Pei<sup>1</sup>, Z. Liu<sup>1</sup>, J. Bao

*Observation of CO<sub>2</sub> Photo-desorption on ZnO Surface*

B. Benmoussa, J. D'Haen, C. Borschel, L. Goris, A. Soltani, V. Mortet, C. Ronning, M. D'Olieslaeger, H.G. Boyen, K. Haenen

*Hexagonal Boron Nitride Nanowalls Synthesised by Unbalanced RF Magnetron Sputtering*

## 5.4 Theses

### Diploma and Master Theses

U. Treske	<i>Photoelektronenspektroskopie an hochgeordneten Phthalocyanin-schichten</i>
M. Bohrisch	<i>Elektrische und optische Eigenschaften von Kohlenstoffnanoröhren</i>
M. Meißner	<i>Organische Moleküle auf epitaktischem Graphen</i>
Thomas Bierschenk	<i>Damage formation in 4H-SiC due to Ag<sup>+</sup> ion and neutron irradiation</i>
Jan Wernecke	<i>Ion-beam induced structural modifications in germanium</i>
Julius Jöhrens	<i>Molekulardynamik-Simulationen zur Erzeugung von porösen Schichten in Germanium und Silizium durch Bestrahlung mit schnellen schweren Ionen</i>
Carl Willem Rischau	<i>Ion-beam induced damage formation in Cadmium Telluride</i>
Luise Hentschel	<i>Herstellung und elektro-optische Charakterisierung von CuIn(S,Se)<sub>2</sub>-Solarzellen mit Nachsulfurisierung und CuInSe<sub>2</sub>-Solarzellen mit RTP-Selenisierung unter Atmosphärendruck</i>
Anika Brömel	<i>Elektrische und elektro-optische Untersuchungen an Phosphor-implantierten CdTe-Schichten</i>
Marc Teichmann	<i>Modifikation der Fenster-Absorber-Grenzfläche in Cu(In,Ga)Se<sub>2</sub> – Solarzellen durch Ionenimplantation</i>
Sven Schönherr	<i>Elektrische Charakterisierung von Dünnschichtsolarzellen</i>
Ulrich-Chr. Schröder	<i>Biofunktionalisierung von ZnO-Nanodrähten für die Nukleinsäuresensoren</i>
Stefan Weidner	<i>Erweiterung des Phasendiagramms von kubischem Bornitrid (cBN) und Modifikation mit Ionenstrahlen</i>
Steffen Milz	<i>Konzepte zur Realisierung von einfachen Nanodrahtbauelementen für die Energiegewinnung</i>
Martin Gnauck	<i>Elektrische Kontaktierung von ZnO-Nanostrukturen und deren Verwendung für sensorische Zwecke</i>
Björn Burkhardt	<i>Domänenwanddynamik in weichmagnetischen Strukturen mit nm-Abmessungen (extern)</i>
Janine Fischer	<i>Epitaxie und elektrische Eigenschaften von (Ca,Sr) Rn O<sub>3</sub>/SrTiO<sub>3</sub>-Mehrschichtsystemen</i>
Christoph Heilmann	<i>Mechanische Spektroskopie an verlustarmen Materialien</i>
Robert Kockrick	<i>Messung der Relaxation magnetischer Nanopartikel</i>

Martin Pollithy	<i>Rauschuntersuchungen an Hoch-Tc DC SQUID-Gradiometern</i>
Karsten Potrick	<i>Einfluss der UV-Bestrahlung auf die Photolumineszenzeigenschaften von Silizium-Nanoteilchen</i>
Markus Schiffler	<i>Untersuchungen zu Relaxationsmechanismen an magnetischen Nanopartikeln</i>
Michael Hübner	<i>Untersuchungen zum Wachstumsverhalten von <math>YBa_2Cu_3O_{7-x}</math> – Schichten mit Au-Nanoclustern</i>
Benjamin Voigt	<i>Untersuchung zur Herstellung von Bauelementen auf der Basis von Kohlenstoffnanoröhren</i>
Franziska Walter	<i>Anisotropie der Thermokraft und transversaler Peltiereffekt in Metall-Halbleiter Multilagen (extern)</i>

### **Bachelor Thesis**

M. Grosch	<i>Ansteuerung und Anwendung eines Stimmgabelsensors</i>
K. Wachter	<i>Mikroskopische und spektroskopische Untersuchungen an epitaktischem Graphen</i>
Markus Westernhausen	<i>Untersuchung von ionenstrahlinduzierter Defektformierung in Germanium mittels Raman-Spektroskopie und Rutherford-Weit-winkelstreuung.</i>
Michael Reichmann	<i>Synthese von Halbleiternanodrähten einheitlichen Durchmessers auf Basis von Goldkolloiden und AAO</i>
Gitta Simon	<i>Wachstum von heterogenen Halbleiternanodrähten</i>
Sven Möller	<i>Wachstum von senkrechten ZnO-Nanodrähten auf verschiedenen Glas-substraten</i>
Alina Donat	<i>Fortgesetztes Wachstum von ZnO Halbleiternanodrähten</i>
Franziska Riedel	<i>Charging phenomena on HOPG</i>
Robert Röder	<i>Charakterisierung optischer Eigenschaften von Silizium-Nanokristallen mit Germanium-Dotierung</i>
Irma Slowik	<i>Herstellung und Charakterisierung von ZnO-Nanodraht-Feldeffekttransistoren</i>
Sandra Christke	<i>Herstellung von YBCO-Schichten mit Au-Clustern und deren Untersuchung mittels Rasterelektronenmikroskopie</i>
Andreas Falk	<i>Dämpfungsuntersuchungen an Wolframdrähten für die mechanische Gütemessung</i>
Johannes Häßler	<i>Herstellung von YBCO-Schichten mit Au-Clustern und deren Untersuchung mittels Röntgendiffraktometrie</i>

Per Heisel	<i>Isolatorschichtsysteme zur Herstellung von Kohlenstoff-Nanoröhren</i>
Gerd Hofmann	<i>Methoden und Verfahren zur Gütemessung an Cantilevern</i>
Christian Katzer	<i>Untersuchungen von Mehrschichtsystemen als Wachstumsgrundlage für Kohlenstoffnanoröhren</i>
Stefanie Koch	<i>Kryodruckspeicherung – Ein Beitrag zu einer weiteren Form der Wasserstoffspeicherung</i>
Julius Komma	<i>Untersuchung der mechanischen Verluste eines thermisch oxidierten Silizium-Cantilevers</i>
Daniel Kuhwald	<i>Untersuchung von Au-Clustern auf YBCO-Josephsonkontakten</i>
Peter Michalowski	<i>Politur von Bikristall-Korngrenzen-Kontakten</i>
Torsten Pliewischkies	<i>Herstellung von C-Si-Dünnschicht-Sorlarzellen auf Glasfasern mittels PECVD</i>

## 6. Cooperations, guests and colloquia at IFK

The Institute of Solid State Physics collaborates with a large number of Institutes and Universities in Germany and around the world and has also close connections with several companies. In the framework of these wide spread contacts in 2010 a number of scientists from various countries visited our Institute to perform experiments, discuss scientific results obtained within joint projects and to give talks in the colloquium of the Institute of Solid State Physics.

### 6.1 Visiting scientists

Prof. Dr. K. Baruth-Ram	iThamba Labs, Cape Town, Südafrika
Prof. Dr. E. Friedland	University of Pretoria, Pretoria, Süd-Afrika
Dr. R. Giulian	Australian National University, Canberra, Australien
Dr. Alexander Grib	Kharkov National University, Physics Department
Karen Haughian	University of Glasgow, Institute for Gravitational Research
Dr. Keita Kawabe	LIGO Hanford, USA
Prof. F.F. Komarov	Universität Minsk, Minsk, Belarus
Prof. Dr. Quan Li	Chinese University of Hong Kong, China
Dr. Nicola Ligurio	INFN, Padua/Italien
Maria E. Messing	University Lund, Schweden
Prof. Dr. Johan Malherbe	University of Pretoria, Pretoria, Süd-Afrika
Dr. Peter Murray	University of Glasgow, Institute for Gravitational Research
Dr. Enrico Serra	Fondazione Bruno Kessler, Trento/Italy
Dr. Yury Shukrinov	Bogoliubov Laboratory of Theoretical Physics, Joint Institute for Nuclear Research Dubna
Prof. Dr. Chris Theron	University of Pretoria, Pretoria, Süd-Afrika
Prof. G. Thummes	Universität Gießen
Prof. Dr. A. Turos	Zoltan Institute for Nuclear Physics, Warschau, Polen
Prof. Sergey Vyatchanin	Moscow State University, Russische Föderation
Dr. X.F. Wang	Shenzhen Institute of Advanced Technology, Chinese Academy of Science
Dr. Kazuhiro Yamamoto	INFN, Padua/Italien
Dr. Jean-Pierre Zendri	INFN, Padua/Italien

### 6.2 Colloquia at the Institute of Solid State Physics

Prof. Dr. Heiko B. Weber (Universität Nürnberg-Erlangen), 15.01.2010  
*Ladungstransport in epitaktischem Graphene*

Dr. Markus Bender (GSI Darmstadt), 22.01.2010  
*UHV Ionenstrahlanalytik – Setup und Anwendungen*

Prof. Dr. Klaus Rademann (Humboldt Universität Berlin), 29.01.2010  
*Funktionalisierte Natronkalksilikatgläser mit Gold und Silber: Synchrotronstrahlungsaktivierung, Bildungsmechanismen der Edelmetall-Nanopartikel und Anwendungen*

Prof. Dr. Werner Wesch (FSU Jena, Institut für Festkörperphysik), 05.02.2010  
*Konrad Gärtner - ein Theoretiker mit Liebe zum Experiment*

Dr. Holger von Wenckstern (Universität Leipzig), 23.04.2010  
*Electric and electronic properties of defects in semiconductors: Case studies of mc-Si and single-crystalline ZnO*

- Prof. Dr. Moritz Sokolowski (Universität Bonn), 07.05.2010  
*Große organische Moleküle auf Festkörperoberflächen – Von der chemischen Bindung zur kollektiven Lichtemission*
- PD Dr. Josef Tiggesbäumker (Universität Rostock), 21.05.2010  
*Helium Nanotropfen - Eine außergewöhnliche Matrix für die Spektroskopie an Atomen, Molekülen und Clustern*
- Prof. Dr. Michael Seibt (Universität Göttingen), 04.06.2010  
*Mikroskopie und Spektroskopie an Defekten in kristallinem Silizium für Solarzellen*
- Prof. Dr. G. Dollinger (Universität der Bundeswehr München), 18.06.2010  
*Mikroskopie mit Protonen und Positronen*
- Dr. Christian Wagner (Forschungszentrum Jülich), 25.06.2010  
*Energiegewinn als Triebfeder für epitaktisches Wachstum organischer Schichten: Experiment und Simulation*
- Herr Bernd Helmbold (FSU Jena, Ernst-Haeckel-Haus), 25.06.2010  
*Kernphysik an der Friedrich-Schiller-Universität von 1946 – 1968*
- Prof. Dr. Waldemar Nawrocki (TU Poznan), 22.10.2010  
*Physical limits for scaling of electronic devices in integrated circuits*
- Prof. Dr. Lukas Eng (TU Dresden), 05.11.2010  
*Tuning plasmonic antenna structures for nanophotonic applications from visible to IR wavelengths*
- Prof. Dr. Hannes Töpfer (TU Ilmenau), 19.11.2010  
*Entwicklung energieeffizienter Mikroelektronik mit Supraleitern*
- Dr. Rupert Oulton (Imperial College London), 03.12.2010  
*Deep sub-wavelength lasers based on semiconductor nano-structures*
- Dr. Thomas Keller (FSU Jena, IMWT), 17.12.2010  
*Molecular self-assembly of polymer biointerfaces*

## 7. Teaching activities

### 7.1 Lectures

Physik der Materie I	Prof. Dr. W. Wesch
Physik der Materie II	Prof. Dr. C. Ronning
Nanomaterials and Nanotechnology	Prof. Dr. C. Ronning
Kernphysik für Lehramt	Prof. Dr. C. Ronning
Nukleare Festkörperphysik	Prof. Dr. C. Ronning
Cluster & Nanoteilchen I und II	Prof. Dr. F. Huisken
Laborastrophysik	Prof. Dr. F. Huisken Dr. H. Mutschke
Physik für Nebenfach-Studenten (Biologie, Ernährungswissenschaften, Pharmazie, Biogewissenschaften, Chemie, Biochemie)	Prof. Dr. W. Wesch
Kerne und Teilchen	Prof. Dr. W. Wesch
Photovoltaik I und II	PD Dr. H. Metzner
Experimentalphysik (Mediziner, Zahnmediziner)	PD Dr. F. Schmidl
Festkörperphysik (Physik-Master, Materialwiss. Master)	Prof. Dr. P. Seidel
Tiefemperaturphysik und Kryotechnik	Dipl.-Ing. M. Thürk
Elektronik	PD Dr. F. Schmidl, Dr. R. Nawrodt
Gravitational Wave Detection	Dr. G. Hammond
Optoelectronics (Master of Photonics 3. Semester)	PD Dr. F. Schmidl
Organische Festkörper	Prof. Dr. T. Fritz
Oberflächenanalytik	Prof. Dr. T. Fritz, Dr. A. Winkelmann
Einführung in die Halbleiterphysik	Prof. Dr. T. Fritz

### 7.2 Seminars

Proseminar zum Fortgeschrittenenpraktikum	Dr. B. Schröter
Organische Festkörper	Dr. R. Forker
Oberflächenanalytik	Dr. R. Forker
Einführung in die Halbleiterphysik	Prof. Dr. T. Fritz
Nukleare Festkörperphysik	Prof. Dr. W. Wesch



Physik der Materie I	PD Dr. K. Gärtner, PD Dr. E. Wendler
Physik für Biogeowissenschaftler	PD Dr. E. Wendler
Experimentalphysik I für Physiker	PD Dr. E. Wendler
Experimentalphysik II für Physiker	PD Dr. E. Wendler
Kerne und Elementarteilchen	PD Dr. K. Gärtner
Physik für Chemiker	Dr. C.S. Schnohr
Festkörperphysik (Materialwiss. Master)	Dr. V. Tümpel, Dr. R. Forker
Optoelectronics (Master of Photonics 3. Semester)	PD Dr. F. Schmidl
Elektronik (Physik-Diplom und Informatik)	PD Dr. F. Schmidl, Dr. R. Nawrodt Dipl.-Phys. D. Heinert
Elektronik (Lehramtsstudenten)	Dr. R. Nawrodt, Dipl.-Ing. H. Mühlig
Gravitational Wave Detection	Dr. G. Hammond
Tiefemperaturphysik und Supraleitung	Prof. Dr. P. Seidel
Tiefemperaturphysik und Kryotechnik	Dipl.-Ing. M. Thürk
<b>Tutorium</b> (Messtechnik)	PD Dr. F. Schmidl
<b>Oberseminar</b> (Festkörperphysik/Materialwissenschaften)	Prof. Dr. P. Seidel
<b>7.3 Practica</b>	
Fortgeschrittenen-Praktikum	Dr. B. Schröter (Leitung) Dipl.-Ing. M. Thürk, Dipl.-Phys. Ch. Schwarz
Praktikum für Biochemiker	Prof. Dr. W. Wesch (Leitung)
Praktikum für Biologen	Prof. Dr. W. Wesch (Leitung)
Praktikum für Nebenfächler	Prof. Dr. W. Wesch (Leitung) Dr. C.S. Schnohr
Physikalisches Grundpraktikum	Dipl.-Phys. T. Steinbach
Grundpraktikum für Mediziner	PD Dr. F. Schmidl
Messtechnik	PD Dr. F. Schmidl, Dr. R. Nawrodt Dipl.-Ing. H. Mühlig, Dipl.-Phys. R. Geithner
Elektronikpraktikum Lehramtskandidaten 5. Sem. Physik-Bachelor, Nebenfächler	Dr. R. Nawrodt, PD Dr. F. Schmidl Dipl.-Ing. H. Mühlig, Dipl.-Ing. R. Neubert, Dipl.-Phys. V. Große
Grundpraktikum 3.Semester Bachelor Physik	Dr. R. Nawrodt, PD F. Schmidl Dipl.-Ing. H. Mühlig, Dipl.-Ing. R. Neubert

## 8. Personnel

### Professors

Prof. Dr. habil. Carsten Ronning (director)  
Prof. Dr. habil. Torsten Fritz  
Prof. Dr. habil. Paul Seidel  
Prof. Dr. habil. Werner Wesch  
Prof. Dr. habil. Friedrich Huisken

### Scientific Staff

PD Dr. habil. Konrad Gärtner (to 01/10)  
PD Dr. habil. Heinrich Metzner-Fraune  
PD Dr. habil. Frank Schmidl  
PD Dr. habil. Elke Wendler  
Dr. Yvain Carpentier  
Dr. Roman Forker (since 02/10)  
Dr. Gaël Rouillé  
Dr. Ernst Glaser  
Dr. Cornelia Jäger  
Dr. Mathias Hädrich  
Dr. Giles Hammond (visiting professor 06 - 09/2010)  
Dr. Ronny Nawrodt (since 04/10)  
Dr. Udo Reislöhner  
Dr. Claudia Schnohr  
Dr. Bernd Schröter  
Dr. Volker Tympel (since 10/10)  
Dr. Sergiy Krasnokutskiy

### PhD Students

Christian Borschel	Steffen Milz
Markus Büttner	Raphael Niepelt
Sebastian Geburt	Michael Oertel
Rene Geithner	Karsten Potrick
Martin Gnauck	Tolou Sabri
Veit Große	Torsten Schmidt
Jakob Haarstrich	Christian Schwarz
Daniel Heinert	Tobias Steinbach
Christoph Heisler	Mathias Steglich
Michael Kozlik	Jana Sommerfeld
Christian Kraft	Christian Wolf

### Extern

Uwe Treske	(IFW Dresden)
Boris Ivanov	(IPHT Jena)
Sascha Glathe	(IPHT Jena)
Thomas Schönau	(IPHT Jena)
Gregor Oelsner	(IPHT Jena)
Ivo Zunke	(Innovent Jena)

## **Diploma Students**

Hans-Peter Baumgartl (extern)  
Martin Bohrisch  
Anika Brömel  
Björn Burkhardt (IPHT, extern)  
Sandra Christke  
Sebastian Döring  
Ralf Erlebach  
Janine Fischer  
Stefan Goetz  
Marco Grünewald  
Christoph Heilmann  
Jessica Hönig  
Gerd Hofmann  
Luise Hentschel  
Carolin Jacobi  
Christian Katzer  
Julius Komma  
Daniel Kuhwald  
Robert Kockrick

Julius Jöhrens  
Peter Michalowski  
Martin Pollithy  
Julian Kühnel  
Matthias Meissner  
Peter Queitzsch  
Willen Rischau  
Markus Schiffler  
Matthias Schmidt  
Stefan Schmidt  
Ullrich Schröder  
Falko Sojka  
Susann Spindler  
Florian Szillat  
Marc Teichmann  
Benjamin Voigt  
Franziska Walter (extern)  
Jan Wernecke

## **Technical Staff**

Ulrich Barth  
Uta Bornkessel  
Uwe Eberhardt  
Tobias Eißmann  
Lutz Föllmer  
Silke Frunzke  
Kristina Garlipp  
Frank Jehn  
Gerald Lenk

Holger Mühlig  
Anja Mittelstädt  
Ralf Neubert  
Stefan Prass  
Helga Rudolph  
Sylvia Stender  
Matthias Thürk  
Carmen Voigt



